EXPERIMENTAL AND NUMERICAL INVESTIGATION ON THE FRACTURING BEHAVIOR AND SCALING OF DISCONTINUOUS FIBER COMPOSITE STRUCTURES

Seunghyun Ko

A dissertation
submitted in partial fulfillment of the
requirements for the degree of

Doctor of Philosophy

University of Washington

2021

Reading Committee:

Marco Salviato, Chair

Jinkyu Yang, Co-Chair

Dwayne D. Arola

Program Authorized to Offer Degree:
William E. Boeing Department of Aeronautics and Astronautics

University of Washington

Abstract

EXPERIMENTAL AND NUMERICAL INVESTIGATION ON THE FRACTURING BEHAVIOR AND SCALING OF DISCONTINUOUS FIBER COMPOSITE STRUCTURES

Seunghyun Ko

Chair of the Supervisory Committee:
Marco Salviato
Associate Professor

Discontinuous fiber composites (DFCs) have received significant attention from many industries due to their unique advantages in manufacturing capabilities. Compare to the continuous fiber composites, DFCs can be formed into complex contours. Also, they are optimized to be used for the compression molding process which is a suitable manufacturing method for high volume production. DFCs possess these manufacturing capabilities because of their unique meso-structures. They are composed of randomly oriented, and deposited platelets or chips made of prepregs. Because they contain fiber volume fractions similar to their pristine prepregs, they possess similar stiffness compared to the quasi-isotropic laminate made of identical prepregs. They are a suitable material form to be used for complex shapes yet stiff and lightweight structures.

Despite their strong manufacturing advantages, engineers and designers do not fully appreciate DFCs' capabilities. The main reason is that DFCs possess strong stochastic fracturing behaviors. The complex mechanisms make DFCs far more difficult to analyze and predict their mechanical responses compare to the continuous fiber composites. As a result, many industries are heavily relied on costly physical tests. The physical experiment should only be proceeded when it is necessary. Also, they only provide insights to the meso-structures

that they tested. Therefore, computational models based on the experimental data must be established in order to expand the applications of DFCs.

In this study, we analyze the fracturing behaviors of DFCs and develop computational tools to understand the failure mechanisms. We experimentally investigate and numerically analyze the unique relationship between the meso-structures and macro-scale material behaviors. We focus on the tensile behaviors of DFCs with and without notches. We study various meso-structures composed of different platelet sizes and structural thicknesses. By leveraging the computational tools validated against the experiment, we can create safer and more efficient design guidelines to broaden the applications of DFCs.

TABLE OF CONTENTS

LIST OF FIGURES

Figure Number Page

LIST OF TABLES

Table Number Page

ACKNOWLEDGMENTS

It is a great privilege that I had two advisors during my Ph.D. First, I would like to thank Professor Marco Salviato for his teaching and guidance towards my Ph.D. journey. Professor Salviato not only showed me how to study a field of mechanics but also how to think and tackle new problems in a scientific way. I deeply appreciate his kind dedication to my professional and personal growth to become a scientist and a researcher. And, I will always remember the true Italian foods that him and his wife made.

I would also like to thank my co-advisor Professor Jinkyu Yang. I first started my undergraduate research job at his laboratory. Since then, he always supported my research and guided me to become a researcher. I deeply thank for his guidance toward my study, the presentation skills, how to manage students, and many other personal skills. Lastly, I would like to thank him for the memorable 18 hours of hiking at the Enchantment trail. I will always be proud of myself for the accomplishment that I achieved with him and other lab members.

I also appreciate kind support from the doctoral committee members, Prof. Dwayne D. Arola, Prof. Richard Wiebe, Prof. Dana Dabiri, Prof. Christopher Lum, and Prof. Mark E. Tuttle. Also, many thanks to my colleagues and friends who shared the hardship of the graduate student life. Especially I thank all the MAMS members: Yao Qiao, Eunsik Phenisee, Tony Deleo, Hangyu Kim, Troy Nakagawa, Minh Nguyen, Kathryn Tidwell, James Davey, Shiva Kumar, Rohith Jayaram, Talal Abdullah, Reda Mamoune, Reed hawkins, Luke Kuklenski and many others. I also want to thank all the LEMS members: Hiromi Yasuda, Hyunryung Kim, Rui Zhu, Zhisong Chen, Aman Rajesh Thakkar, James O'Neil, Zhenzhen Su, Rajesh Chaunsali, GilYong Lee, Eunho Kim, Koshiro Yamaguchi, Oliver Shi, Yasuhiro Miyazawa, Chunwei Chen, and others. I thank all the DFC teams including the 50 undergraduates and 11 graduate students. Thank you for your hard work. Also the GUG 307 members: Abhiram Aithal, Pablo Posada, Gustavo Fujiwara, Hiyao Lin, Minh Hoang Nguyen, Avin Vijayachandran, Dawei Lu, and many others. Finally, my undergraduate friends, Sean Lay, Brian Chang, Jingmeng Tian, Guy Ogihara, and Keisuke Tsujita who are still sharing the great friendship over the time.

I would also like to thank many industry professionals. William Avery, Bill Kuykendall, Sean Yeung, Michelle Hickner, Dzung Tran, George Eliot, Ed Connery, Winnie Lin, Nancy-Lou Polk from the University of Washington, Chul Y Park, Ebonni Adams, Matthew Soja, Mike Larson, and Scott Gunther from the Boeing company, Dave Stanley, Ahmet Oztekin, Cindy Ashforth, and Larry Ilcewicz from the FAA, Scott James and Robb Medved from Sekisui Aerospace, Lisa Walton and Gary Bond from Solvay. Lastly I deeply appreciate Dr. S.Rao Varanasi, and Dr. Usha Varanasi for the Varanashi fellowship.

DEDICATION

to my family, Seokmoon Ko (고석문), Kyungja Kim (김경자), and Ahra Ko (고아라) and my girlfriend Yunjung Choi (최윤정) for their endless support and love.

Chapter 1

INTRODUCTION

Increasing demand of lightweight but strong structures using carbon fiber reinforced polymers (CFRPs) is a clear trend not only to the aerospace industry but also the automotive, marine, and etc [1–4]. The rising demand pushes the manufacturing capability of the CFRPs to the limit. Continuous fiber composites are suitable in large and relatively simple contour structures such as wings and fuselages [5]. A successful example is the Boeing 787 [6]. However, the continuous fibers are difficult to manufacture complex hinges, brackets, and other joint structures because the fiber folding and wrinkling [7, 8]. Using a discontinuous fiber form is a promising alternative to manufacture such complex structures.

Discontinuous fiber composites (DFCs) or chopped fiber composites are composed of randomly deposited platelets or chips where pristine prepregs are chopped into a defined size. DFCs are also called as randomly oriented strands (ROS) [9], stochastic prepreg platelet molded composite (PPMC) [10], composite oriented strand board [11], tow-based discontinuous composites (TBDCs) [12], ultra-thin chopped carbon fiber tape reinforced thermoplastic (UT-CTT) [13], chopped carbon fiber chip-reinforced SMC [14], and stochastic tow-based discontinuous composite (STBDC) [15]. DFCs are suitable material form for a compression molding technique because platelets can precisely follow complex mold contour. Therefore, mass production can be easily achieved using this material. Examples of DFCs are shown in Fig. 1.1. In terms of their mechanical properties, DFCs provide superior advantage compared to short fiber composites. Unlike the short fiber composites where the fiber volume fraction is below 30% [16], DFCs maintain 50% or higher fiber volume fractions [17,18]. Such high fiber volume fraction allows DFCs to maintain tensile stiffness near 80 $\sim$ 90% of quasi-isotropic laminate made of identical prepregs [19]. As a result, DFCs can fill in the niche of complex

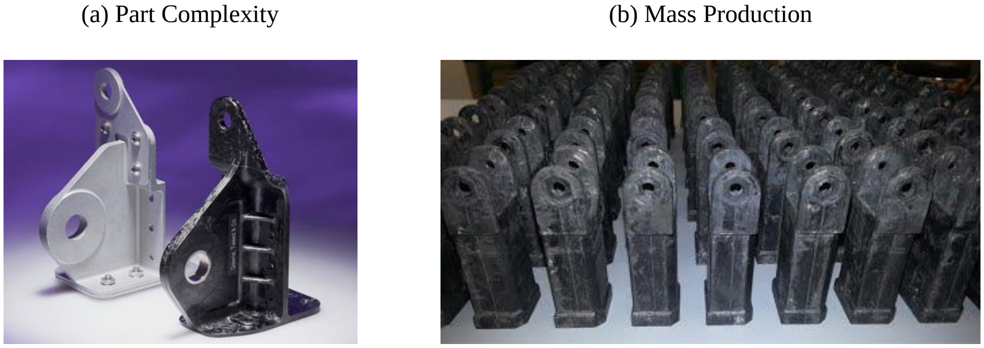

(a) Part Complexity

(b) Mass Production

Figure 1.1: (a) DFCs can easily follow the complex 3D contours. As a result, we can reduce the part numbers and optimize the topology to create more efficient structure. A one to one part comparison between the aluminum vs. DFCs is shown here [20]. (b) Mass manufacturing can be achieved using the compression molding process. The average curing cycle is within 2 minutes according to Hexcel [21].

CFRP structures.

Currently, there are no efficient ways to properly characterize and certify DFC parts without relying on time consuming and costly experiments. DFCs possess unique meso-structures due to highly stochastic orientations of the platelets. The knowledge acquired relying solely on physical experiments tends to be affected by the structures and materials that are tested. Therefore, we need to develop comprehensive computational models to integrate and guide the physical experiments. There are many parameters which govern the mechanical properties of DFCs including e.g., platelet size and aspect ratio, matrix and fiber properties, manufacturing process, and platelet and structure thicknesses [9, 11–13, 22–32]. Feraboli *et al.* [22] pioneered experimental investigations of DFCs with varying thicknesses. They found that the increasing platelet aspect ratio and coupon thickness increased the tensile elastic modulus and strengths. Selezneva and Lessard [9] also investigated the elastic tensile, compressive, and shear properties with varying platelet sizes and coupon thicknesses. They found that higher aspect ratio increased elastic properties but also increased variability of data. They also measured the warpages of DFCs and concluded that regardless of the aspect ratio, increased coupon thickness significantly reduced the plate warpage. Wan and Takahashi [13] studied the relationship between the platelet aspect ratio and molding pressures with tensile and compressive mechanical properties. They found that the molding pressure significantly influenced the strengths of DFCs while the platelet sizes had almost negligible impact on elastic properties. Kravchenko *et al.* [23, 24] and Sommer *et al.* [25] found strong connection between the mechanical properties of DFCs with their underlying fiber orientation tensors. They successfully created digital models of DFC coupons by integrating fiber orientation tensors measured from an x-ray µCT scan to finite element models. Using the finite element models, they precisely captured the failure locations of the scanned coupons. Tang *et al.* [26] and Chen *et al.* [27] also found strong correlation between the fiber orientations and local material properties. They directly measured the fiber orientations using the microscope and compared their measurements against the tensile modulus using a digital image correlation technique. They matched the locations of low modulus with poorly aligned fiber orientations and resin rich area. Li *et al.* [12] and Alves *et al.* [28] experimentally investigated the effects of platelet thickness to tensile properties of DFCs. They found that the thinner platelets promoted higher strength but negligible impact on elastic modulus. The computational models must capture the effects of these parameters determining the mechanical behavior of DFCs. At the same time, the models must consider the effects of platelet orientations whether they are perfectly and randomly oriented or have local biased orientations [12,23–27]. In this study we formulated analysis tools which consider these unique meso-structure characteristics in DFCs.

Addition to the considerations listed above, we must also consider the effect of quasibrittle fracture mechanism. The quasibrittle fracture mechanism involves the study of fracture with structures made of complex, heterogeneous materials with non-negligible inhomogeneities [33–41]. In this case, a size of the fracture process zone (FPZ) with a presence of stress-free

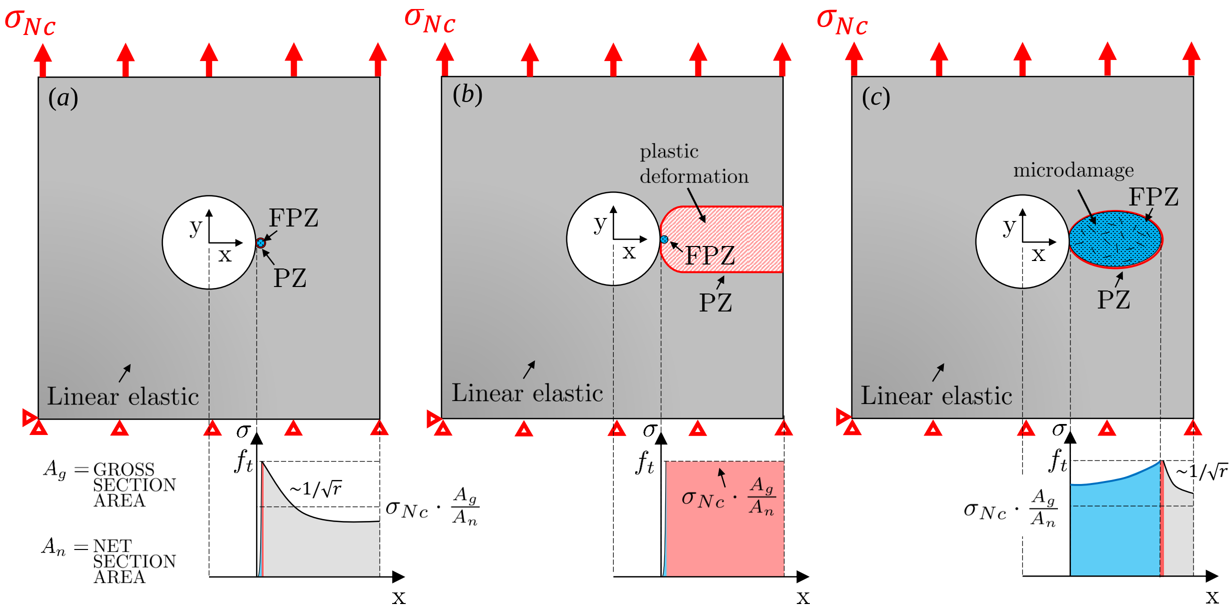

Figure 1.2: The size of material inhomogeneities in front of the notch are compared. Unlike brittle and ductile materials, the quasibrittle material contains non-negligible fracture process zone (FPZ). The stress state in the FPZ is also significantly different compared to the plastic zone (PZ). The characteristics of quasibrittle material are considered in this study.

crack is non-negligible [33–41]. The fracture process zone is an area composed of accumulated micro-damages. If there is a significant portion of FPZ in front of the crack tip compare to the total structure size, neither the linear elastic fracture mechanics (LEFM) nor the ductile fracture mechanics would work to describe the failure (see Fig. 1.2). Therefore, the scaling effect of the structure size must be considered. Many studies have confirmed that polymer composites possess strong quasibrittle fracture [35, 37–40, 42–46]. We expected DFCs to have even stronger quasibrittleness due to highly stochastic fracturing behaviors. We will discuss the scaling effect of DFCs with notched structures in this study.

In Fig. 1.3, we present the objectives of this study: leveraging the building block analysis approach, create material design guidance of DFCs. At the platelet level, the design guid-

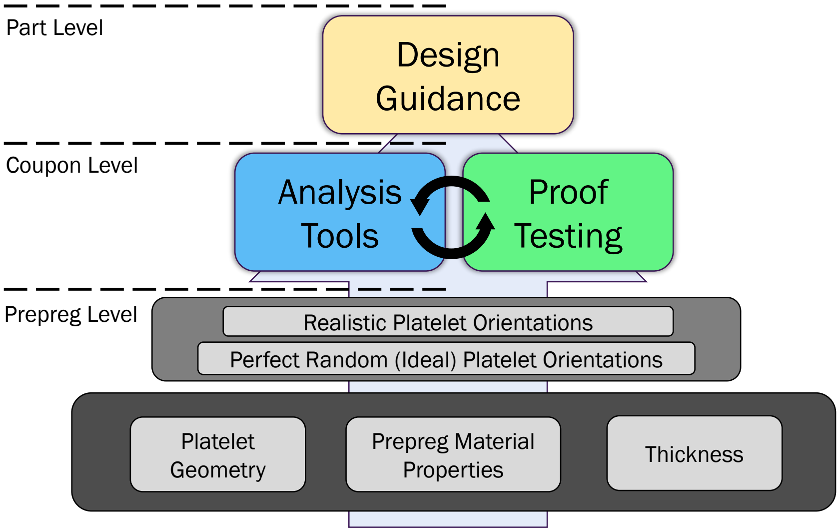

Figure 1.3: Schematic of the building block approach to provide the design guidance of DFCs. Each block is validated through experimental investigations and computational analysis.

ance includes the mechanical properties of the platelets, matrix, platelet geometry, coupon thickness, and etc. At the meso-scale level, we study the effects of the platelet orientation. Using the foregoing studies, we create experimental data sets and computational analysis tools. We identify the mechanical responses and material properties of DFCs with respect to their unique meso-structures. The experiments, numerical models, and analysis results are closely interconnected (see Fig. 1.4). Combining the experimental and numerical analysis, we provide the material design guidance of DFCs.

The dissertation is composed of experimental and computational investigations. Chapter 2 presents the in-house manufacturing process of DFCs made of thermoset prepregs. The thermoset DFCs were used to study the fracture behaviors of notched DFC structures. For unnotched structures, thermoplastic DFCs manufactured by Sekisui Aerospace Corporation [47] were used. Chapter 3 discusses the experimental investigations of unnotched DFC struc-

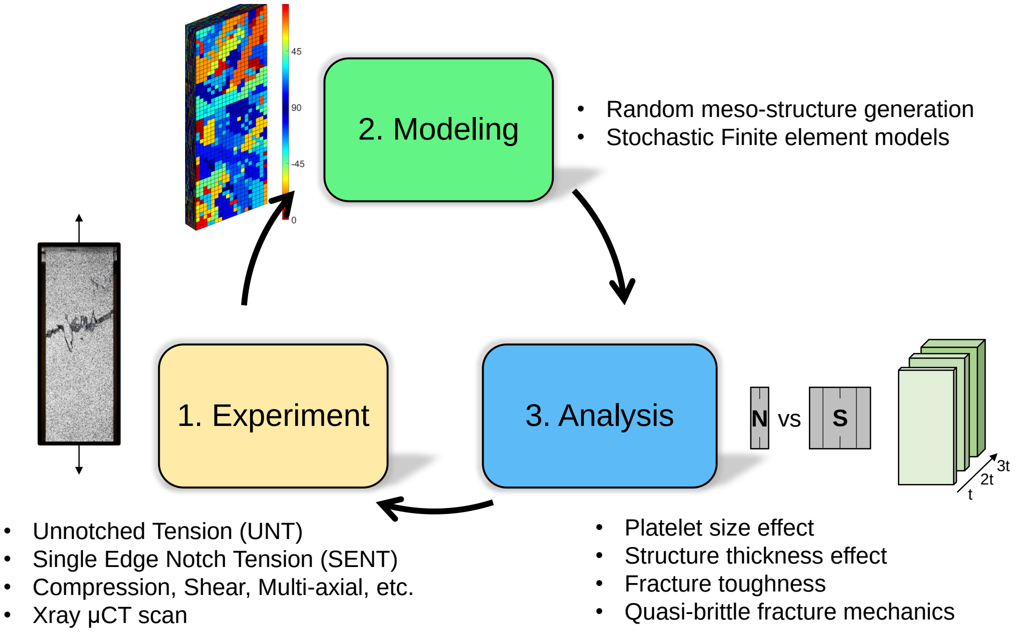

- Random meso-structure generation
- Stochastic Finite element models

- Unnotched Tension (UNT)
- Single Edge Notch Tension (SENT)
- Compression, Shear, Multi-axial, etc.
- Xray μCT scan

- Platelet size effect
- Structure thickness effect
- Fracture toughness
- Quasi-brittle fracture mechanics

Figure 1.4: Research objective of this study. We want to create solid experimental data sets, develop computational models validated by the experiment results, and provide analysis to understand the mechanical behaviors of DFCs. By completing the closed-loop of analysis, we will provide essential information to help the certifications of DFC structures.

tures made of different platelet sizes and coupon thicknesses. The Platelet width effect and the structure thickness effect are discussed. Chapter 4 presents the stochastic finite element model framework. The random platelet meso-structure generation is also discussed. Chapter 5 and 6 discuss the experimental investigations of notched DFC structures. The scaling effect, platelet size effect, and structural thickness effect are discussed. Chapter 7 introduces the application of stochastic finite element models to notched DFC structures. In Chapter 8, we ends this article with main conclusions and future works.

Chapter 2

IN-HOUSE MANUFACTURING TECHNIQUE

2.1 Manufacturing procedure

In this study, we investigate two different prepreg materials used to manufacture the DFC plates. First is the Toray P707AG-15 with T700G-12K fiber reinforced thermoset prepreg. Second is the AS4D/PEKK thermoplastic from Solvay. The thermoset prepreg requires in-house manufacturing process since we want to control the dimensions of the platelets as well as the thickness of the structures. The thermoplastsic prepreg are manufactured by Sekisui Aerospace. In this chapter, we explain how to manufacture thermoset prepreg DFC plates. The main steps of the semi-automated manufacturing protocols are summarized as follows (see Fig. 2.1):

1. Sheets of Toray P707AG-15 with T700G-12K fiber reinforced prepreg are cut into two comb-shaped strips using a CNC fabric cutter (manufactured by Autometrix Advantage). Each strip is cut with a width corresponding to the desired platelet dimensions (Fig. 2.1a). The combs are separated from each other carefully.

2. The protective backing tape is removed. Both surfaces of the prepreg strips are covered using silicone coated parchment papers. The parchment papers act as protective layers which could be easily removed after the final cuts (Fig. 2.1b). Also, the parchment papers secure the position of the strips preventing any movements during the cutting.

3. The prepreg strips are cross-cut to the desired length using the CNC fabric cutter. The variations of the platelet size are minimized due to precise cutting process using the CNC cutter. (Fig. 2.1c);

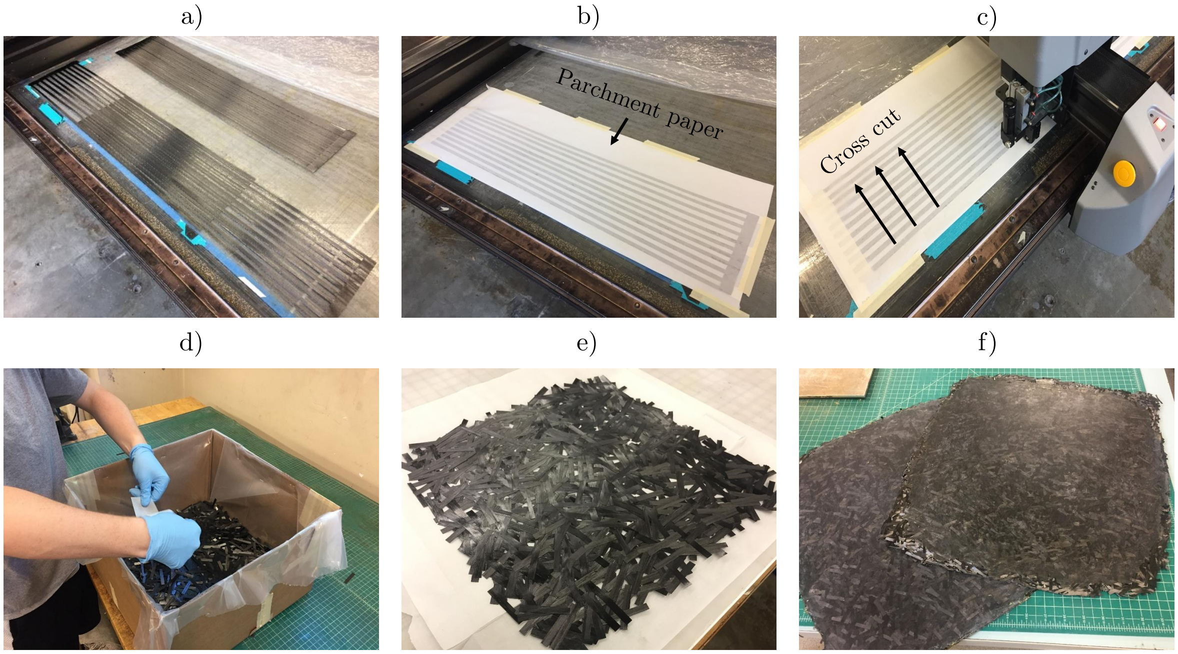

Figure 2.1: In-house manufacturing process of the DFCs.

4. The platelets are manually shaken into a container in a random fashion to form a mat. To reduce the empty spots, the box is rotated periodically. If the empty spots are observed, the platelets are manually placed (Fig. 2.1d);

5. The mat stacking method proposed by Jin *et al.* [11] is adapted to control the thickness of the plate. The mass of a single mat is around 100 g. Approximately eight mats are used to build the plate with 3.3 mm thickness;

6. After the desired mass of the plate is reached, the plate is debulked under 100 kPa for two hours. The debulking process removes air pockets trapped between the platelets and enhances the uniform thickness throughout the plate;

7. The DFC plate is transported to the hot press for the curing. The curing process is (1) ramping rate of 3°F per minute for an hour, (2) hold the temperature at 270 °F for two hours under 0.6 MPa, and (3) 30 minute cool down to the room temperature;

8. The cured plate (see Fig. 2.1f) is trimmed 15 mm from the edges using the diamond blade tile saw to remove possible uncured spots.

A thorough analysis of the plates confirmed the reliability of the proposed manufacturing process. In fact, the volume fraction of voids is far below 2% for all the plates manufactured in this work. The thickness variation is within a tolerance of ±3.31%. A detailed manufacturing process also can be found here [48, 49].

Chapter 3

TENSILE FRACTURING BEHAVIORS OF UNNOTCHED DISCONTINUOUS FIBER COMPOSITE STRUCTURES - EXPERIMENTAL INVESTIGATION

3.1 Introduction

Platelet-based DFCs have significant advantageous in the manufacturing capability but also possess analysis complexity. Comparing with the continuous fiber, DFCs have inhomogeneous meso-structures due to their randomly distributed platelets. Therefore, characterizing the meso-structures become the major challenge. Many researchers studied the relationship between the meso-structure characteristics and the mechanical properties. Feraboli *et al.* [22,50] investigated the effects of platelet sizes and coupon thicknesses to elastic properties and strengths. They found that longer platelets with thicker coupons improved the performances. Selezneva *et al.* [9] expanded the platelet sizes and coupon thicknesses. They found that meso-structure characters such as warpages, out-of-plane orientations, and resin-rich areas also impacted the mechanical performances of DFCs. Wan and Takahashi [13] related manufacturing parameters with the performances of DFCs. They found that increasing the hot-press pressure decreases the void contents, therefore, increases the tensile strength. The modulus did not show particular correlation with the pressure. Li *et al.* [12] found that the thinner platelets have advantage in the tensile strength. Ko *et al.* [29, 30] found that the mode I fracture energy is a function of the platelet size and the coupon thicknesses. Longer platelets and thicker coupons provided higher fracture energy. Also, they noticed that DFCs are much larger fracture process zone [36,38–40,51–54] compared to the continuous fiber composites. The fracture process zone in front of the notch was found to be $3 \sim 7$ times larger than the continuous fiber composites. Among many different meso-structure characteristics, the platelet orientation draw significant attention. To explicitly measure the platelet orientation, researchers started to utilize a X-ray micro Computer Tomography (μCT) scanning technique. Wan and Takahashi [55–57], Denos *et al.* [10, 58], Kravchenko [59], and Favaloro *et al.* [60] measured the platelet orientation tensors by calculating the gradient differences between the neighboring voxels. They integrated the platelet orientations into finite element models, analyzed complex 3D structures. Kravchenko [59] found out that when there are no particular directional flow in the manufacturing process, the average orientation tensor of the DFC coupons remained close to a quasi-isotropic laminate. Martulli *et al.* [61] observed DFC coupons with directional flow which induced significant platelet orientation change compared to the no flow coupons.

In this section, we study the effect of the coupon thickness and the platelet width in the tensile elastic modulus and strength. We focus on both average and variation of the mechanical properties. To do so, we propose testing of large number of coupons to create statistically meaningful experimental data. DFCs possess high scatter in experimental data compare to the continuous fiber composites [9, 12, 13, 22, 23, 29, 30, 50, 59]. Due to the high variation, the number of test coupons must be larger than the minimum recommended test coupons (at least 5 coupons) suggested by ASTM D3039 test standard for the continuous fiber composites. Kravchecnko *et al.* [23] tested $10 \sim 24$ coupons to address the importance of the statistics. However, the number of test coupons varied throughout the tests. We propose a sample size based on the largest coupon test from Kravchecnko *et al.* [23]. Having the statistical significant data create solid experimental data to understand the statistical variations in the DFC material properties.

3.2 Experiment

3.2.1 Preparation

We investigate three coupon thicknesses and two platelet widths. The two platelet width are the square and the narrow. The square platelet is 0.5" × 0.5". The narrow platelet has an identical length but reduced width. The exact dimension is undisclosed due to proprietary reason. We tested the coupon thicknesses of 0.065", 0.15", and 0.25" for the narrow platelets and 0.065", and 0.15" for the square platelets. Sekisui Aerospace manufactured 12" × 12" flat DFC plates made of AS4D/PEKK thermoplastic tapes from Solvay. We discarded half-inch from the edges, and trimmed 10" × 1" tensile coupons. We used a wet tile saw with a diamond blade to trim the plates. Each coupon had two 2" garolite tabs at the ends, leaving 6" as a gauge length. We sprayed a layer of flat white paint with black paint speckles on a single side to measure the surface displacements using the Digital Image Correlation (DIC) technique. We tested the coupons using a ShoreWestern servo-hydraulic axial-torsion load frame with a closed-loop control. The load frame capacity was 56 kip. The loading strain rate was set at 0.6% strain per minute. Total duration of the test was 2 ∼ 3 minutes per coupon. A digital camera captured the surface with a sampling rate of 1 Hz. Taken images were analyzed using GOM software [62] to measure the surface displacements.

We carefully selected the number of test coupons to fully capture the statistics of DFCs. Cochran's sample size formula [63] was used to determine the sample population. The Cochran's sample size formula calculates a sample size to meet desired accuracy from a given probability.

$$n = \left[\frac{Z * \sigma}{PA * \mu - \mu}\right]^2 \tag{3.1}$$

n is the sample size, Z is the confidence level set equals to 95% (= 1.96), σ is the data standard deviation, μ is the data average value, and PA (Percent Accuracy) is the desired accuracy. We set $PA = 95\%$. For the data average and standard deviation, we used uniaxial tension test results from Kravchenko et al. [23] where they tested 24 coupons. The average strength (μ) was 33.2 and the standard deviation (σ) was 4.02. Using Eq. 3.1, the suggested sample size (n) was 22. In Fig. 3.1, a sample size distribution is plotted against the percent accuracy. As can be notice, the traditional sample size (5 ∼ 8) is much smaller compare to the suggested sample size. In this study, we tested more than 30 coupons to fully characterize the statistics of DFCs. For the thickness of 0.065", we tested 15 coupons due to manufacturing difficulties involving with thin panels. However, the sample size was still

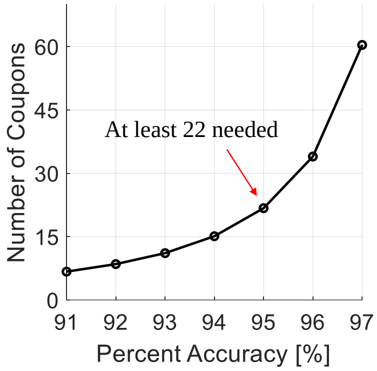

Figure 3.1: An example of Cochran sample size distribution. We choose to have 95 percent accuracy which lead to test at least 22 coupons. We select the population size of 30 to be conservative.

higher than the traditional sample size.

3.2.2 Experiment Results

Regardless of the platelet widths and coupon thicknesses, we observe significant variations associated with the tensile elastic modulus and strength. In Fig. 3.2 and 3.3, representative normalized stress and strain curves of the narrow and square platelets with different thicknesses are plotted. The stress is normalized against the theoretical strength of a quasi-isotropic laminate made of the identical prepreg material properties. For the narrow platelet with 0.25" thickness, a percent difference between the minimum and the maximum strength is nearly 52%. We check the outliers in the test data using the maximum normed residual method suggested by Composite Material Handbook-17 (CMH-17) [64]. All the test data safely passes the outlier test. A summary of the test results is listed in Table 3.1.

Highly chaotic and random fracture patterns are observed through out the coupons. In

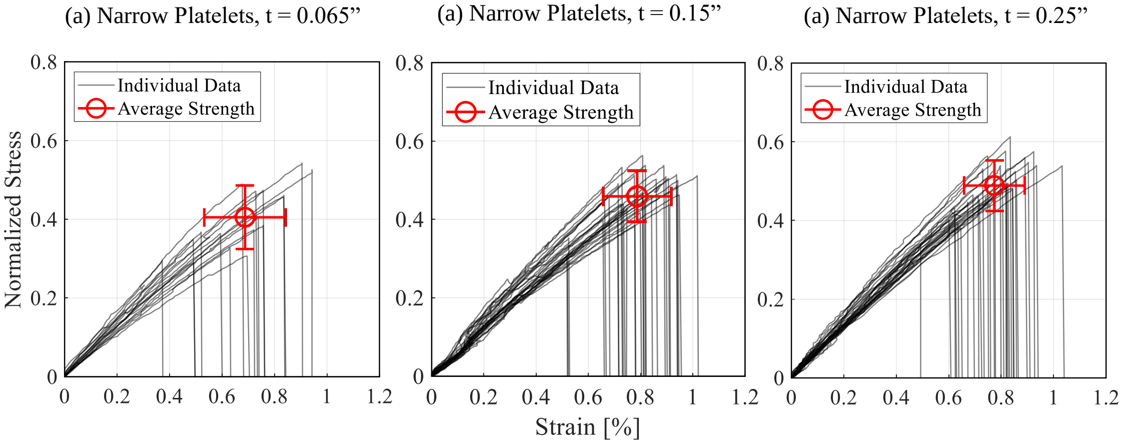

Figure 3.2: Experimental normalized stress and strain curves of the narrow platelets with different coupon thicknesses. The tested DFC coupons possess strong variability in the tensile modulus and strength. The mean strength is plotted as a circle with one standard deviation using the error bars. The square platelets show similar stochastic behaviors.

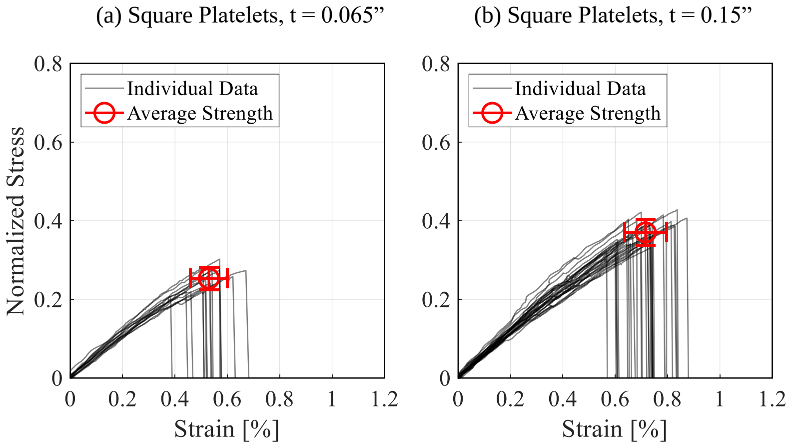

Figure 3.3: Experimental normalized stress and strain curves of the narrow platelets with different coupon thicknesses. A similar statistical variations in the modulus and strength are observed in the square platelet. The mean strength is plotted as a circle with one standard deviation using the error bars.

Table 3.1: A summary of the experiment results

Platelet Size	Thickness [in]	Normalized Modulus	Modulus CoV [%]	Normalized Strength	Strength CoV [%]	Tested Coupons
Narrow	0.065	0.91	11.6	0.41	18.7	17
	0.15	0.89	12.9	0.46	13.6	33
	0.25	0.94	9.3	0.50	11.6	33
Square	0.065	0.78	11.1	0.25	10.8	15
	0.15	0.83	6.7	0.37	8.3	30

*Normalized against the theoretical modulus and strength of a quasi-isotropic laminate made with identical prepreg material properties.

Fig. 3.4, three representative fracture surfaces of different platelet widths and thicknesses are shown. Interestingly, for the narrow platelets with 0.065” thickness, two out of 22 coupons failed with two distinct locations (see Fig. 3.4c). These double fractures happened only at the 0.065” thickness with the narrow platelets. The double fractures must be strongly related with the randomness associated with the meso-structures. At the 0.065”, we observe significant plate warpages. Selezneva et al. [9] showed that the warpage increases drastically as the thickness decreases. The warpage caused by the paucity of platelets through the thickness leads to highly non-symmetric, unbalanced layups. Therefore, these warped plates have strong axial-twist coupling. When the axial load was applied, strong twisting of the coupons led to double fractures near the ends of the coupons. However, we did not observed any significant strength and modulus reduction due to the double fractures.

The analyzed experiment results are plotted in Fig. 3.5 and 3.6. Tensile elastic modulus and strength are normalized against the theoretical quasi-isotropic laminate properties. When the thickness increases from 0.065” to 0.25”, the narrow platelet strength increases by 19.6% and the modulus increases by 4.3%. For the square platelet, the strength and modulus are

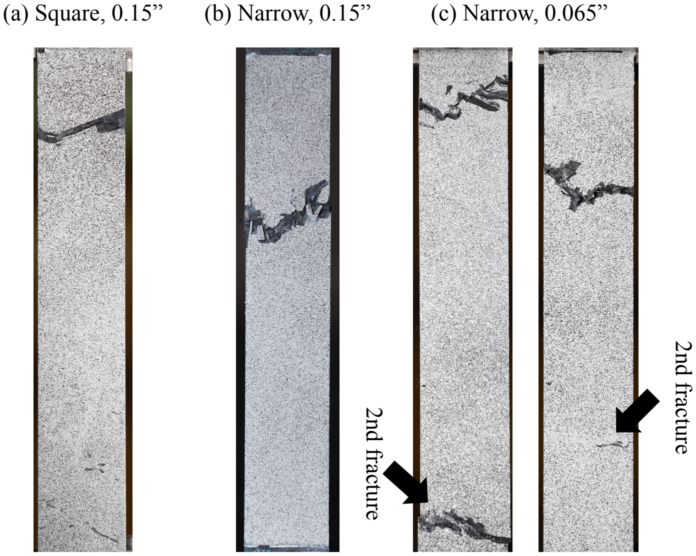

Figure 3.4: Representative fracture surfaces of the different tested DFC coupons. The narrow platelets possess stronger chaotic fracture surfaces compared to the square platelets. Also, we observe two coupons with double fractures from the narrow platelets with 0.065” thickness. However, the strength shows no significant difference compared to the rest of the group.

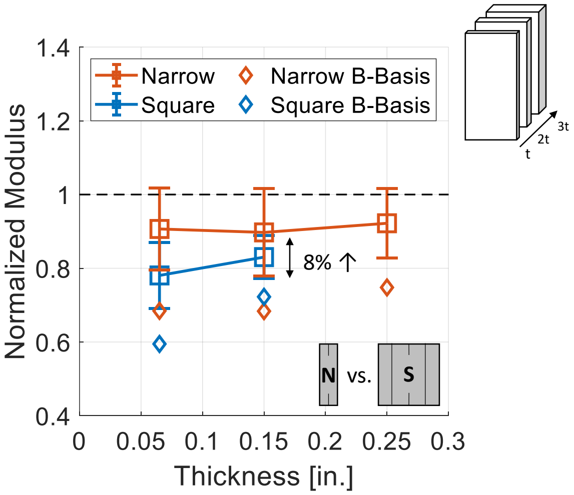

Figure 3.5: A summary of the modulus thickness effect of the narrow and square platelets. The thickness effect in the tensile elastic modulus is insignificant for both platelet sizes.

increased by 32.4% and 6.0% when the thickness increases from 0.065" to 0.15". The thickness effect is more pronounced at the square platelet. Comparing the mechanical properties of the two platelet sizes, the narrow platelet outperforms both modulus and strength in all thicknesses. The percent differences between the two platelets are 15.1% in the modulus and 48.5% in the strength at the 0.065" thickness. The differences are reduced as the thickness increases. In section 4.3.1, we predict the modulus and the strength at the thickness of 0.5" using a finite element model. The difference in the modulus becomes negligible at the thickness of 0.5". However, the narrow platelet still outperforms by 7.6% in the strength.

The narrow platelet has higher average modulus and strength throughout the thicknesses but a trade-off exists. The narrow platelet also possesses a higher Coefficient of Variation (CoV). The CoV decreases with increasing the thickness and the platelet width. Kravchenko *et al.* [23] also found a similar trend. They claimed that the decreasing variation in the mechanical properties are related with the decreasing local variability. As the structure thick-

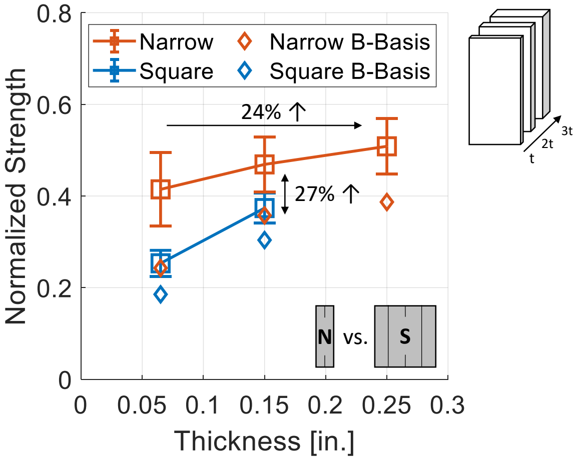

Figure 3.6: A summary of the strength thickness effect of the narrow and square platelets. A significant thickness effect is observed in both platelet sizes.

ness increases, the local orientation variation decreases because there are larger number of platelets through the thickness. However, this analogy is only partially true. When the platelet width decreases, despite the fact that there are more platelets in the coupon, the modulus and strength variations decrease. Here, we must distinguish between the through thickness variation and the spatial variation. The through thickness variation decreases when the total number of platelets increases. On the other hand, the spatial variation increases when the total number of platelets increases. Therefore, we must be cautious when we relate the variations of the material properties with the total number of the platelets.

Besides the average and CoV of the experiment results, we also calculated B-Basis design values following the CMH-17 [64]. The B-Basis design value is the lower tenth percentile of the distribution with a 95% confidence level. In other words, 10 out of 100 specimens will fail below the B-basis value with 95% confidence level. To calculate the B-basis value, we first identified the probability distributions of the test data. We used the Anderson-

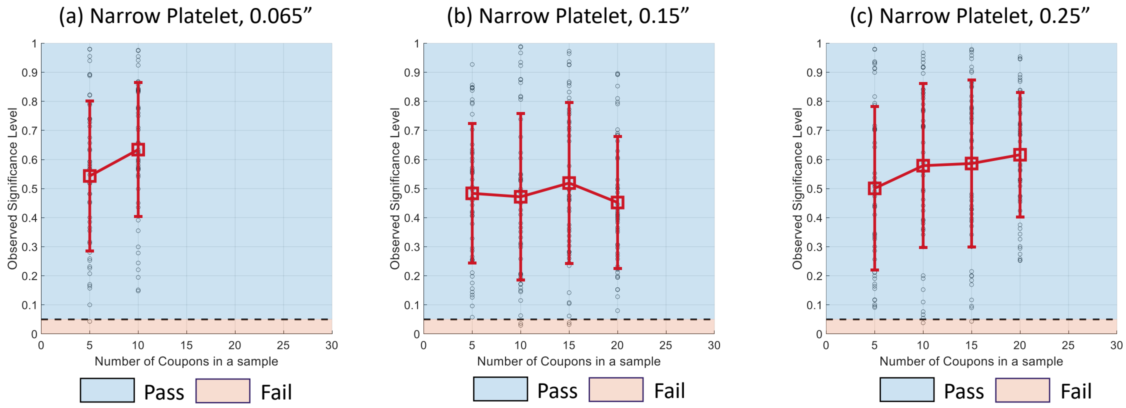

Figure 3.7: Anderson-Darling statistical test for the tensile modulus of the narrow platelet with different thicknesses. Throughout the thicknesses, the modulus matches well with the normal distribution.

Darling statistic test suggested by CMH-17 [64]. The modulus data fitted well to the normal distribution. The strength data fitted both normal and the Weibull distribution. However, we chose to use the Weibull as CMH-17 [64] recommended. We also varied the number of samples in a statistical test to observe if there is a significant change to the AD test when the sample number decreases. For example, we picked a set of random samples out of total test data. Each set possessed unique test data. We ran the AD test and plotted the observed significance level. We repeated the process multiple times and found the average and standard deviation. In Fig. 3.7 and 3.8, we plot the results of statistical tests for the narrow platelet. As can be noted, in average, the modulus passes the test with the normal distribution regardless of the thickness. However, in strength, the statistic test was near fail at the coupon thickness of 0.065”. Therefore, using a B-basis design value may not work at the very thin DFC coupons (less than 11 platelets through the thickness).

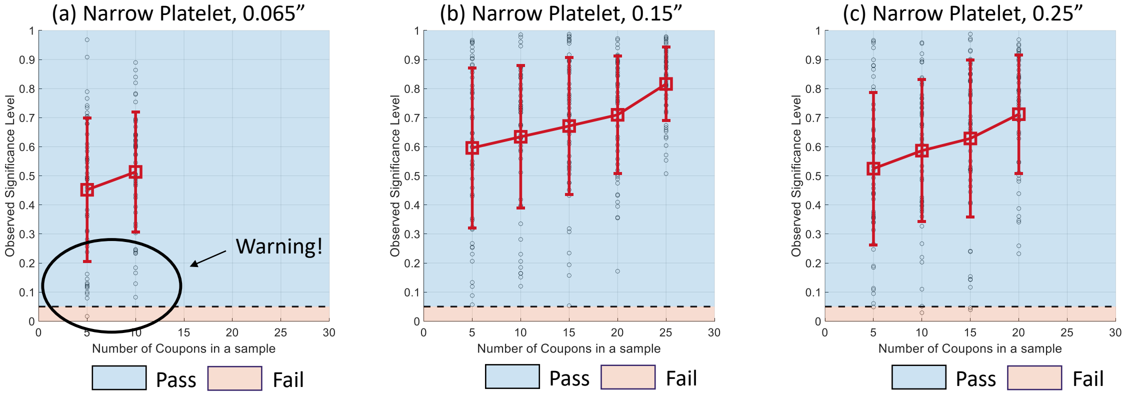

Figure 3.8: Anderson-Darling statistical test for the tensile strength of the narrow platelet with different thicknesses. Throughout the thicknesses, the strength matches well with the Weibull distribution. However, near the thickness of 0.065”, the strength distribution starts to deviate from the Weibull. Therefore, we must be careful to use the Weibull distribution at low thickness coupons.

Once the distribution was identified, we followed a step-by-step guide from the CMH-17 [64]. The results are plotted as diamond markers in Fig. 3.5 and Fig. 3.6. As can be noted, the B-Basis values are strongly affected by the CoVs. Due to the strong variation at the 0.065” thickness, the narrow platelet B-Basis is lowered by 41% compared to the average strength. Also, a high variation in the narrow platelet results in 5.4% decrease in the B-basis modulus compare to the square platelet at the thickness of 0.15”. However, the average modulus for the narrow platelet at 0.15” is actually 6.7% higher than the square platelet. Indeed, the material property variation plays a significant role. A list of the B-basis design values is in Table 3.2.

Table 3.2: A summary of the B-basis design values

Platelet Size	Thickness [in]	Normalized modulus B-basis value	Normalized strength B-basis value
Narrow	0.065	0.685	0.243
	0.15	0.684	0.358
	0.25	0.748	0.387
Square	0.065	0.595	0.185
	0.15	0.723	0.304

3.3 Conclusion

1. DFCs possess strong thickness effect in the tensile modulus and strength. From the experiment, we observe 1.4 and 22.4% increase in the modulus and strength of the narrow platelet when the thickness increases from 0.065” (11 layers) to 0.25” (45 layers). With the square platelet, we observe 6.4 and 47.8% increase in the modulus and the strength when the thickness increases from 0.065” to 0.15” (27 layers).

2. The narrow platelet outperforms the square platelet in both average modulus and strength. At the thickness of 0.15”, the narrow platelet outperforms by 8.0% in the

modulus and 25.4% in the strength. However, the narrow platelet also possesses significantly higher Coefficient of Variations (CoVs) than the square platelet (12.9 vs 6.7% in the modulus and 13.6 vs 8.3% in the strength). Therefore, a trade off exists between the average and variation of the mechanical properties when the platelet width changes.

3. Using the Anderson-Darling statistical test, we find the matching statistical distributions for the modulus and strength. Regardless of the thickness, the modulus distribution fits well with the Gaussian distribution. The strength distribution fits well with the Weibull distribution. However, near the 0.065" thickness, some data set starts to deviate from the Weibull distribution. Therefore, engineers and designers must be careful to use those distributions at low thickness coupons.

Chapter 4

TENSILE FRACTURING BEHAVIORS OF UNNOTCHED DISCONTINUOUS FIBER COMPOSITE STRUCTURES - COMPUTATIONAL INVESTIGATION

4.1 Introduction

Based on the numerous experimental data, computational modelings of DFCs are developed to understand the relationship between the meso-structures and various mechanical properties. Feraboli *et al.* [65] and Harban *et al.* [66] introduced discretized, partition-based stochastic finite element model. They divided 2D space into square partitions and stored unique platelet orientation generated by a certain probability distribution. This partition-based approach was further improved by Selezeneva *et al.* [67]. They explicitly generated platelets over the partitioned space, stacking them like tetris fashion to create meso-structures. This approach effectively captured the random strain field in DFCs. Kravchenko *et al.* [23], Sommer *et al.* [25], Shah *et al.* [68], Visweswaraiah *et al.* [69], Chen *et al.* [14], Ryatt *et al.* [15] contributed to improve the explicit generations of the platelets by introducing additional features. Those features were including prevention of platelet concentrations, thickness adjustments, platelet deformation, and conserving out-of-plane orientations. Researchers also worked on analytical methods. Li and Pimenta [70] and Henry and Pimenta [71] developed semi-analytical method equipped with shear-lag model to predict the strength of DFCs. They captured the tensile strength with respect to the platelet thickness. Wan *et al.* [57] developed analytical approach combined with the partition-based platelet generation to find the modulus of flat DFC coupons. The model matched the experimental data with different platelet sizes.

Many studies successfully matched their average experimental results using the computational models. However, we often neglect another key statistical characteristic of DFCs, the variation. Without matching the variations, engineers and designers must rely on a high margin of safety, wasting material capability. Only when the models successfully match both average and variation, the DFCs can be safely utilized.

In this chapter, we introduce two fundamental elements of the computational investigation of DFCs. First is the random platelet meso-structure generation. The generation algorithm precisely mimic the manufacturing process, therefore capable of providing realistic representation of complex DFC meso-structures. Second is the transformation of the meso-structures into the finite element models equipped with progressive damage modeling. The stochastic FE models capture the key failure mechanisms involved with DFCs to simulate tensile behaviors.

4.2 Computational Modeling Framework

We develop a computational modeling framework to understand the effects of the meso-structure characteristics to the material properties of DFCs. We categorize the framework into three stages: (1) Random platelet meso-structure generation, (2) Random platelet spatial variation, and (3) Stochastic finite element modeling. First and second stages create random meso-structures closely following the manufacturing process. The last stage transforms the meso-structures into finite element models.

4.2.1 Random platelet meso-structure generation

The meso-structures made of randomly deposited platelets govern the mechanical behaviors of DFCs. For example, the platelet length, aspect ratio, thickness, and orientations influence the mechanical performances of DFCs [9, 12, 13, 22, 23, 29, 30, 50, 59]. Therefore, we prioritize building the meso-structures closely mimicking the manufacturing process. We follow the manufacturing process called mat-stacking method introduced in the following studies [11, 29, 32].

The main purpose of the meso-structure generation algorithm is to store unique platelet information explicitly. We adapt the discretized, partition-based method [65, 66] where the individual platelet information are stored into partitions. The partition size is 0.02" $\times$ 0.02". The partition size is determined to have at least three partitions across the smallest length of the platelet. In Fig. 4.1, a platelet inside of the discretized space is plotted.

4.2.1.1 Platelet distribution algorithm

We explicitly generate platelets with pre-defined geometry and orientations. We use an uniform random distribution for the random orientation. But the algorithm is robust enough to adapt any probability distribution (e.g., Gaussian, or trapezoidal). We deposit the platelets into random locations inside the 12" $\times$ 12" space. The partitions interfere with the platelets store the orientations. Multiple platelets can be deposited in a partition but we keep track the order of the deposition. Therefore, through the thickness, the platelets are deposited tetris-like fashion. When the platelets are generated without restrictions, a significant uneven distribution of the platelets are often observed, similarly observed by Selezneva *et al.* [67]. To prevent such unrealistic unevenness, we implemented the following algorithms.

DFC structures exhibit a natural spatial distribution on the number of platelets through the thickness. To characterize this morphological feature, 90 DFC samples were observed under an optical microscope (Omax 9 MP camera with Nikon M Plan 20 objective) to record the actual number of platelets through the thickness. A sample image is plotted in Fig. 4.3. The measured coefficient of variation (CoV) was 0.22 for an average of 24 layers. To achieve the desired CoV in the numerical model, two strategies are implemented in the algorithm: (1) the platelet-limit zone and (2) the saturation points (see the decision boxes in Fig. 4.2). The platelet-limit zone blocks additional platelet depositions at the certain partitions when they reach the allowable limit. If a platelet is placed on top of the limit zone, the algorithm rejects it and a new platelet is generated at another random location. The saturation points decide the allowable limits in the partitions. In the case of 24 layers, every third layer is the saturation point which corresponds to the mat stacking manufacturing method as described in Section 2.1. Therefore, the allowable limits are $[3, 6, 9, ...24] \times$CoV. The algorithm repeats

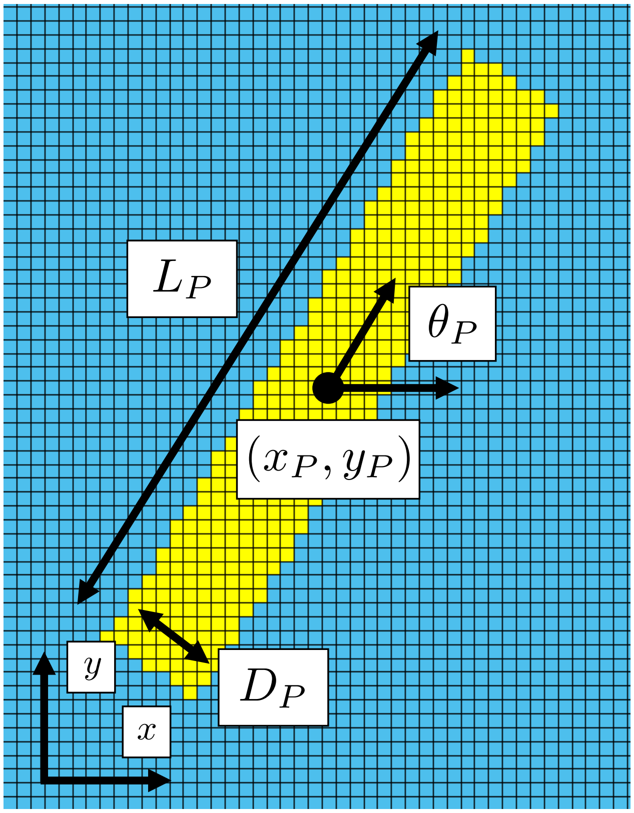

Figure 4.1: A platelet geometry within the partitioned domain. θ_p is the platelet orientation, x_p, y_p are the coordinates of the platelet center point, L_p, D_p represent the length and the width of the platelet.

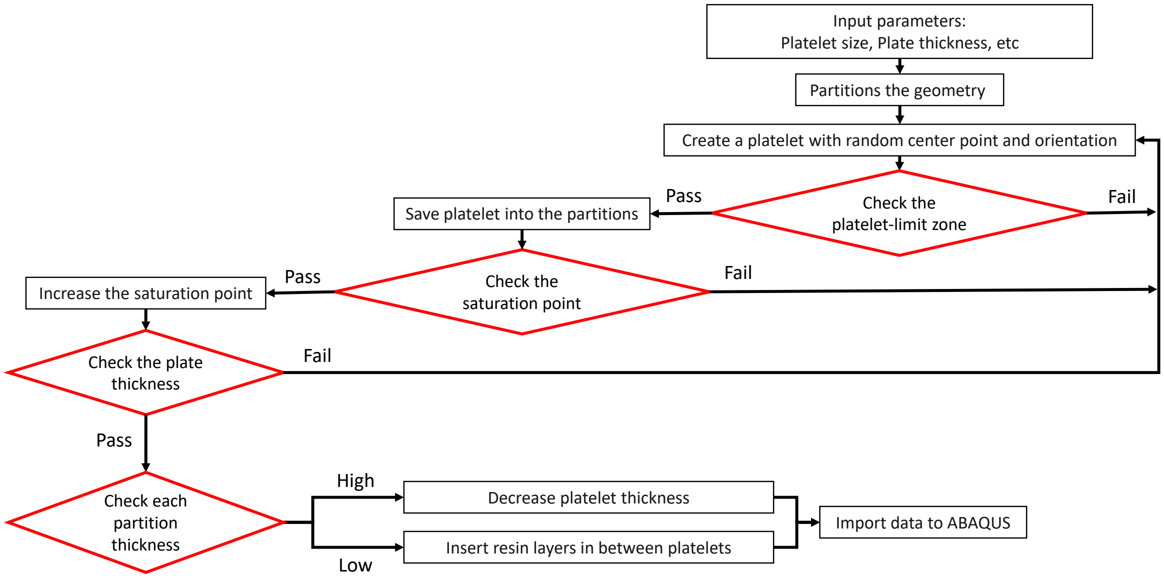

Figure 4.2: A flowchart of the random platelet meso-structure generation algorithm.

the platelet generations until the number of platelets through the thickness reaches the saturation points. If the condition is met, the saturation point moves to the next point until the final limit point (= 24).

Figure 4.4a shows the evolution of the average platelets as a function of the running time of the platelet distribution algorithm. A cascading trend is observed, with each step corresponds to the saturation points. The advantage of this algorithm is the accurate control of the CoV, resulting in a more realistic mesostructure as shown in Figs. 4.4b-d. As the result, the maximum and minimum numbers of the platelets through the thickness are 30 and 15 at the end of the platelet generation (see the color bar in Fig. 4.4d). Without such platelet distribution tactics, this contrast of platelet numbers can be far off from measured CoV, which is unrealistic.

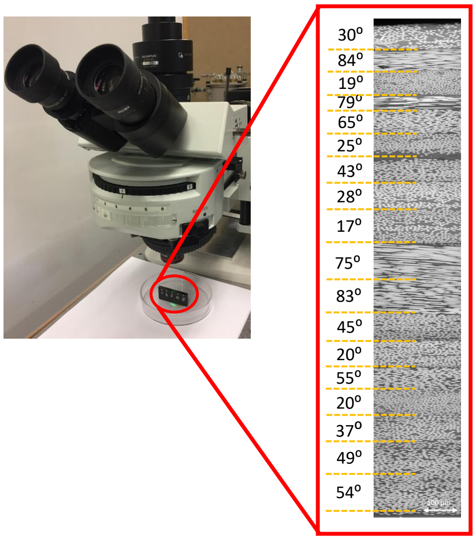

Figure 4.3: A sample image of the microscope study. We counted the number of platelets through the thickness in 90 different sample cross sections. For the coupon thickness of 3.3 mm, the average number of platelets is 24 with CoV of 22%.

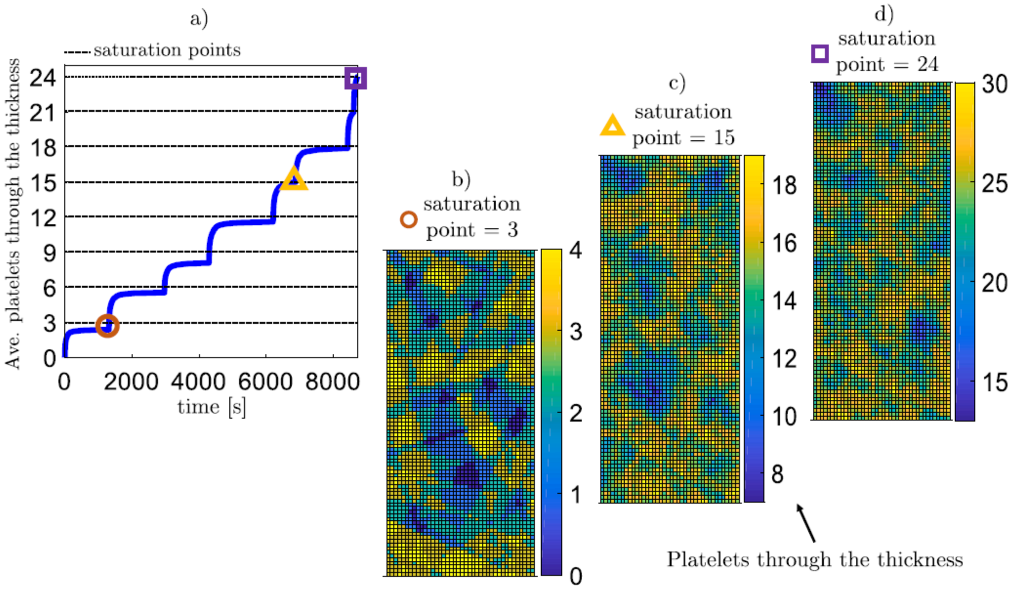

Figure 4.4: (a) The saturation limit points exist every 3 layers through the thickness. (b) Using the saturation limit points, we can control the statistical distribution of the number of platelets through the thickness.

4.2.1.2 Platelet thickness adjustment algorithm

Once the mesostructure is constructed within the desired CoV, the algorithm proceeds with the adjustment of the partitions thickness. This step is made necessary by the fact that the resin flow is not modeled explicitly. Accordingly, at the end of the algorithm, each partition will be characterized by a different thickness, in contrast to the fact that real DFC plates feature an almost uniform thickness. To overcome this issue, two possible conditions are addressed. (1) When the number of platelets exceeds the target average number, each platelet thickness is reduced linearly to match the target thickness (see Fig. 4.5a). This is assumed to be a valid assumption since, in reality, the platelets are compressed and spread out by the hot press machine to meet the average thickness. The deformation of the platelet geometry is neglected in this study. (2) If the number of platelets is lower than the target, instead of increasing the platelet thickness, layers of resin are introduced (see Fig. 4.5b). This is done to indirectly mimic the flow of the resin into the lower thickness regions (i.e., regions with the lower number of platelets). The resin layers are assumed to have the matrix system material properties of the T700G.

4.2.2 Random platelet spatial variation

Addition to the meso-structure generation algorithm, we implement the random platelet spatial variation to precisely control the statistical variation of the platelet orientation. It controls the platelet orientation locally varying in space. In DFCs, there are two important platelet orientation variation. One is through the thickness and the other is spatial variation. In Fig. 3.2 and 3.3, we observe the effects of the coupon thickness and platelet width. The coupon thickness effect is more related with the variation through the thickness. Meanwhile, the platelet width effect is more closely related to the variation in space. They are not independent to each other but one has a stronger impact than the other. The saturation point method implemented in the random platelet meso-structure generation controls the variation through the thickness. Here, we will explain how we control the variation in space

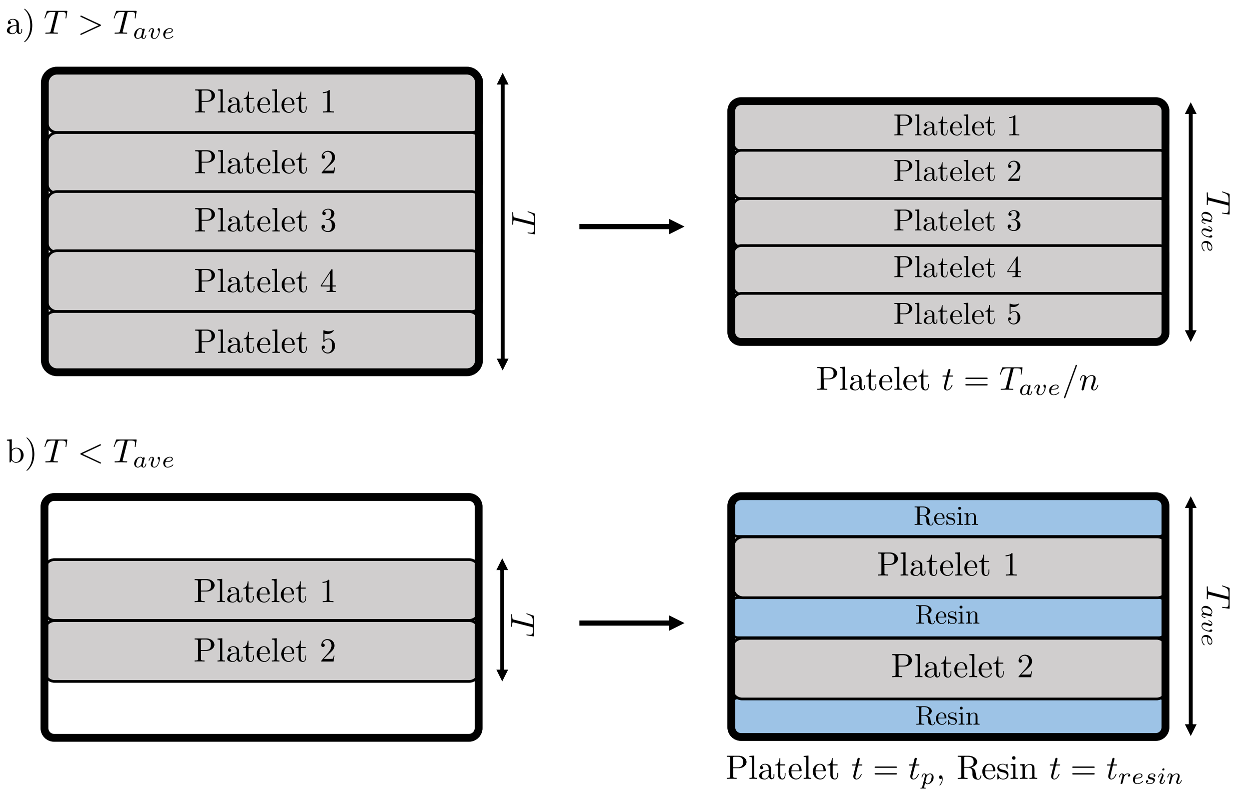

Figure 4.5: A summary of the thickness adjustment process. (a) When the local total thickness is higher than the target average thickness, we linearly reduce the individual platelet thickness to match the target average thickness. (b) When the local total thickness is lower than the target thickness, resin-rich layers are inserted to increase the total thickness.

using the spatial variation algorithm.

First, we study what is the actual fiber orientation variation over the space. We define the 3D platelet orientation tensor, A_{ij}, followed by [72]:

$$A_{ij} = \begin{bmatrix} A_{11} & A_{12} & A_{13} \\ ... & A_{22} & A_{23} \\ sym & ... & A_{33} \end{bmatrix} = \begin{bmatrix} p_1p_1 & p_1p_2 & p_1p_3 \\ ... & p_2p_2 & p_2p_3 \\ sym & ... & p_3p_3 \end{bmatrix}, where \begin{pmatrix} p_1 = sin(\phi)cos(\theta) \\ p_2 = sin(\phi)sin(\theta) \\ p_3 = cos(\phi) \end{pmatrix} \tag{4.1}$$

The direction 1 is the longitudinal direction (loading direction). The direction 2 is the transverse direction. The in-plane angle θ is positive from the direction 1 to 2. The out-of-plane angle ϕ is positive from the direction 3 to the plane 1-2 (see Fig. 4.6). The diagonal terms, A_{ii}, value from 0 to 1 and their summation equals to 1. We find the average orientation through the thickness using the following equation:

$$A_{ii,ave} = \frac{1}{N \cdot t_{tot}} \sum_{j=1}^{N} A_{ii} \cdot t_j \tag{4.2}$$

where n equals to the number of the platelets through the thickness. We exclude resin-rich layers when calculating the average orientation. Using $A_{ii,ave}$, we can easily represent the state of the randomness. When the platelets are oriented in a uniform random in all three directions, $A_{ii,ave} = 1/3$. When the platelets remain flat (2D case) and uniform random, $A_{11,22,ave} = 1/2$ and $A_{33,ave} = 0$. We refer this 2D uniform random state as an ideal manufacturing condition for the flat DFC coupons.

Many researchers have utilized the X-ray μCT scans to measure the fiber orientations. Based on the literature [58,59], we find that $A_{33,ave}$ is near zero (0.004 (3.6°) to 0.007 (4.8°)). In this study, the platelets are deposited perfectly flat ($A_{33} = 0$). Therefore, the $A_{ii,ave}$ can be simplified into only direction 1 and 2. Since their summation equals to 1, we can refer 2D average orientation tensor using a single parameter $A_{11,ave}$. When all the platelets are oriented towards the loading direction, $A_{11,ave} = 1$. If they are directed to the transverse direction, $A_{11,ave} = 0$.

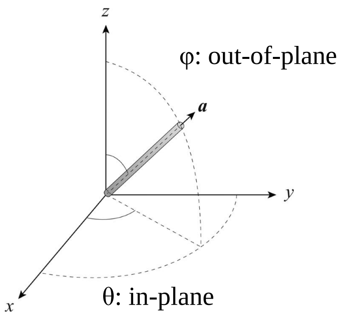

Figure 4.6: 3D coordination system of the platelet orientation.

From the X-ray μCT scan studies [58, 59], they also found that the $A_{11,ave}$ is close to 0.5 but locally varies. To measure the local variation, they subdivide 6" × 1" gauge length DFC coupons into 1" × 1" regions. In each region, they found the $A_{11,ave}$. An example of a DFC coupon with CT scan result is plotted in Fig. 4.7. From the square platelet DFC coupons, the $A_{11,ave} = 0.528$ and $A_{11,CoV} = 6.6\%$. From the narrow platelet DFC coupons, the $A_{11,ave} = 0.54$ and $A_{11,CoV} = 12.3\%$. We generated random meso-structures with identical platelet sizes to compare the average orientations. From the square platelet DFC coupons, we obtained the $A_{11,ave} = 0.50$ and $A_{11,CoV} = 5.4\%$. From the narrow platelet DFC coupons, we obtained the $A_{11,ave} = 0.50$ and $A_{11,CoV} = 2.3\%$. The random platelet meso-structure generation created precise 2D ideal random platelet orientations but the associated variation was underpredicted, especially for the narrow platelet size.

To control the spatial variation of the platelet orientation, we subdivide a coupon and enforce unique platelet orientation in each subdivision. Each subdivision or statistical representative volume elements (SRVEs) has a size of 1" × 1". We adapt the size from [58, 59]. However, we acknowledge that the statistics of $A_{11,ave}$ are depending on the size of SRVEs. We will further investigate how to choose the SRVE size in the future study.

In order to enforce unique $A_{11,ave}$ in each SRVE, we manipulate the boundaries of the

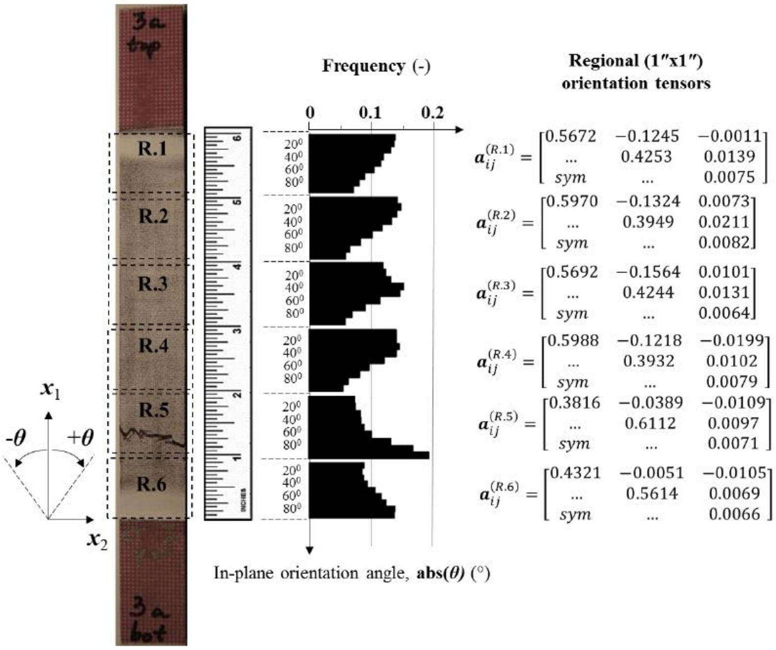

Figure 4.7: An example of the 3D orientation tensors obtained by Xray µCT scan from Kravchenko [59]. They subdivided a coupon into six 1” by 1” squares to obtain local orientation tensors. We adapted the size of the subdivision as the statistical RVE size.

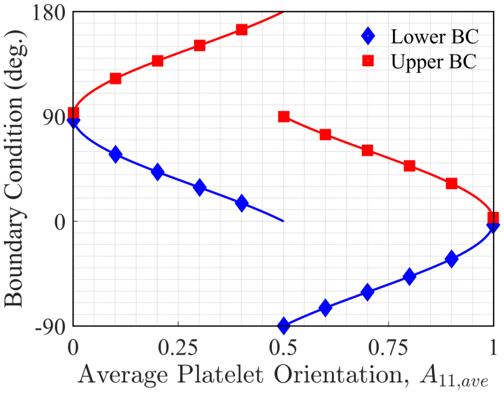

Figure 4.8: Lower and upper boundary conditions of the uniform distribution used to generate the platelets to match a target A_{11}.

uniform distribution which generate random platelet orientation. We can express the relationship between the $A_{11,ave}$ and the uniform distribution boundaries using a simple integral form. From Eq. 4.3, we find boundary conditions ($BC_{Lower,Upper}$) that provide the target $A_{11,ave}$.

$$A_{11,ave} = \frac{1}{BC_U - BC_L} \int_{BC_L}^{BC_U} cos^2(\theta) d\theta \tag{4.3}$$

For simplicity, we define the $BC_{L,U}$ to have same magnitude. For example, if $A_{11,ave} = 0.5$, then $BC_L = -\pi/2$ and $BC_U = \pi/2$ which correspond to the ideal manufacturing condition. Figure 4.8 shows the boundary conditions used to generate the $A_{11,ave}$. From this equation, we find the exact boundaries of the uniform distribution to match the target $A_{11,ave}$.

However, the target $A_{11,ave}$ is not always guaranteed because of the overlapping platelets between the SRVEs. It gets harder to match the target $A_{11,ave}$ as the platelet width decreases. A simple solution is to generate the SRVEs separately and combine them to create a coupon. However, this method creates sharp discontinuities between the SRVEs which is unrealistic.

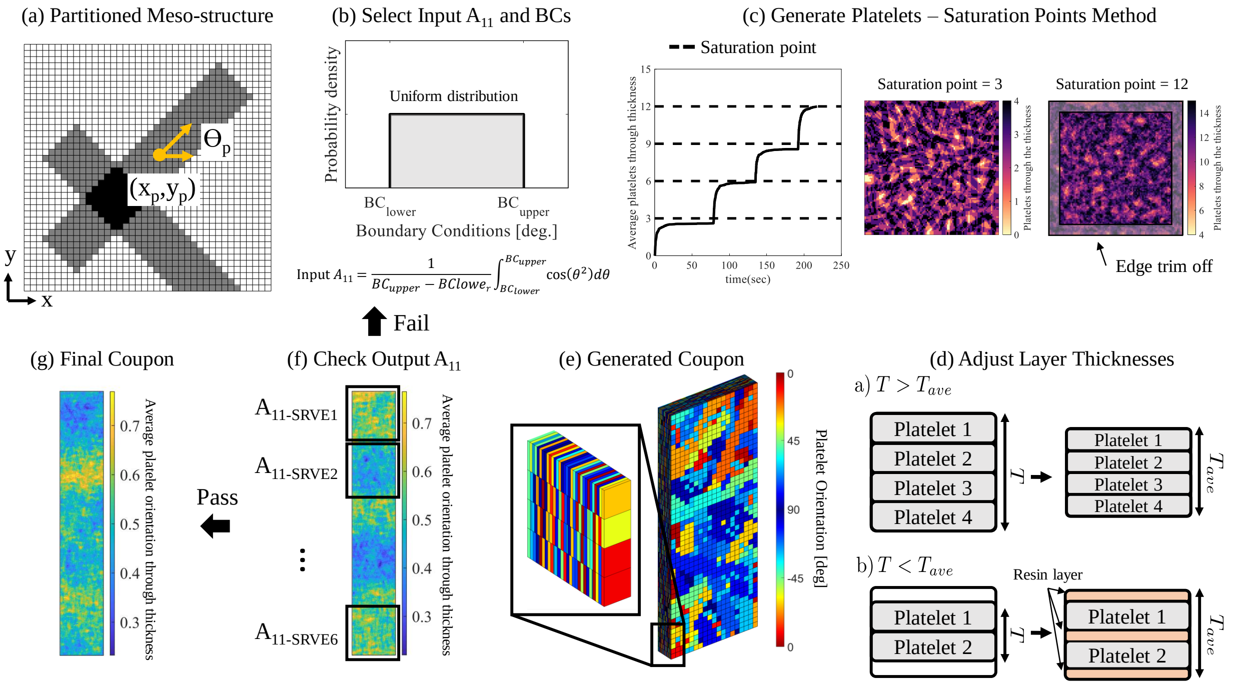

Figure 4.9: A graphical flowchart of the random platelet meso-structure generation. Using the generation algorithm, we control both average and variation of the explicitly generated platelet orientations.

We decide to generate the entire coupon as a single piece. To accommodate the effect of the overlapping platelets, we implement a bisection optimization algorithm. The optimization algorithm checks the difference between the current $A_{11,ave}$ and the target $A_{11,ave}$ in each SRVE. When the current $A_{11,ave}$ is lower than the target $A_{11,ave}$, we increase the input $A_{11,ave}$ by 0.01 until the difference flips the sign. We also reduce the increment by half. We iterate the process until the difference between the target and current $A_{11,ave}$ is less than 1%. We optimize all the SRVEs simultaneously. Equipped with the spatial variation algorithm, the random platelet meso-structure generation can controls the platelet orientation variation through the thickness and over the space. A complete graphical flowchart of the meso-structure generation is plotted in Fig. 4.9.

4.2.3 Stochastic finite element framework

We transform the meso-structures into finite element models using Abaqus [73]. A schematic of the FE model is plotted in Fig. 4.10. As shown in Fig. 4.10, we prioritize capturing the failure mechanisms in the DFC coupons. In the DFC coupons, there are intra-, and inter-laminar fractures. Intra-laminar fracture involves the failure within the platelets such as fiber breakage, fiber pull-outs, and matrix damages. Often these damages start to accumulate prior to the ultimate failure. Micro-cracks accumulate and form a macro-crack leading to the structural failure. Therefore, the damage process in the quasi-brittle materials such as CFRPs, concrete, ceramics, rocks, sea ice, and nanocomposites are complex and progressive [36, 37, 39, 51, 74].

For the intra-laminar damages, we use continuum damage mechanics approach where the damage is smeared over the element. The material degradation is modeled by strain softening constitutive law. We use Hashin failure criteria as a damage initiation, and linear damage softening law for the progression of the damage [75, 76]. The intra-laminar damages are simulated using the Belytschko-Tsai shell elements with reduced integration (S4R in the Abaqus). Each partition from the meso-structures is treated as a shell element containing unique fiber orientation and thickness.

For the inter-laminar damages, we use the cohesive zone model. A linear elastic traction-separation constitutive behavior is used [77]. For the damage initiations, we use the quadratic stress failure criteria. For the damage progression, a linear softening law with Benzeggagh-Kenane (BK) mixed mode was used. We used BK exponent of 2 as suggested by [78]. The inter-laminar damages are simulated using the 3D, 8-nodes cohesive elements (COH3D8 in the Abaqus). A layer of cohesive elements with thickness of $1/100^{th}$ of the prepreg ply thickness is inserted between the shell elements. Abaqus regularized both constitutive laws using the Crack Band Model [36, 79] in order to avoid any false energy dissipation. A single side of the shell elements and the cohesive elements share common nodes, creating a laminate. Between the laminates, a perfect bonding constraint is applied to create a coupon.

The platelet material properties used in this study are undisclosed due to the company proprietary. However, we use similar material properties from [24]. For the cohesive element properties, the penalty stiffness in normal and two shear direction are chosen to be 1.0×10^5 N/mm^3 [80]. The strengths are equaled to 320 MPa in all three directions as well. The normal and shear fracture energies are 1.4 and 2.4 N/mm. The cohesive material properties are used to calibrate the model to match the the experiment results from the narrow platelets with 0.15" thickness. Uni-axial displacement is applied at the end of the specimen while the other end is fixed in all directions. A mesh size of 0.02" × 0.02" is used to match the partition size. We use the explicit integration method.

4.3 Computational Modeling Results

4.3.1 Computational analysis results

We investigated the tensile elastic modulus and strength using the ideal manufacturing condition first. We extended the investigated thickness up to 0.5" (91 layers through thickness) to fully cover wide enough thickness range. We simulated 30 coupons per thickness. The results are showing in Fig. 4.11 and Fig. 4.12. The simulation averages match the experiment results in both tensile modulus and strength. Thanks to the computational analysis, we find out that the modulus and strength reach the asymptotic level after the thickness of 0.25" (45 layers through thickness). At 0.5" thickness, the normalized modulus of both platelet sizes reach 0.97. For the strength, they reach 0.49 for the narrow and 0.45 for the square (only 7% difference). To summarize, the platelet width effect diminishes in both modulus and strength after DFC coupons reach the asymptotic thickness of 0.25". Therefore, engineers and designers must choose the structure thickness carefully in order to avoid the thickness effect and the platelet width effect.

Similar to the experiment, the simulated modulus and strength CoVs follow a decreasing trend as the thickness increases. However, the magnitudes of CoVs are significantly under predicted in all the thicknesses and the platelet sizes. At the 0.15" thickness, the narrow

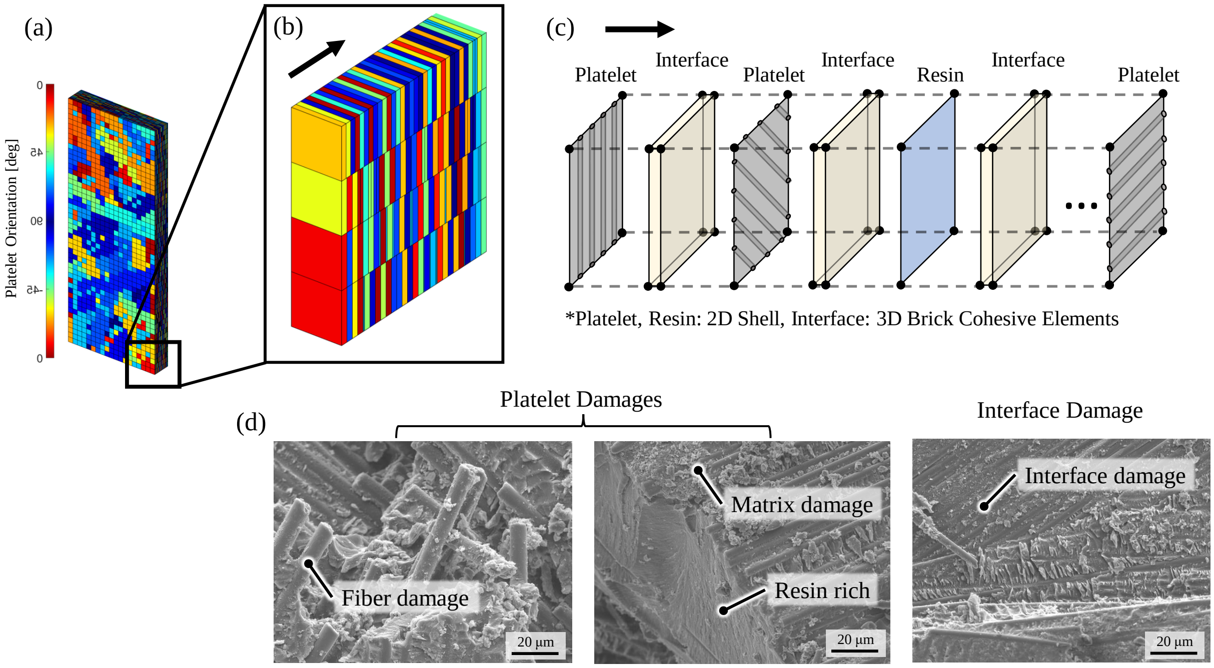

Figure 4.10: A summary of the stochastic finite element model framework. From the random platelet meso-structures (a - b), individual layers are modeled using 2D shell elements (c). Between the shell elements, the cohesive elements are inserted to represent the interface layers. Using this approach, we are able to capture three main failure mechanisms that we observed from SEM (d).

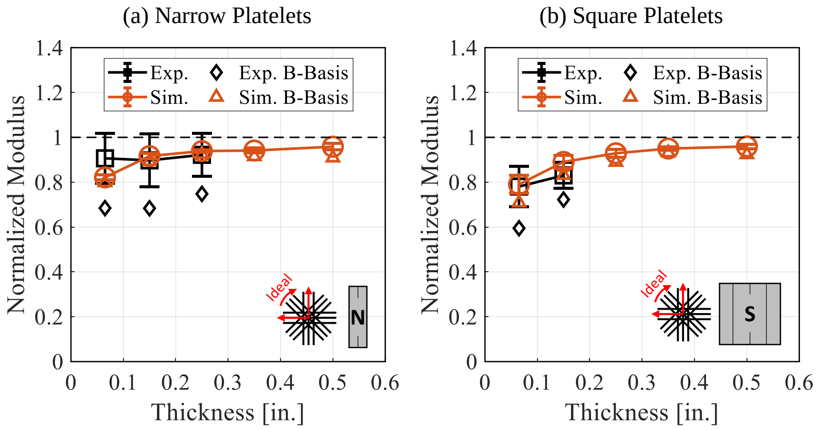

Figure 4.11: A summary of the modulus thickness effect of the narrow and square platelets. The thickness effect in the tensile elastic modulus is insignificant for both platelet sizes. The modulus reaches the asymptotic limit at the thickness of 0.25”. At the asymptotic limit, the modulus difference between two platelets is negligible.

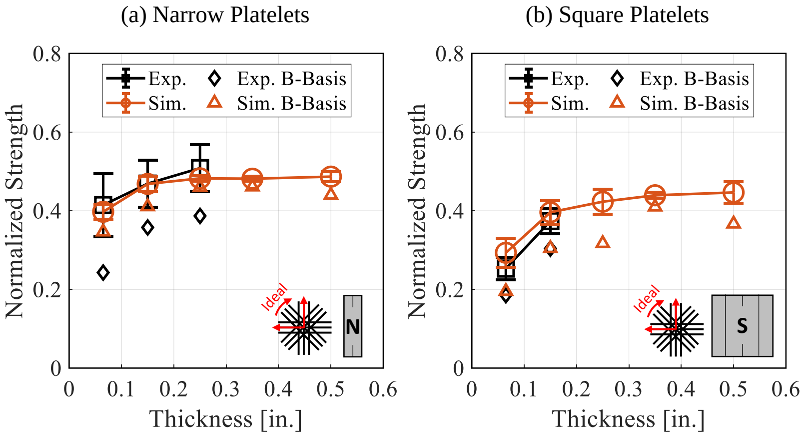

Figure 4.12: A summary of the strength thickness effect of the narrow and square platelets. A significant thickness effect is observed in both platelet sizes. The strength reaches the asymptotic limit at the thickness of 0.25". At the asymptotic limit, the strength difference between the two platelets is only 7 percent.

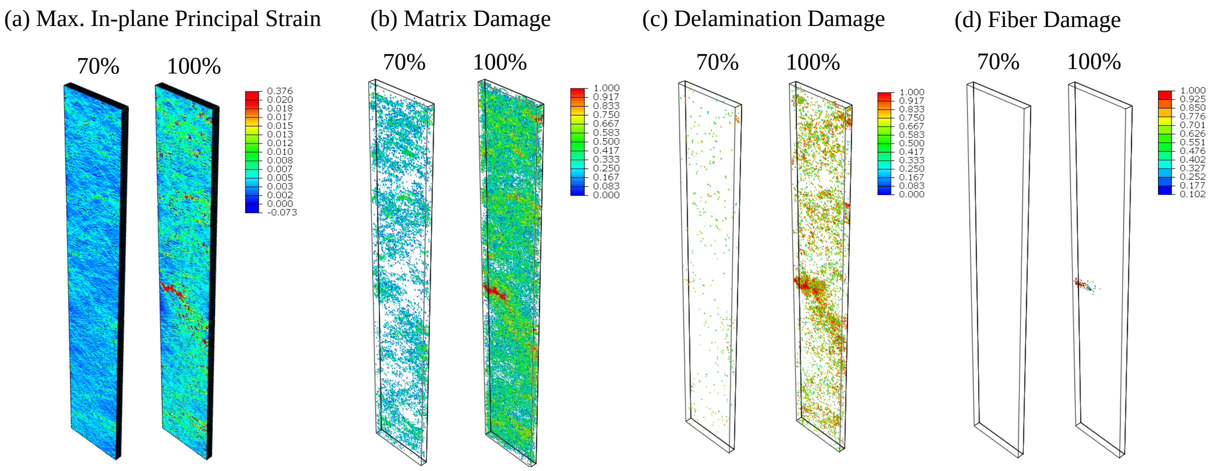

Figure 4.13: Three major failure mechanisms of DFC coupon. The percentage represents the current load status compared to the maximum load. Matrix damage is the dominant failure mechanism followed by the delamination. The fiber damage is the least affecting damage mechanism in DFC coupon.

platelet has the modulus CoV of 12% from the experiment but only 1.2% from the simulations. The square platelet has 7% from the experiment and 3.2% from the simulations. Such discrepancies are due to the ideal platelet orientation where the spatial variation is not considered. The CoVs of the strength and modulus are closely related with the local spatial variation of the platelet orientation. Using the ideal orientation generation, such variations are tightly limited, resulting significantly lower CoVs. We closely investigate the effect of the platelet orientation variations in the following section.

4.3.1.1 Effect of the platelet orientation variations

To find the platelet orientation variations, we first find the average platelet orientation ($A_{11,ave}$) within SRVEs size of 1" × 1". SRVE serves as a smallest unit of the statistical sample size. Then we define two orientation variations. Global orientation variation finds the CoV of $A_{11,ave}$ from the entire SRVE population. If there are 10 coupons with 6 SRVEs each, the entire SRVE population size is 60. Local orientation variation measures the CoV of $A_{11,ave}$ from SRVEs within a coupon. Using the global orientation variation, we can easily manipulate the statistical variation within and in between DFC coupons.

Without the spatial variation, the global orientation variation is $\sim 2\%$ for the narrow platelets and $\sim 5\%$ for the square platelets. We perform a parametric study by increasing the global variation. Assuming that the platelet orientation, A_{11}, follows the normal distribution, we set the mean at 0.5 and increase the CoV from $2, 10$, and 15%. To efficiently assign $A_{11,ave}$ into SRVEs, we use the Latin-Hypercube Sampling (LHS) [81] method. The LHS is chosen because it guarantees to cover the two end-tails of the probability distribution. We calculate the cumulative density function (CDF) from the selected mean and CoV. The CDF is divided into equal spaces, called stratifications. The total number of the stratification equals to a number of SRVEs per coupon (6) times a total number of coupons. We simulate 30 coupons per CoV to have enough stratifications. Within a stratification, a random point is selected. This random point corresponds to a specific CDF value and therefore unique A_{11}. Finally, we assign 6 random A_{11}s into a coupon until all coupons have assigned A_{11}s. In Fig. 4.14, we illustrate the process of LHS method. Using the LHS, we can easily control the global orientation variation of the entire coupon population.

Increasing the global orientation variation directly affects the local orientation distributions of the platelets. In Fig. 4.15, we increase the global orientation CoV from 2% to 10%. Simulated coupons have the narrow platelets with 0.15" thickness. We can clearly notice A_{11} variation within a coupon as the global orientation CoV increases. Increasing the orientation variation induces regions with poorly oriented platelets. These weak spots will trigger the fracture at lower strength. We plot the normalized modulus and strength against the local orientation variation in Fig. 4.16. All coupons have a thickness of 0.15" with the narrow platelets. Solid lines represent the averages and dashed lines represent one standard deviation. Clearly, the strength and the modulus decreases as the local orientation CoV increases. The average strength is reduced more than the average modulus because the strength is more sensitive to the presence of local weak spots [51–53, 82].

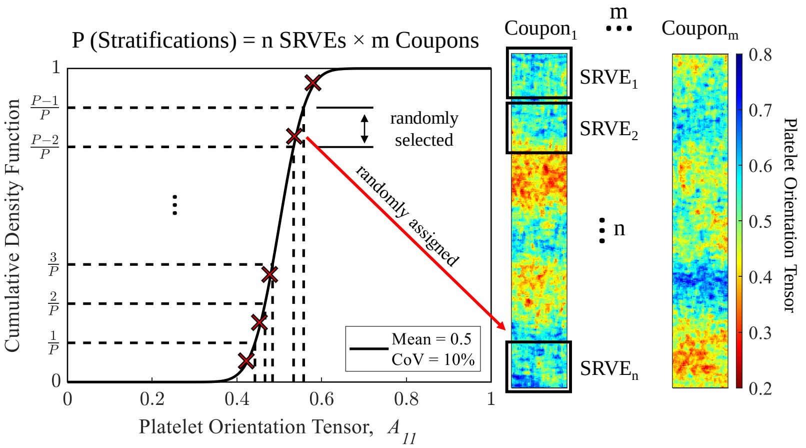

Figure 4.14: We use the Latin Hypercube Sampling (LHS) method to create coupons with random A_{11}s. control the global platelet orientation variation following the given mean and variation.

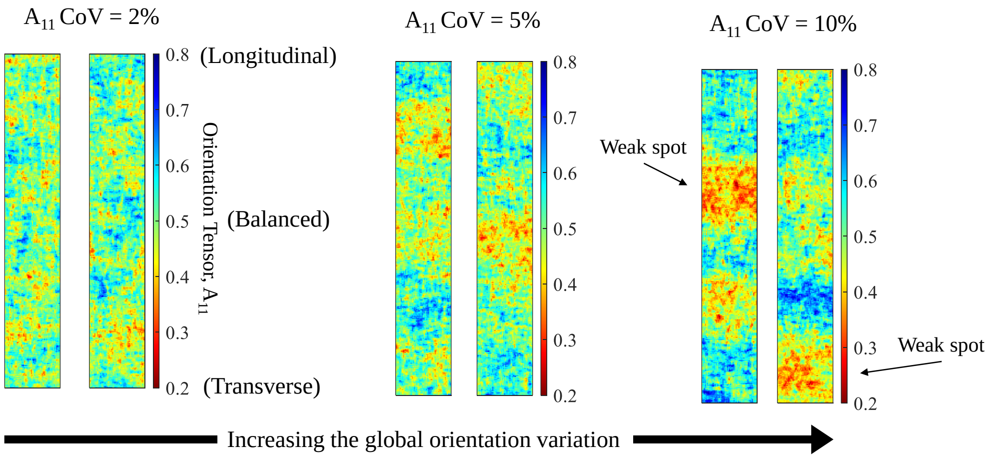

Figure 4.15: Visualization of the platelet orientation distribution with different global orientation variations. When the global variation increases, it shows that the DFC coupons have noticeable regions with poorly oriented platelets (local weak spots). The average coupon orientations remain relatively constant.

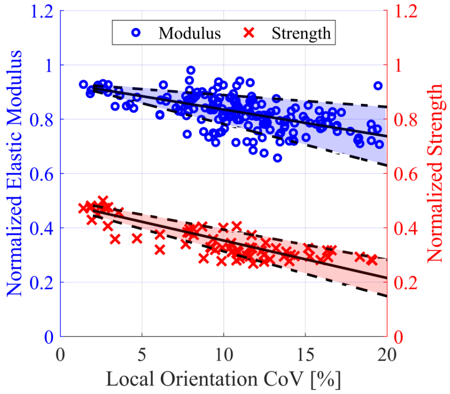

Figure 4.16: Simulated normalized modulus and strength against the local platelet orientation variation. Increasing the local platelet orientation variation decreases the average modulus and strength (solid line) while increasing their variations (dashed lines). The narrow platelets with coupon thicknesses of 0.15” are simulated. The square platelets also possess similar trend.

From the Fig. 4.16, we observe the effect of the platelet orientation variation on the mechanical properties of DFCs. Besides the orientation variation, there is another important meso-structure characteristic that define DFC structures, which is the average platelet orientation. The average platelet orientation determines the coupon modulus according to many studies [10, 12–14, 57, 59–61, 65, 67, 68, 83]. We combine two different meso-structure characteristics and plot the modulus and strength changes. We plot contour maps of the modulus and strength in Fig. 4.17. We used a Delaunay triangulation to perform the interpolation in Matlab [84]. Comparing between the Fig. 4.17a and b, the contour lines in the modulus are tilted more horizontally than the strength. For the modulus, the average platelet orientation is the dominating parameter. However, the effect of the orientation variation is not negligible. We can explain this relationship with a series coupling of individual SRVEs. As described in Eq. 4.4, each modulus in SRVE contributes to the equivalent modulus [85].

$$E_{equivalent} = \left(\sum_{i=1}^{N} \frac{1}{E_i} \right)^{-1} \tag{4.4}$$

Because this equation is composed of the product and summation of each modulus in SRVE, both average and variation of the modulus are important. The modulus and the platelet orientation, A_{11} are also directly related. Therefore, to accurately predict the modulus, we need both average platelet orientation and their CoVs. In case of the strength (see Fig. 4.17b), the platelet orientation CoV plays more significant role than the average orientation. Compared to the modulus, the strength contour lines are tilted more vertically. Unlike the modulus, the strength is more dependent on the individual SRVE's probability of survival. If a single SRVE fails, the whole structure fails [51–53, 82]. It can be simply described as a weakest link chain model described in Eq. 4.5. where $P_f(\sigma_N)$ is the failure probability in given nominal stress.

$$P_f(\sigma_N) = 1 - \prod_{i=1}^{N} (1 - P_{fi}(\sigma_N)) \tag{4.5}$$

The weakest SRVE or the SRVE having the most poorly oriented platelets governs the strength of the coupon. Therefore, the average platelet orientation alone is limited to indicate the strength of DFC structures.

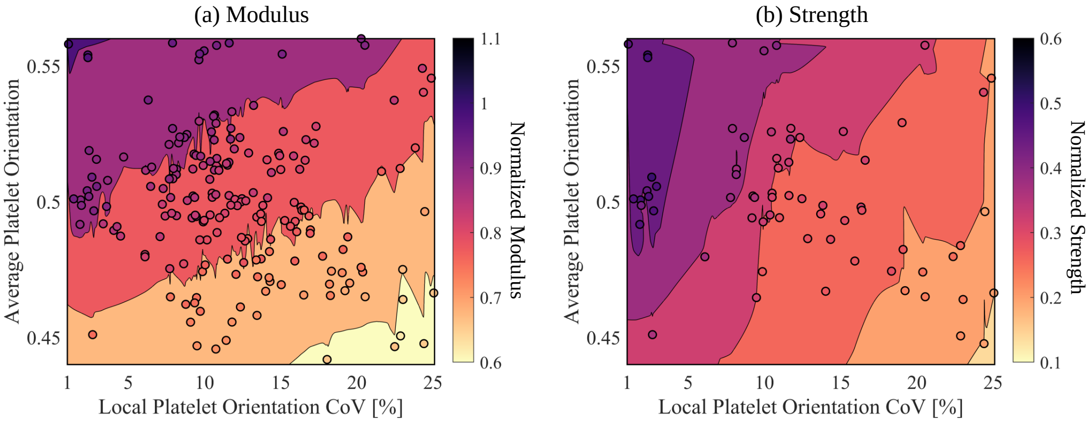

Figure 4.17: Simulated (a) normalized modulus and (b) normalized strength against the local platelet orientation variation and the average platelet orientation. Comparing the slopes of contour lines in (a) and (b), we can determine the dominating parameter for the modulus and strength. (a) In the modulus, the average platelet orientation is the dominating parameter. As a result, the contour lines are more horizontally tilted. However, the variation also plays a significant role where it can significantly reduce the modulus. (b) In the strength, the local platelet orientation variation is the dominating parameter. We observe that the contour lines are more vertically tilted. Having a high CoV significantly reduces the strength. However, we must understand that both average and variation of the platelet orientation significantly affect the modulus and strength.

4.3.1.2 Matching the modulus and strength variations

As can be seen in Fig. 4.16, the global orientation variation affects the modulus and strength variations. By manipulating the global orientation variation, we can match the modulus and strength variation from the experiment (see Fig. 4.11, 4.12). We take the advantage of the spatial variation algorithm to calibrate the meso-structures with different global orientation variations. Both platelet sizes are simulated with coupon thickness of 0.15". At least 20 coupons are simulated per global orientation variation. The results are plotted in Fig. 4.18. By manipulating the global orientation variation, we can control the modulus and strength variations. In case of the narrow platelets, we reach the experimental variation using the 15% orientation CoV. Without calibrating the spatial distribution of the platelets, such variations are hard to obtain. However, we observe noticeable reduction of the average strength as the orientation CoV increases. We believe this mismatch is due to the fact that we assume the size of the SRVE is 1" × 1". Changing the size of the SRVE will affect the average and variation of the strength. We will investigate such effect in the future study. In the square platelet, we successfully match both average and variation associated with the tensile modulus and strength. We use the average platelet orientation at 0.5 and the global orientation variation of 10% as the calibration parameters. This results indicate that if we know the statistical information of the platelet orientation prior to the experiment, we can predict not only the average but also the associated variation of both modulus and strength of DFC coupons. It will significantly reduce the required number of proof testing in order to certify this stochastic material properties.

To validate the computational results, we use the X-ray μCT scans to find the statistical information of the platelet orientations. We compare the global orientation variation used it to calibrate the meso-structure against the measurement directly from the CT scans.

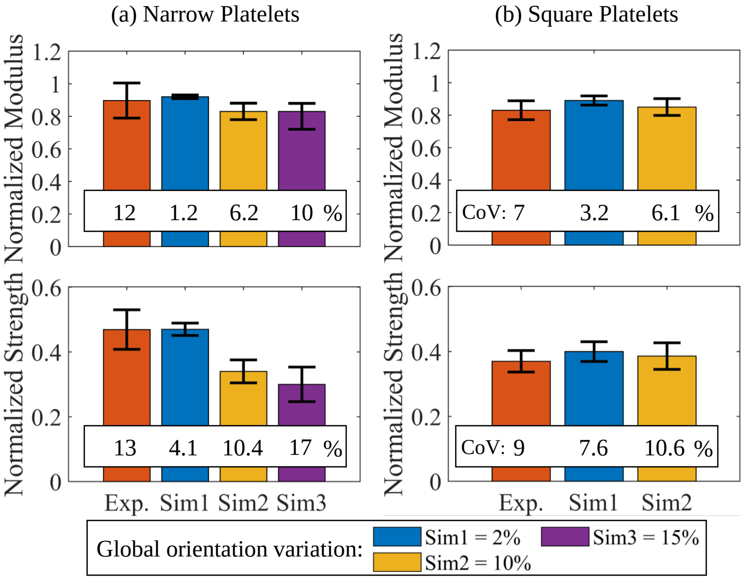

Figure 4.18: Normalized modulus and strength with meso-structures made of different platelet orientation variation. For (a) the square platelets, the meso-structure with input A_{11} CoV of 10% precisely match the modulus and strength variation from the experiment. However, for (b) the narrow platelets, CoV of 10% still underpredicts the variation from the experiment. In fact, it is difficult to match both modulus and strength CoV using a single input CoV.

4.3.1.3 Find the platelet orientation distribution using the X-ray micro Computer Tomography (CT) scan

We measured the platelet orientation distribution using the Xray μCT scan. We scanned 5 square platelet coupons at the thickness of 0.15". We used NSI X5000 scanner with scan resolution of 25 μm. Reconstruction of the scanned images were processed using the VGStudio Max [86]. There were several methods to calculate the orientation tensors of DFCs using the μCT scan [55,58,60,61]. We chose to adapt the work done by Denos *et al.* [10,58,87]. Denos *et al.* calculated the gradient density difference between the adjacent voxels and correlated with the platelet orientation tensors. We used 3D Gaussian distribution derivative filters to find the local density gradients. A Gaussian smoothing filter was used to reduce the noise.

We averaged platelet orientation within SRVEs. As expected, the $A_{33,ave}$ was near zero (0.0032). Therefore, we assumed $A_{33,ave} = 0$ and obtained $A_{11,ave}$. Total of 30 SRVEs were measured from the square platelet coupons. The $A_{11,ave} = 0.49 \pm 9.3\%$. As can be noted, the measured $A_{11,ave}$ CoV is very close to the global orientation variation that we used to calibrate the meso-structures (10%). This μCT scan measurement confirms that using the statistical distribution of $A_{11,ave}$ from SRVEs, we can find the average and variation of the tensile modulus and strength of DFC coupons.

4.3.1.4 Effect of the resin-rich percentage

Besides the platelet orientation, we also investigate the effect of the resin-rich layers. Large amount of the resin-rich layers are unavoidable meso-structure characteristic of DFCs due to the discontinuity of the platelets. It occupies $5 \sim 10\%$ of the total volume [9, 88] but often overlooked because of the platelet orientation. Wan and Takahashi [13] experimentally showed that the tensile and compressive strength changed with respect to the fiber volume fraction. They measured the fiber volume fraction with respect to the molding pressures at 5 and 10 MPa. When the pressure was reduced, the fiber volume fraction also reduced from $\sim 56\%$ to $\sim 50\%$. The decreased fiber volume fraction aligned with the reduction of the tensile and compressive strength. We further extend the effect of the resin-rich layers leveraging the comprehensive random meso-structure generation algorithm.

From the algorithm, we indirectly control the total percentage of the resin-rich layers. In the generation algorithm, we limit the number of maximum platelets that can be deposited in the partitions. Currently, the maximum limit is set as the one standard deviation (or CoV = 22%) above the target average. This value is experimentally determined from the previous studies [29, 30]. By changing the maximum limit of the platelets, we can vary the percentage of the resin-rich layers. We varied the resin-rich percentage from 4 $\sim$ 8%. The simulated coupons had the narrow platelets, thickness of 0.15" and no spatial variation to explicitly observe the effect of the resin-rich layers only.

In Fig. 4.19, the average modulus and strength with respect to the resin-rich percentage are plotted. The figure shows a clear linear decreasing trend of the modulus and strength as the resin-rich percentage increases. The dashed line represents a linear fit of the modulus and strength. As can be noted, a small percent change, from 4 to 8%, of the resin-rich layers causes a significant reduction (25%) of the strength. The resin-rich layers have direct impact to the mechanical performances of DFCs. To minimize the effect of the resin-rich layers, we recommend to precisely optimize the molding pressure.

4.3.2 Platelet width effects

From the experiment (see Fig. 4.11,4.12), we observe significant reduction in the tensile strength as the platelet with increases. In this section, we discuss what are the meso-structure characteristics that drive such platelet width effect. We simulated four different platelet widths at the coupon thickness of 0.15". We simulated 10 coupons per platelet width. In Fig. 4.20a, the tensile stiffness and strength of different platelet widths are plotted. As the platelet width increases by $\sim$ 8 times, the tensile strength is decreased by 17%. The stiffness is much less affected. We observe three meso-structure characteristics. They are the average platelet orientation, local orientation variation, and resin-rich percentage. As the platelet width changes, the average platelet orientation and the resin-rich percentage remain

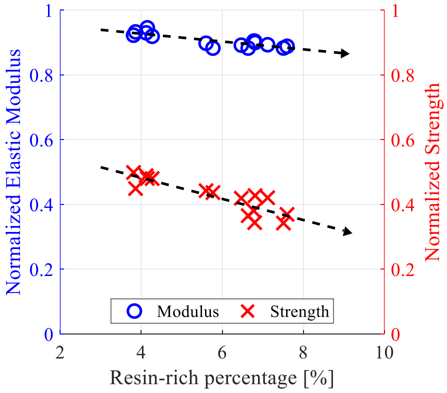

Figure 4.19: Simulated normalized modulus and strength against varying resin-rich percentage of an entire coupon volume. The resin-rich percentage significantly penalizes the strength of DFC coupons. The narrow platelets with coupon thicknesses of 0.15” are simulated.

relatively constant but the local orientation variation significantly changes. As can be seen in Fig. 4.20b, the local orientation variation is increased more than double. Increasing the local orientation variation reduces the strength by introducing the local weak spots (see Fig. 4.15,4.17). Therefore, the narrow platelets are recommended not only because they have the manufacturing advantage, but also they possess higher tensile strength.

4.3.3 Structure thickness effects

Kravchenko et al. [23, 24] pointed out that the thickness effect was due to the change of uniformity of the local orientation state. Similar to the platelet width effect, we investigate the three meso-structure characteristics with respect to the coupon thickness. We simulated 30 coupons made of the narrow platelets. The local orientation variation and the resin-rich percentage are strongly affected by the coupon thickness while the the average platelet orientation remains close to 0.5 in all cases. In Fig. 4.21, we plot the results. As the coupon

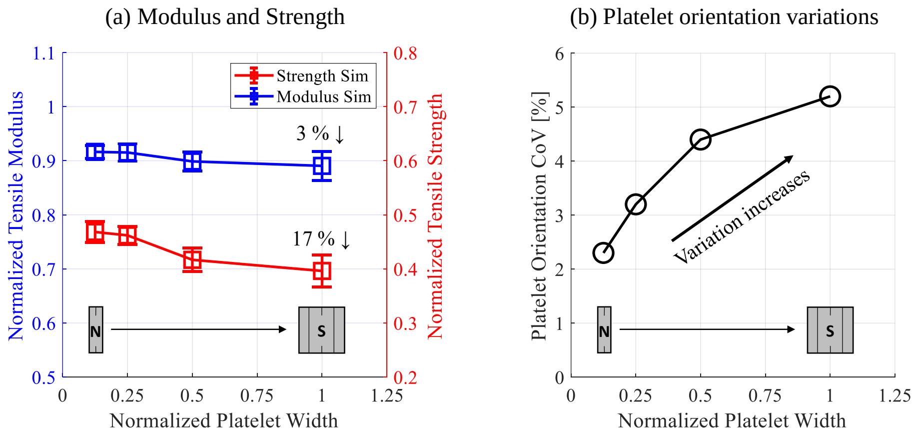

Figure 4.20: (a) As the platelet width increases, we observe reduction in the modulus and strength. The strength reduction is especially noticeable. (b) As the platelet width increases, the meso-structures introduce higher local platelet orientation variations. Higher variation creates local weak spots. Therefore, the coupon strength reduces as the platelet width increases.

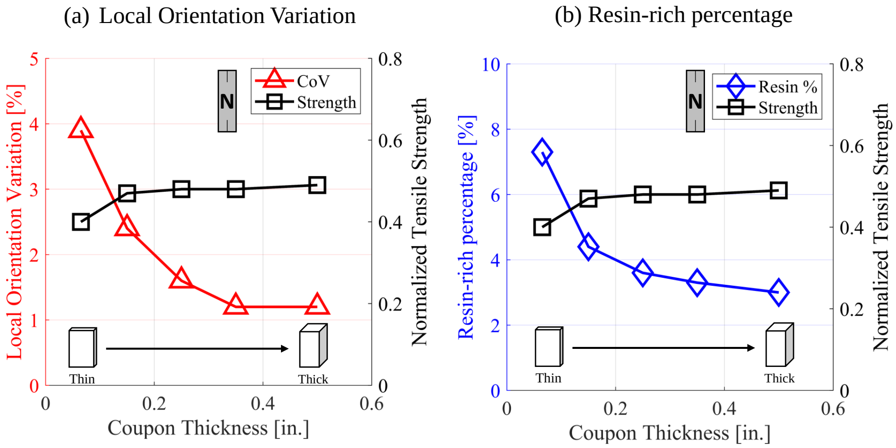

Figure 4.21: As the coupon thickness changes, we observe two meso-structure characteristics change. (a) The platelet orientation variation decreases and (b) resin-rich percentage also decreases as the coupon thickness increases. Increasing the coupon thickness significantly benefits the strength because it reduces having a chance of local weak spots.

thickness increases, the tensile strength increases until the thickness of 0.25”. We clearly see that both local orientation variation and the resin-rich percentage decrease as the the coupon thickness increases. Especially, the resin-rich layers decrease drastically as the thickness increases. By increasing the coupon thickness, the DFC coupons reduce the probability of having the poorly oriented regions as well as the resin-rich layers which can trigger the fracture.

4.4 Conclusion

1. Using the stochastic finite element models, we capture the thickness effect in both modulus and the strength. We extend the coupon thickness up to 0.5” (91 layers). Both platelet sizes reach the asymptotic modulus and strength after the thickness of 0.25”. At the asymptotic limit, the platelet width effect and the structure thickness effect

become negligible. After the asymptotic thickness limit of 0.25”, the modulus reaches 96% of the theoretical modulus of quasi-isotropic (QI) laminate. For the strength, the narrow and the square platelet reach 49% and 45% of the QI laminate strength.

2. Leveraging the computational modeling equipped with the spatial variation of the platelets, we study the effect of the local orientation variation within coupons. For both modulus and strength of DFC structures, the average platelet orientation and the local platelet orientation variation play significant role. However, in the modulus, the average platelet orientation plays a dominant role. Vice versa, the local orientation variation plays a dominant role in the strength. Therefore, we must consider both characteristics when relating the DFC meso-structures to their tensile material properties.

3. Additional important meso-structure characteristic that defines the DFC material properties is the percentage of the resin-rich layers. The thickness effect is caused by both the change in the local platelet orientation variation and the resin-rich percentage. The two characteristics significantly change as the thickness varies up to the asymptotic thickness limit of 0.25” (45 layers). The platelet width effect is mainly caused by the change in the local platelet orientation variation.

4. Lastly, we suggest two meso-structure calibration methods to accurately capture both average and variation of the material properties. First is to calibrate the meso-structures against the experimental results. Using the Latin-hypercube sampling method, we find the accurate platelet orientation variation associated with the meso-structures. Second is to use the Xray μCT scans to directly obtain the platelet orientation distributions. Two independent methods will provide accurate estimation of the B-basis design values for engineers and designers.

Chapter 5

EFFECT OF THE PLATELET SIZE ON THE FRACTURING BEHAVIOR AND SIZE EFFECT OF DISCONTINUOUS FIBER COMPOSITE STRUCTURES

5.1 Introduction

Composites reinforced by randomly oriented platelets or chopped fibers, generally called Discontinuous Fiber Composites (DFCs), offer several advantages over traditional unidirectional composites. Not only do they feature a relatively pseudo-ductile behavior [9,13,22,50,89,90], but they also enable the manufacturing of parts in complex shapes without the need for machining or the use of adhesives [91, 92]. This is thanks to significant formability, unmatched by traditional unidirectional carbon fiber composites, which makes the use of compression molding a highly viable option even for very complex geometries [93–95]. This enables almost net-shape designs with minimum waste of materials [95]. Further, the platelet-based geometry opens new avenues for recycling uncured prepreg materials [11, 96] and developing hybrid laminates with continuous fibers to achieve unprecedented mechanical properties and formability [69]. These characteristics broaden the use of DFCs for applications that have been typical of light alloys, such as secondary structural components for aerospace [17,93,95], body frames of terrestrial vehicles [17, 91, 92, 94], composite brackets, suspension arms and interiors [94] and crash absorbers [17, 91, 94].

Considering the remarkable properties of DFCs, it is not surprising that the scientific and industrial communities devoted significant efforts to understanding their mechanical behavior and developing proper design guidelines. Since the pioneering work of Halpin and Pagano [72], significant progress have been made on the experimental and computational characterization of the DFC mesostructure [10,25,56,58], and the understanding of the influence of the platelet morphology on the elastic properties and strength of DFCs [9, 22, 24, 50, 55, 89, 90, 97].

Notwithstanding the remarkable work on DFCs performed in the last decade, several challenges still need to be overcome. For instance, while a large bulk of data on the mechanical properties of DFCs is available already, an aspect overlooked in the literature is the fracturing behavior and its scaling effect. It is interesting that, to date, no estimates on the fracture energy and its relation to the platelet morphology is available in the open literature. This is a serious issue since the design of complex-shaped DFC components featuring holes, notches, and other stress raisers requires a thorough understanding of the fracturing process and its size effect in particular.

Since the DFCs are the quasibrittle structures, i.e., structures made of complex, heterogeneous materials with non-negligible inhomogeneities. For typical engineering applications, materials that lead to a quasibrittle behavior include concrete [33, 34, 36], composites [35, 37, 42], and nanocomposites [38–40, 43–45]. In quasibrittle structures, the size of the non-linear Fracture Process Zone (FPZ) occurring in the presence of a large stress-free crack is usually not negligible [33–41]. Particularly in DFCs, the stress field along the FPZ is nonuniform and decreases with crack opening due to discontinuous cracking, delamination and frictional pullout of platelets [31,32]. As a consequence, the fracturing behavior and, most importantly, the energetic size effect associated with the given structural geometry, cannot be described by means of the classical Linear Elastic Fracture Mechanics (LEFM). To capture the effects of a finite, non-negligible FPZ, the introduction of a characteristic (finite) length scale related to the fracture energy and the strength of the material is essential [33–39, 41].

Another aspect that makes the characterization of the fracturing behavior of DFCs particularly challenging is the significant role played by the platelet morphology, especially the platelet size and its spatial random distribution throughout the structure. In fact, the random orientation distribution of platelets leads to significant spatial variability of the mechanical properties as well as of the local stress field [9, 32]. In particular, the final failure caused by damage localization is often initiated by the presence of weak spots rather than stress raisers such as cracks or notches. The location of these weak spots is dictated by the spatial randomness of both local material resistance and applied stress field.

In consideration of the foregoing knowledge gaps, this study presents an investigation of the intra-laminar fracture and size effect in DFCs for three platelet sizes (75×12, 50×8, and 25×4 mm). The size effect on the structural strength of geometrically-scaled Single Edge Notch Tension (SENT) specimens is characterized for the first time, showing that neither stress-based failure criteria nor LEFM can solely capture the scaling effect. To capture the size effect and characterize the fracture energy, G_f, and the effective length of the fracture process zone, c_f, an approach combining equivalent fracture mechanics and stochastic finite element modeling is proposed in this study. The model accounts for the complex random mesostructure of the material by modeling the platelets explicitly. Thanks to this theoretical framework, the mode I fracture energy of DFCs is estimated for the first time and it is shown to depend linearly on the platelet size for the size range investigated in this work. It is found that the fracture energy of DFCs is much larger than several light alloys and always comparable to or larger than the quasi-isotropic laminate composite made from the same constituents. This feature can make DFCs attractive for impact applications [98]. Also, the fracture characteristics of DFCs obtained by this study will be useful for the formulation of certification guidelines for DFCs and the development of their inspection and maintenance strategies.

5.2 Material preparation and test description

5.2.1 Specimen characteristics

Previous studies [33, 35, 37] investigated the intra-laminar size effect on unidirectional and textile composites and successfully obtained the fracture energy. The present work extends the experimental procedure proposed by Salviato *et al.* [37] to account for the peculiar characteristics of the DFCs.

Fracture tests on geometrically-scaled Single Edge Notched Tension (SENT) specimens (see Fig. 5.1) of five different sizes were conducted. The ratio between size-1 (largest) and the

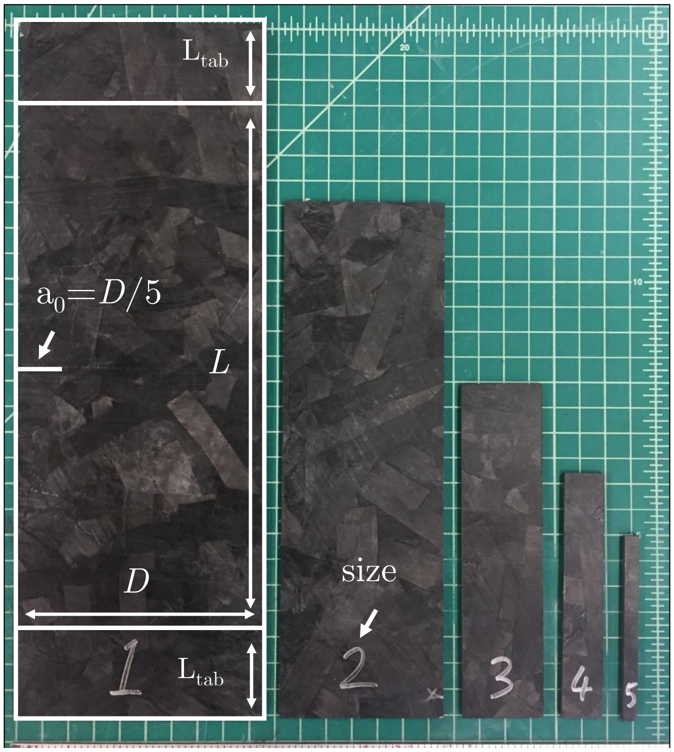

Figure 5.1: Geometrically-scaled, Single Edge Notch Tension specimens investigated in this work.

size-5 (smallest) was 19 : 1. The specimens were geometrically scaled except the thickness which was kept to a constant value of 3.3 mm. Table 5.1 summarizes the geometrical details of the specimens. Five different sizes of coupons were prepared for all three platelets dimensions, 75 × 12, 50 × 8, and 25 × 4 mm. These platelet dimensions were chosen in comparison with the 50 × 8 mm-sized platelets used for commercial aerospace DFC structures [17].

To create a sharp notch, a thin, diamond-coated, razor blade saw was used. The blade thickness was 0.2 mm. The width of the notch was kept in a constant ratio relative to the structure width in this study ($a_0 = D/5$ in Fig. 5.1). A layer of white paint was sprayed followed by the black speckles to use Digital Image Correlation (DIC) technique. It is noteworthy that the displacement fields of the DFC specimens on the front and rear surfaces

Size	Width, D (mm)	Gauge length, L (mm)	Total length, $L + 2L_{tab}^{*}$ (mm)	Notch length, a_0 (mm)	Thickness, t (mm)
1	120	267	343	24	3.3
2	80	178	254	16	3.3
3	40	89	165	8	3.3
4	20	44.5	120.5	4	3.3
5	6.3	14	90	1.3	3.3

* $L_{tab} = 38$ mm

Table 5.1: Geometry of the Single Edge Notch Tension specimens.

could be different because of the inhomogeneous characteristics of the material [99]. However, a single surface DIC result was sufficient to observe the displacement field near the notch and to enable the accurate measurement of the displacement in the gauge area of the specimens and to characterize size-dependent fracture behavior in DFCs.

5.2.2 Testing

A closed-loop, servo-hydraulic Instron 5585H with 200 kN capacity was used for all the tests. The nominal strain rate was set to 0.2 %/min for all the specimen sizes investigated in this work. The load from the machine was recorded with a sampling frequency of 10 Hz. To use the DIC technique, digital images were captured using a Nikon D5600 DSLR camera with Nikon AF micro 200 mm and Sigma 135 mm DG HSM lenses. The images were taken with a sampling rate of 1 Hz.

5.3 Experimental results

5.3.1 Load-displacement curves

The load-displacement curves of the size effect tests were analyzed based on the displacement field computed from DIC using the GOM Correlate software [62]. The nominal displacement was calculated by averaging the relative displacements between two horizontal lines spanning the width of the specimen, placed symmetrically with respect to the crack plane. The distance between the lines was $1.2 \cdot D$ so that it scaled with the specimen size. Thanks to the use of DIC, the effects of the compliance of the machine were removed.

Typical load-displacement curves for the various specimen sizes are shown in Fig. 5.2 for the 25 × 4 mm platelet. As expected, the initial stiffness is similar for all the specimens. However, in agreement with previous results on quasibrittle materials [33–39, 41], a strong size effect can be observed qualitatively by analyzing the structural behavior. That is, for the largest specimen (size-1), the load-displacement curves feature a significantly linear behavior up to the peak load after which sudden failure occurs followed by snap-back instability [100]. This behavior, representing the typical response of a brittle structure, is in sharp contrast with the smaller sizes. In fact, as the specimen size decreases, the structural response becomes nonlinear before the peak due to sub-critical damage in the FPZ. As can be noted from the inset of Fig. 5.2, the smallest specimens (size-5) indeed exhibit a remarkable nonlinear response before the peak, this trend being present for all the different platelet sizes investigated.

5.3.2 Fracture surfaces

In Fig. 5.3, representative fracture surfaces of the tested DFCs are shown. Because of the randomly oriented platelets, mixed damage mechanisms were observed including delaminations between platelets, fiber breakages, pull-outs, and splittings. The fracture paths were also distinct. For size-1, the fracture paths were perpendicular to the loading direction (see Figs. 5.3a-c) whereas the fracture paths became more chaotic and torturous (see Figs. 5.3g-i)

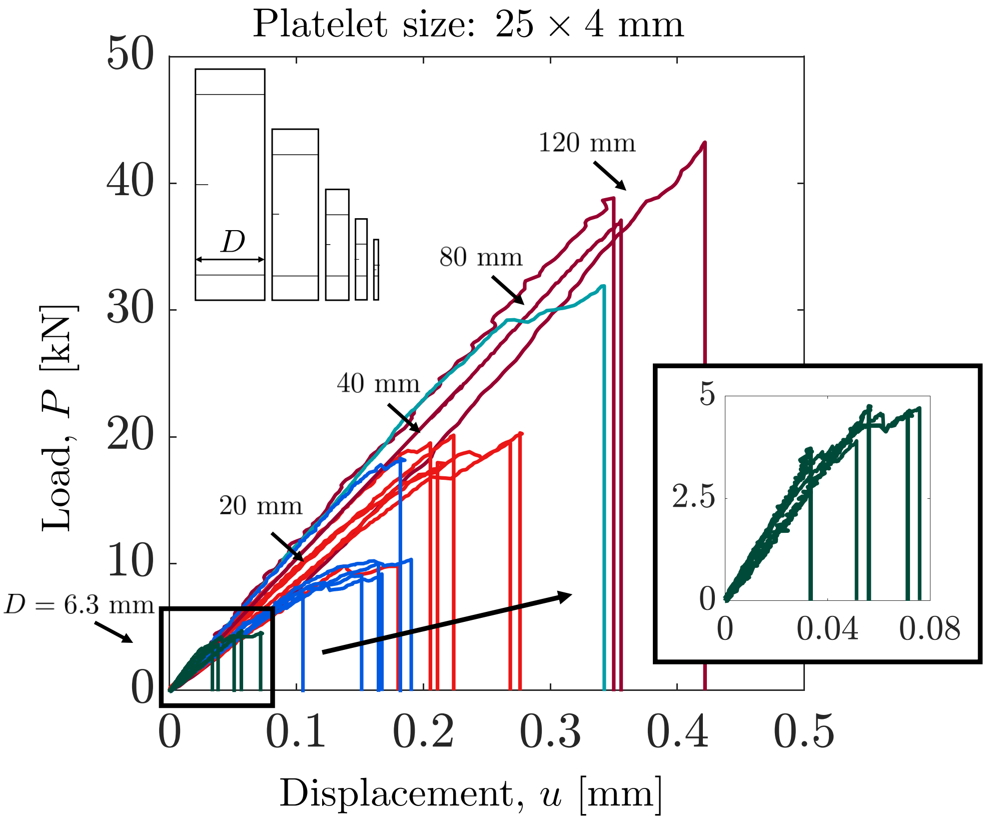

Figure 5.2: Representative load-displacement curves of the DFC specimens with the platelet size of 25 × 4 mm.

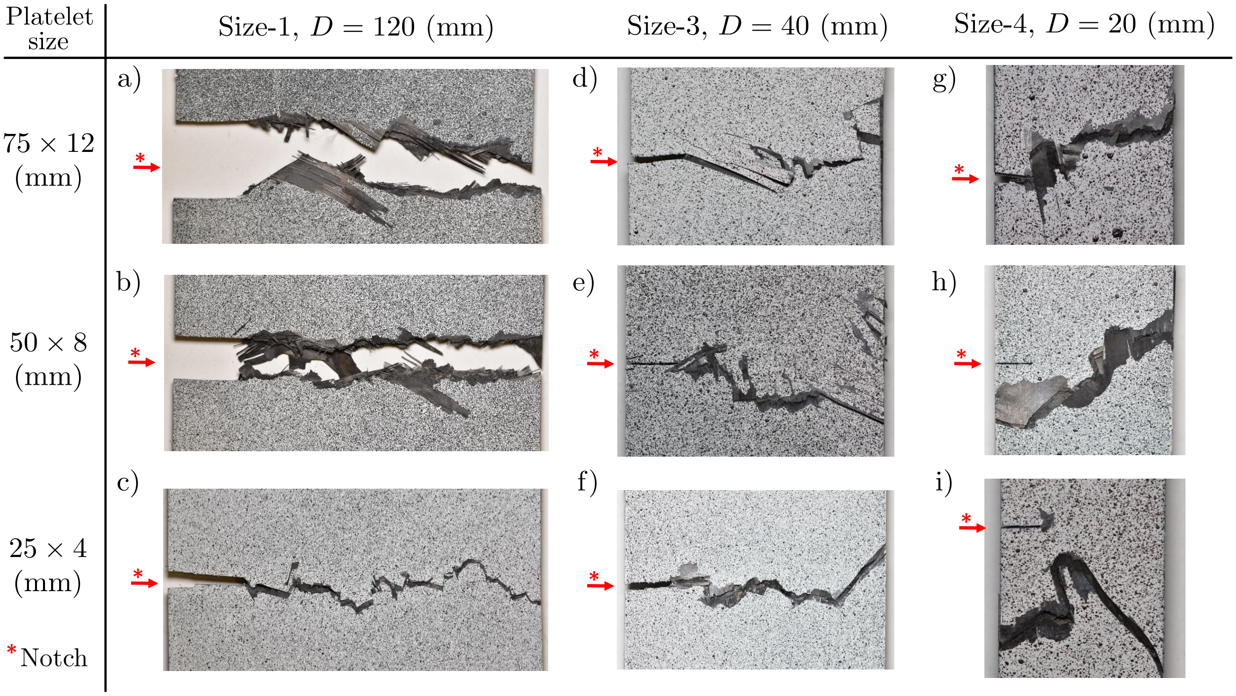

Figure 5.3: Representative fracture surfaces of the Single Edge Notch Tension DFC specimens. The red arrow indicates the initial location of the notch.

as the specimen sizes decreased.

For size-4 and -5, several failures were initiated far from the notch, an indication of pronounced quasi-ductile behavior. Indeed, this phenomenon is related to the distributed damage in the FPZ which promotes stress redistribution in front of the notch. In this context, the fracture process may be triggered by other weak spots in the specimen such as resin rich areas, air pockets, or spots with poorly oriented platelets in which the fiber orientations were mainly towards transverse direction with respect to the loading direction.

In previous studies by Feraboli *et al.* [101] and Qian *et al.* [102], it was claimed that DFC structures can fracture away from a center notch or hole depending on the ratio between the notch and the width of the specimen. However, this statement is only partially true. Indeed, the failure location and fracturing behavior depend strongly on the structure geometry (e.g., ratio between notch size and structure width, the shape of the notch etc). Yet, another important aspect of driving the failure behavior is the structure size relative to the platelet dimensions. This is clearly proven in this work since the specimens were all geometrically-scaled and only the characteristic size of the structure was changed. In the experiments, the failure was triggered away from the notch only for size-3, -4, and -5. In such cases, the failure behavior was pseudo-ductile with significant nonlinear energy dissipation before the peak. For all the other larger specimens, the crack always initiated from the notch and the behavior became increasingly more brittle with increasing dimensions.

5.3.3 Size effect on the structural strength

From the peak load P_c measured during the tests, a nominal strength $\sigma_{Nc} = P_c/tD$ where $t =$ thickness and $D =$ specimen width was calculated. The average nominal strength for various specimens and platelet sizes tested is listed in Table 5.2 and plotted in Figs. 5.4a-c. Figs. 5.4a-c show the experimental strength σ_{Nc} against the size D in double-logarithmic scale. As can be noted, the figures contain two asymptotes. The horizontal asymptote represents the nominal strength as predicted by stress-based failure criterion, whereas the oblique asymptote with a slope of $-1/2$ represents the prediction by LEFM. It can be noted that, regardless of the platelet sizes, the strength of the SENT specimens decreases as the structure size increases. As mentioned before, this size effect cannot be captured by strength-based failure criteria such as Maximum stress, Tsai-Wu, or others since they predict a constant nominal strength for geometrically-scaled structures. The decreasing strength of experimental data in Figs. 5.4a-c certainly deviates from the horizontal asymptote representing the strength-based failure criteria. On the other hand, the trend neither follows LEFM, which predicts a scaling of nominal strength with $D^{-1/2}$. To capture the transition from quasi-ductile fracture (displayed by smaller specimens) to brittle fracture (displayed by larger specimens), a theory equipped with a characteristic length-scale related to the size of the FPZ is needed. Such a theory, based on a combination of equivalent fracture mechanics and stochastic finite element modeling, is presented in the following sections.

	Average failure strength (MPa), Tested number of specimens			
Size	75 × 12 mm	50 × 8 mm	25 × 4 mm	Quasi-isotropic
1	143.2 ± 16.21, 3	139.1 ± 15.68, 2	108.9 ± 9.44, 3	-
2	167.7 ± 27.15, 3	153.8 ± 27.61, 3	129.3 ± 0, 1	176.1 ± 9.73, 3
3	171.1 ± 19.09, 5	198.2 ± 14.90, 5	173.8 ± 11.10, 5	238.6 ± 23.20, 8
4	210.7 ± 12.58, 5	214.2 ± 14.58, 4	160.2 ± 18.87, 5	277.9 ± 31.54, 6
5	230.2 ± 29.13, 4	242.2 ± 4.99, 5	224.2 ± 8.29, 5	-

Table 5.2: The average failure strength and standard deviations of Single Edge Notch Tension specimens (units: MPa) and the number of tested specimens.

5.4 Analysis and Discussion

The goal of the present study is to capture the fracturing behavior and scaling in DFC structures featuring large stress-free notches. At the same time, another objective is to leverage the proposed framework to obtain an estimate of the energy absorbed by the material upon fracture. This latter result is particularly important since, to date, no data are available on this quintessential property.

The approach proposed in the present work stems from equivalent fracture mechanics which was pioneered by Irwin [103] and later extended to quasibrittle media (see e.g., [36] and references therein). The main idea is to account for the effects of the nonlinear damage in the FPZ by adding to the original crack a_0 an additional effective FPZ length, c_f, such that the resultant of the stresses induced by the effective crack equals the one related to the cohesive stresses in the FPZ.

The effective size of the FPZ, c_f, depends significantly on the mechanisms responsible for the dissipation of the elastic energy in the FPZ. In fact, in DFCs the effective FPZ length depends on mechanisms such as fiber fracture, platelet pullout, platelet delamination, and matrix microcracking. These mechanisms are strongly influenced by mesostructural parame-

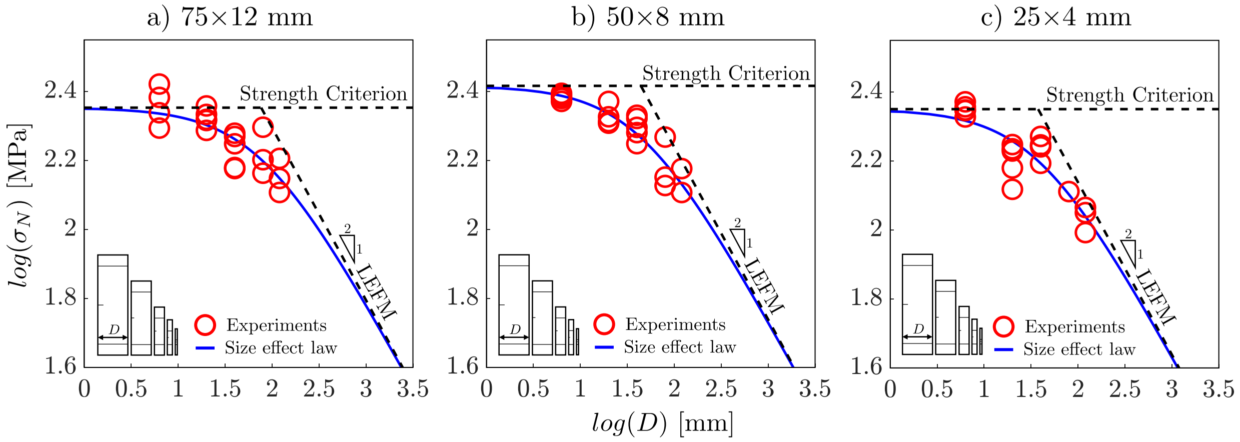

Figure 5.4: Nominal strength against structure size in double-logarithmic scale showing size effect in DFCs with platelet size of a) 75 × 12 mm, b) 50 × 8 mm, and c) 25 × 4 mm.

ters such as the platelet width, the platelet orientation and the number of platelets through the thickness. Accordingly, the mesostructure of DFCs needs to be properly accounted for to describe the fracturing process and capture the effects of the nonlinear FPZ.

In a fully three-dimensional stochastic framework equipped with properly calibrated quasibrittle softening laws the value of c_f could be predicted by explicitly simulating the progressive damage occurring in the FPZ. On the other hand, in equivalent fracture mechanics c_f is a parameter that can be characterized experimentally by means of a size effect analysis. In this scenario, the progressive damage does not need to be modeled explicitly. However, the effects of the mesostructure on the energy release rate in front of the tip must still be captured accurately. Towards this goal, it is quintessential that the random elastic behavior of DFCs is modeled precisely since it accounts for the distribution of elastic strain energy close to the crack tip. Note that the effects of the damage occurring in the FPZ is already accounted for by the equivalent FPZ, which is characterized by the size effect testing.

The following sections aim at providing a description of the analytical and computational framework.

5.4.1 Analysis of fracture tests by Size Effect Law (SEL)

With reference to Fig. 5.1, let a_0 be the initial notch length. To account for the effects of the nonlinear damage in the FPZ, an equivalent crack of length:

$$a = a_0 + c_f \tag{5.1}$$

is considered, c_f being an effective FPZ length treated as a material property.

Following LEFM, the energy release rate $G(\alpha)$ is a function of the crack length as follows:

$$G(\alpha) = \frac{\sigma_N^2 D}{E^*} g(\alpha) \tag{5.2}$$

with $\alpha = a/D$ = dimensionless crack length, σ_N = the nominal stress defined as $\sigma_N = P/(tD)$, and E^* = effective elastic constant. The function $g(\alpha)$ represents the dimensionless energy release rate which relates the geometric and elastic parameters of the structure to G [36,37].

In the condition of incipient fracture, the energy release rate G must be equal to the fracture energy G_f, assumed to be a material property. By substituting Eq. (5.1) in Eq. (5.2), G_f can be expressed in terms of the effective crack length as follows:

$$G_f = G(\alpha_0 + c_f/D) = \frac{\sigma_{Nc}^2 D}{E^*} g(\alpha_0 + c_f/D) \tag{5.3}$$

For homogeneous structures, $g = g(\alpha)$ or, in other words, the dimensionless functions depend only on the geometry of the structure [35,36, e.g]. This means that the dimensionless functions take the same value for all the geometrically-scaled structures investigated in the size effect tests. However, this is not the case for DFCs which are highly inhomogeneous. Indeed, the inhomogeneity size is often comparable to the structure size. In this case, the dimensionless energy release functions g and g' may depend on the structure dimension D relative to platelet size and structure thickness. This is because these functions are related to the amount of strain energy stored in the material that is released by the creation of new crack surface area. This quantity is not only influenced by the structure geometry but also by the morphology of the platelets and their orthotropic elastic properties. Since the platelet size is not scaled with the structure and the number of platelets may not be enough to make the structure statistically homogeneous, a size effect on the energy release occurs.

In view of these considerations, Eq. (5.3) must be rewritten as follows:

$$G_f = \frac{\sigma_{Nc}^2 D}{E^*} g(\alpha_0 + c_f/D, D) \tag{5.4}$$

where now the dimensionless energy release is considered as a function of both the relative crack length and structure size: $g = g\,(\alpha, D)$. Performing a Taylor series expansion around α_0 for a constant structure size D one gets:

$$G_f = \frac{\sigma_{Nc}^2 D}{E^*} \left[g(\alpha_0, D) + \frac{c_f}{D} \frac{\partial g}{\partial \alpha}(\alpha_0, D) \right] \tag{5.5}$$

After rearranging Eq. (5.5), the following equation, known as Bažant's Size Effect Law (SEL) [33, 35, 36] modified for DFC structures is obtained:

$$\sigma_{Nc} = \sqrt{\frac{E^* G_f}{D g(\alpha_0, D) + c_f g'_D(\alpha_0, D)}} \tag{5.6}$$

where $g'_D = [\partial g/\partial \alpha]_D$ and the subscript D indicates partial differentiation with a constant structure size. As can be noted, the main difference compared to the homogeneous case, Eq. (5.3), is that the new equation features an additional size effect related to the dimensionless energy release functions. These functions can be calculated leveraging the stochastic finite element framework presented in the following sections.

Different from LEFM, the foregoing equation relates the nominal strength not only to the fracture energy of the material but also a characteristic length scale c_f, associated to the FPZ size. This length scale is the key to capture the transition of the fracturing behavior from quasi-ductile to brittle with increasing the structure size. Finally, the previous expression can be also written as follows:

$$\sigma_{Nc} = \frac{\sigma_0}{\sqrt{1 + D/D_0}} \tag{5.7}$$

where $\sigma_0 = \sqrt{E^* G_f / c_f g'(\alpha_0, D)}$ and $D_0 = c_f g'(\alpha_0, D)/g(\alpha_0, D)$. σ_0 and D_0 are size effect constants depending on the structure geometry and the size of the FPZ.

It is worth noting that for the structure sizes and the thickness considered in this study, the average dimensionless energy release functions were not found to change significantly with D based on an extensive computational study (detailed discussion in section 5.2). Therefore, for the sake of simplicity, Eq. (5.6) was used with the average value of $g(\alpha_0)$ and $g'(\alpha_0)$ of all the specimen sizes for a given platelet size. However, the reader should keep in mind that for all the cases in which g and g' are shown to depend significantly on the structure dimensions D, Eq. (5.6) with $g(\alpha_0, D)$ and $g'(\alpha_0, D)$ should be used.

Finally, it is worth concluding this section stressing the simplicity of Eq. (5.6). This expression does account for all the key aspects of the fracturing process in DFCs. While the effect of the nonlinear cohesive stresses in the FPZ is accounted for by the introduction of the length scale c_f, the effects of the platelet size and morphology on the energy release are captured by the functions g and g'_D. These functions are calculated by explicitly modeling the platelets by FEA and characterizing the evolution of the strain energy in the structure for different crack lengths.

5.4.2 Fitting of the experimental data using the SEL

To obtain the size effect parameters σ_0 and D_0, regression analysis was conducted on the experimental data. To do so, the following transformation was used:

$$X = D, \;\; Y = \sigma_{Nc}^{-2} \tag{5.8}$$

Using these terms, Eq. (5.6) can be expressed in the following linear form:

$$Y = C + AX \tag{5.9}$$

with:

$$\sigma_0 = C^{-1/2}, \;\; D_0 = \frac{C}{A} = \frac{1}{A(\sigma_0)^2} \tag{5.10}$$

Leveraging this equation, it is possible to perform a linear regression of the size effect data as shown in Figs. 5.5a-c for all the investigated platelet sizes. Then, the size effect parameters,

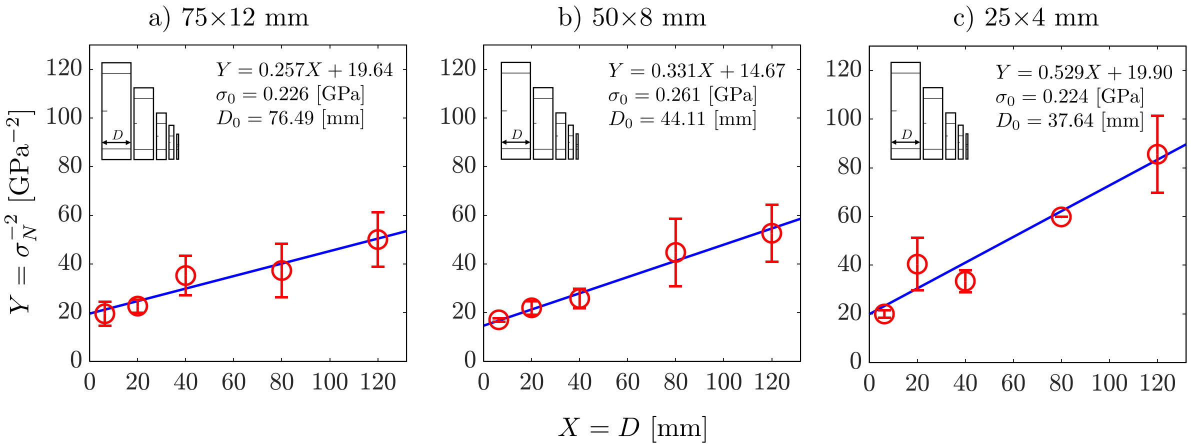

Figure 5.5: Linear regression analysis to find the size effect law parameters, σ_0 and D_0 for the platelet size of a) 75 × 12 mm, b) 50 × 8 mm, and c) 25 × 4 mm.

σ_0 and D_0 are extrapolated from the y-intercept and the slope of the linear regression, by means of Eqs. (5.10).

Figures 5.4a-c show the fitting into SEL based on Eq. (5.6). As can be noted, the results for all the platelet sizes are characterized by a significant deviation from LEFM, the deviation being more pronounced for smaller specimens and larger platelets. In particular, the figures show a transition of the experimental data from stress-driven failure, characterized by the horizontal asymptote, to energy-driven fracture characterized by the $-1/2$ asymptote. This phenomenon can be ascribed to the increased size of the FPZ compared to the structure size, which makes the non-linear effects caused by micro-damage in front of the crack tip not negligible. For sufficiently small specimens, the FPZ affects the structural behavior and causes a significant deviation from the scaling effect predicted by LEFM. Indeed, the structural strength is less affected by the size. On the other hand, for increasing sizes, the effects of the FPZ become less significant, thus leading to a stronger size effect closely captured by LEFM. Further, comparing the size effect plots of DFCs from small to large platelet sizes, a gradual shift of experimental data points can be noted towards the quasi-ductile region. Thus, it shows that not only the larger platelets lead to a higher fracture toughness but also to a gradually more quasi-ductile structural behavior for a given size.

The foregoing conclusions are extremely important for the design of DFC structures featuring defects or sharp notches. The pseudo-ductile behavior reported in fracture tests on small laboratory-scaled DFC specimens may induce designers to overestimate severely the load capacity of real, large structural components if strength-criteria is used. On the other hand, LEFM does not always provide an accurate method to extrapolate the structural strength of larger structures from lab tests on small-scale specimens, especially if the size of the specimens belongs to the transitional zone. In fact, the use of LEFM in such cases may lead to a significant underestimation of structural strength, thus hindering the full exploitation of DFC fracture properties. This is a severe limitation in several engineering applications such as aeronautics and astronautics for which structural performance optimization is of utmost importance. On the other hand, LEFM always overestimates significantly the strength when used to predict the structural performance at smaller length-scales. This is a serious issue for the design of e.g. small complex-shaped components. In such cases, SEL or other equivalent material models with a characteristic length scale ought to be used.

It is interesting to compare the structural behavior of DFCs to traditional continuous composite structures. To do so, quasi-isotropic (QI) laminates $[0/45/90/-45]_{3s}$ with geometrically-scaled SENT specimens were manufactured with the identical prepreg system. The average thickness of the QI laminates were 3.43 mm. The test method was identical with the DFCs. The resulting strengths are listed in Table 5.2. Using the Eq. (5.6), the size effect curve of the QI laminate is plotted in Fig. 5.6a. The QI possesses far more brittle behaviors compared to the DFCs reaching oblique asymptote even with the smallest specimen size. Because of the higher sensitiveness to the stress risers in the QI laminate, the strength drops much quickly as the structure size increases. Surprisingly, the QI provides lower strength after reaching the structure size of 112 mm comparing with the DFCs made of largest platelet size (see the crossing of the two curves marked with a star in Fig. 5.6b). This result indicates that DFCs are more suitable than QI laminates for the structures with sufficiently large size containing the geometrical stress risers such as notches or holes.

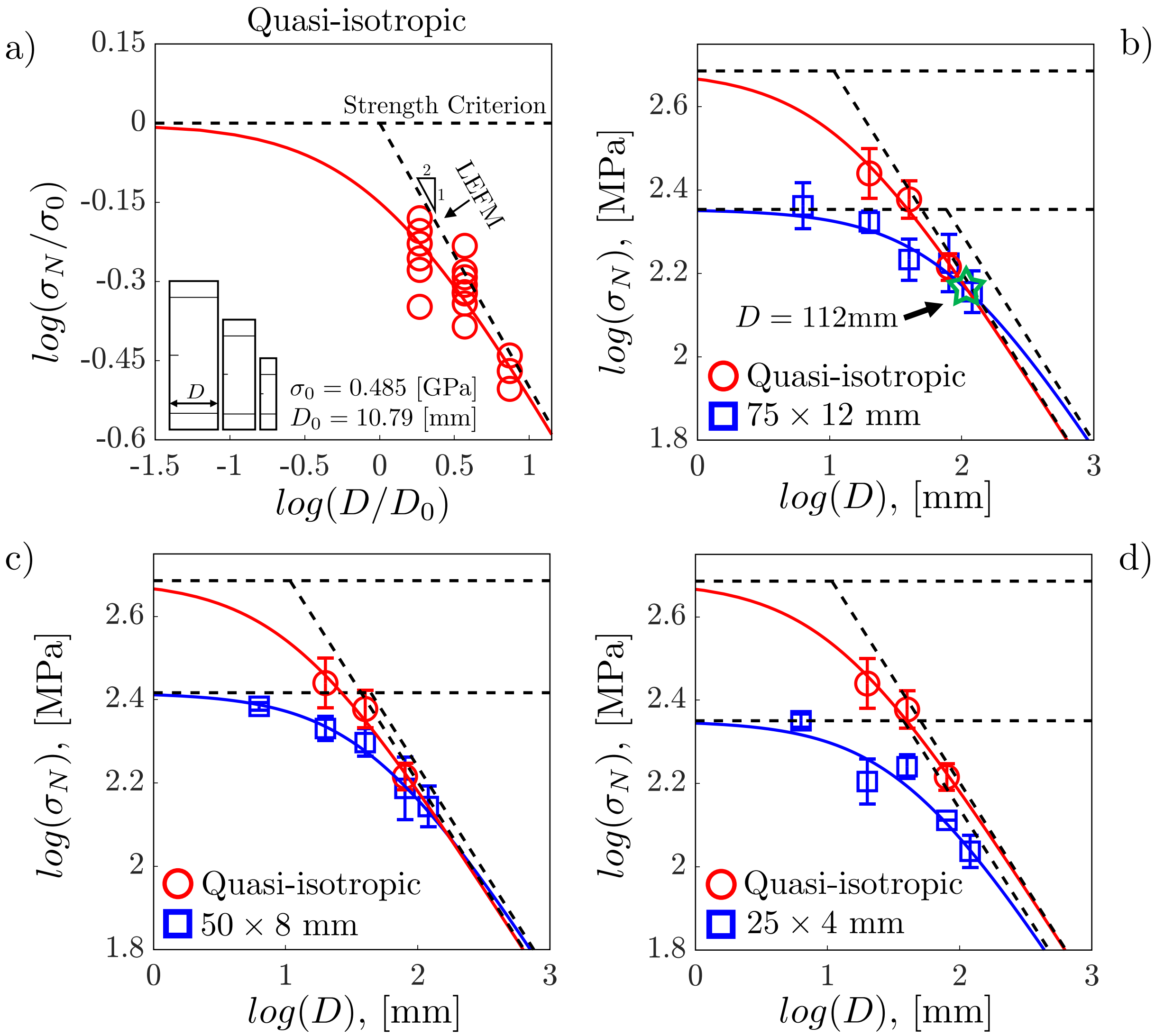

Figure 5.6: a) Normalized size effect curve of quasi-isotropic (QI) laminate, a star mark shows where the two solid lines cross over, b) size effect curve of QI with 75 × 15 mm, c) QI with 50 × 8 mm, and d) QI with 25 × 4 mm.

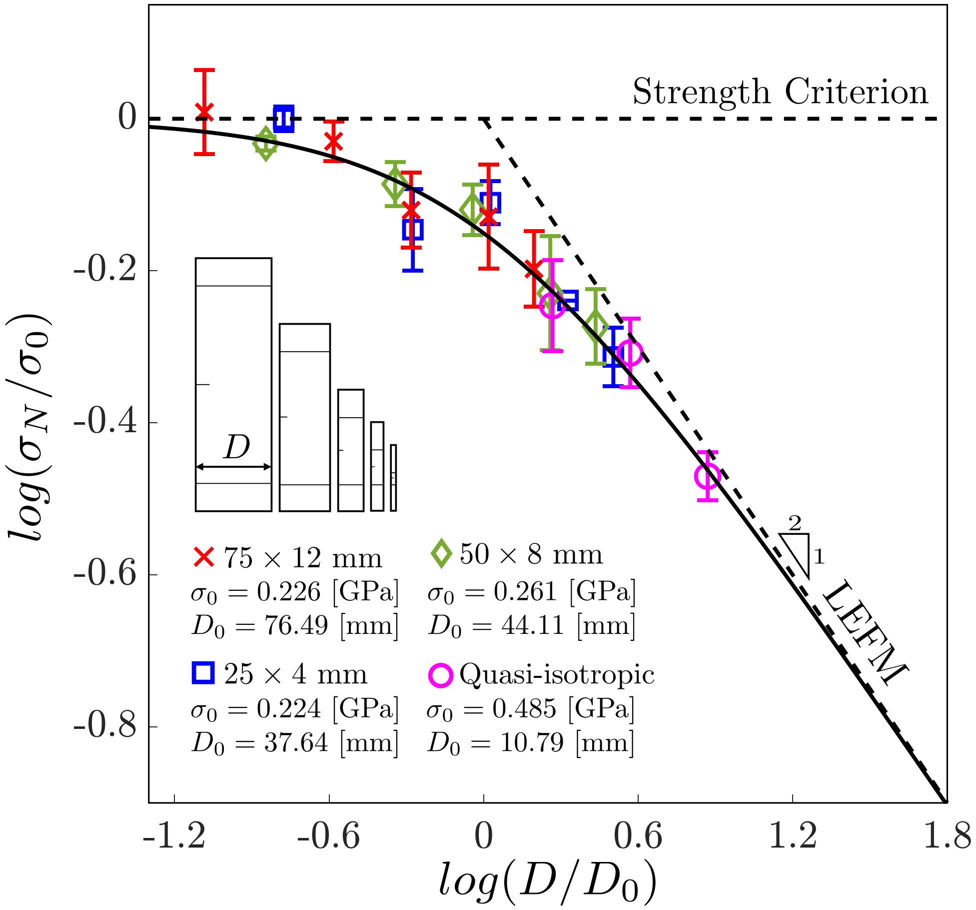

Figure 5.7: Normalized size effect curves in double-logarithmic scale showing a size effect in the DFCs with all the platelet sizes and the quasi-isotropic laminate.

Figure 5.7 combines all the normalized experimental strength, σ_{Nc}/σ_0, against the normalized size, D/D_0, in double-logarithmic scale with the SEL fitting. Regardless of the platelet sizes, all the normalized strengths are well captured by the SEL. Also, the structure sizes tested in the laboratory are within the neighbor of D_0, where the two asymptotes meet. This D_0 is called the *transitional size* where it locates the transition from quasi-ductile to brittle behavior. This trend confirms that DFCs are the quasibrittle material containing the non-negligible size of the FPZ.

5.4.3 Brittleness number of DFCs vs traditional laminated composites

For additional structural behavior comparison between the traditional composite structures with DFCs, a useful non-dimensional parameter called the *brittleness number*, β, is introduced [36]. This parameter, comparing the brittleness of structures with similar geometry and size, is defined as the ratio between the structure characteristic size, D, and the transition size, D_0. When β is greater than ~ 10, the behavior of the structure is typically very brittle and LEFM is well suitable to capture the fracturing behavior of the material. When β is less than 0.1, the structure can be considered as quasi-ductile or perfectly plastic. The stress-based failure criteria provides a fairly good prediction of the structural strength. If β lies in between 10 and 0.1, the structure should be treated as quasibrittle material. Figure 5.8 shows β for the DFC structures investigated in this work compared to a QI laminate. Further, the β for the textile composite structures tested in [37] is also provided for reference. As can be noted, the brittleness number of DFCs is always within the boundary of the quasibrittle zone for all the structure sizes investigated, regardless of the platelet size. In contrast, both the QI and textile composite feature higher brittleness numbers for the same structure size, with the largest specimen reaching the LEFM region. From the foregoing analysis, it is evident that DFCs are, by far, less brittle than traditional composites. This is a highly desirable condition for the design of damage tolerant composite structures featuring notches and other stress raisers.

5.5 Stochastic finite element model

One of the main objectives of this study is to estimate, for the first time, the mode I intralaminar fracture energy G_f of DFCs. To characterize G_f leveraging Eq. (5.6), the dimensionless functions $g(\alpha_0)$ and $g'(\alpha_0)$ need to be calculated. These functions are related to the release of elastic strain energy induced by the crack, which is significantly influenced by the platelet constitutive properties and, more importantly, the random platelet distribution. To capture these aspects, a stochastic finite element model is used.

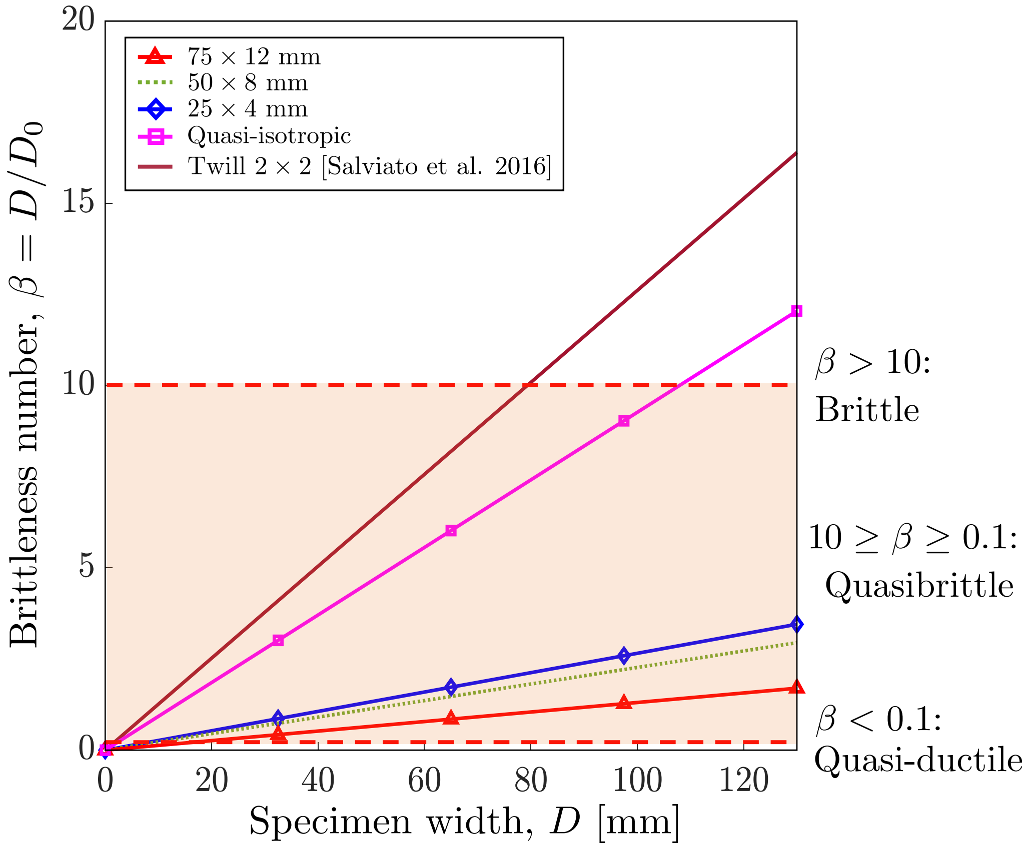

Figure 5.8: Brittleness number, β, vs structure size for the DFCs investigated in this work, a quasi-isotropic laminated composite made using the same prepregs, and a carbon twill 2×2 composite [37].

5.5.1 *Computation of $g(\alpha)$ and $g'(\alpha)$ and the fracture energy*

The mesostructure generated by the algorithm described in section 4.2.1 was imported in Abaqus/Standard [73]. 8-node, quadrilateral Belytschko-Tsay shell elements (S8R) were used to model the structure and to calculate the reaction force, P, and the total strain energy. The behaviors of the platelets and resin layers were assumed to be linearly elastic, with the elastic properties given in Table 5.3.

Description	T700G	Resin
Platelet thickness, t (mm)	0.135	varies
In-plane longitudinal modulus, E_1 (GPa)	135	3
In-plane transverse modulus, E_2 (GPa)	10	3
In-plane shear modulus, G_{12} (GPa)	5	1.1
In-plane Poisson ratio, ν_{12}, ν_{31}	0.3	0.35

Table 5.3: Elastic properties of the platelet (T700G) and resin layer used in this study.

A uni-axial uniform displacement was applied at one end of the specimen while the other end was fixed in all directions. To find the dimensionless functions $g(\alpha)$ and $g'(\alpha)$ using Eq. (5.2), the energy release rate $G(\alpha)$ needed to be computed using the finite element method.

Generally, a convenient method to obtain the energy release rate is using the J-integral approach [37, 104]. However, this is not applicable to DFCs due to their in-homogeneous material characteristics. Accordingly, to calculate $G(\alpha)$, its definition is used directly [36]:

$$G(u, a) = -\frac{1}{b}\left[\frac{\partial \Pi(u, a)}{\partial a}\right]_u \tag{5.11}$$

with u being the equilibrium displacement, a being the crack length, b the thickness, and Π being the potential energy of the whole specimen. Figure 5.9a shows the potential energy

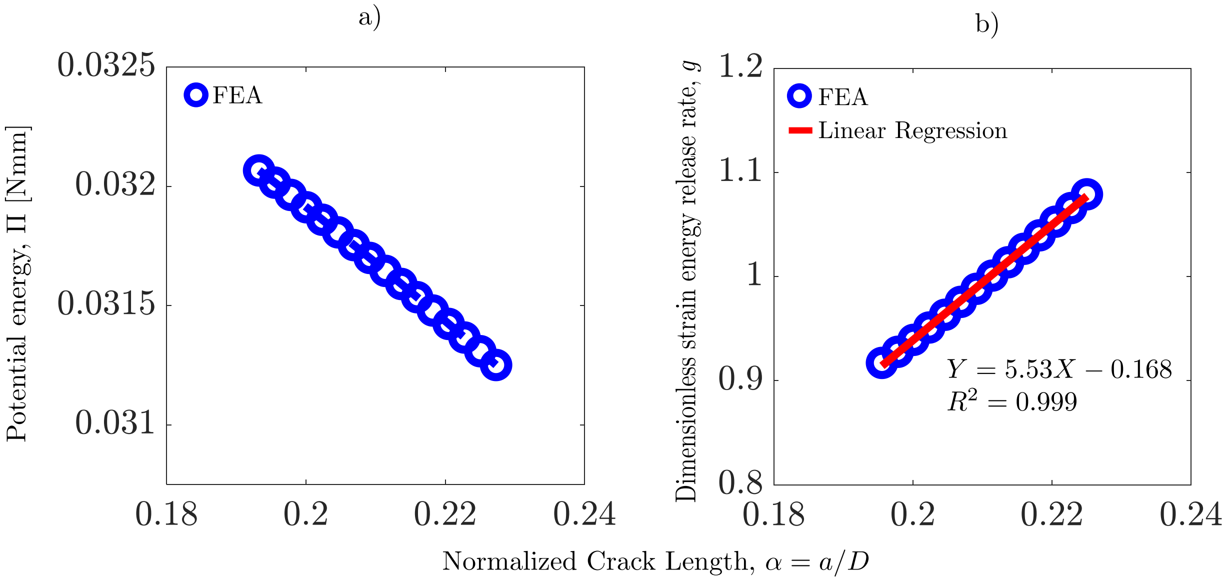

Figure 5.9: a) Obtained potential energy of a typical SENT DFC specimen, b) The calculation of dimensionless energy release rate $g(\alpha_0)$ and its derivative $g'(\alpha_0)$.

of a typical DFC SENT specimen. Then, $G(u,a)$ is calculated by means of a central finite difference approximation, $G\left(u,a\right) \approx -1/b\left[\Delta\Pi\left(u,a\right)/\Delta a\right]_u$, as a function of the normalized crack length, $\alpha = a/D$. Once the energy release is calculated, $g(\alpha)$ can be calculated taking advantage of Eq. (5.2), whereas $g'(\alpha)$ can be calculated by linear interpolation for $\alpha \to \alpha_0$ (see Fig. 5.9b).

For homogeneous, geometrically-scaled specimens, the functions $g(\alpha)$ and $g'(\alpha)$ do not depend on the structure size [36]. However, in the case of DFCs, this is not generally true as explained in the previous sections. For this reason, 10 different mesostructures of the size-2, -3, and -4 were simulated to verify if any size effect on the dimensionless energy release functions was present for the structures investigated in this work. The results of this computational study are presented in Fig. 5.10 which provides $g(\alpha)$ and $g'(\alpha)$ with $\alpha = \alpha_0$ as a function of the specimen size for the various platelet dimensions. As can be noted, for a moderate window of the specimen and platelet size variations considered in this work, the

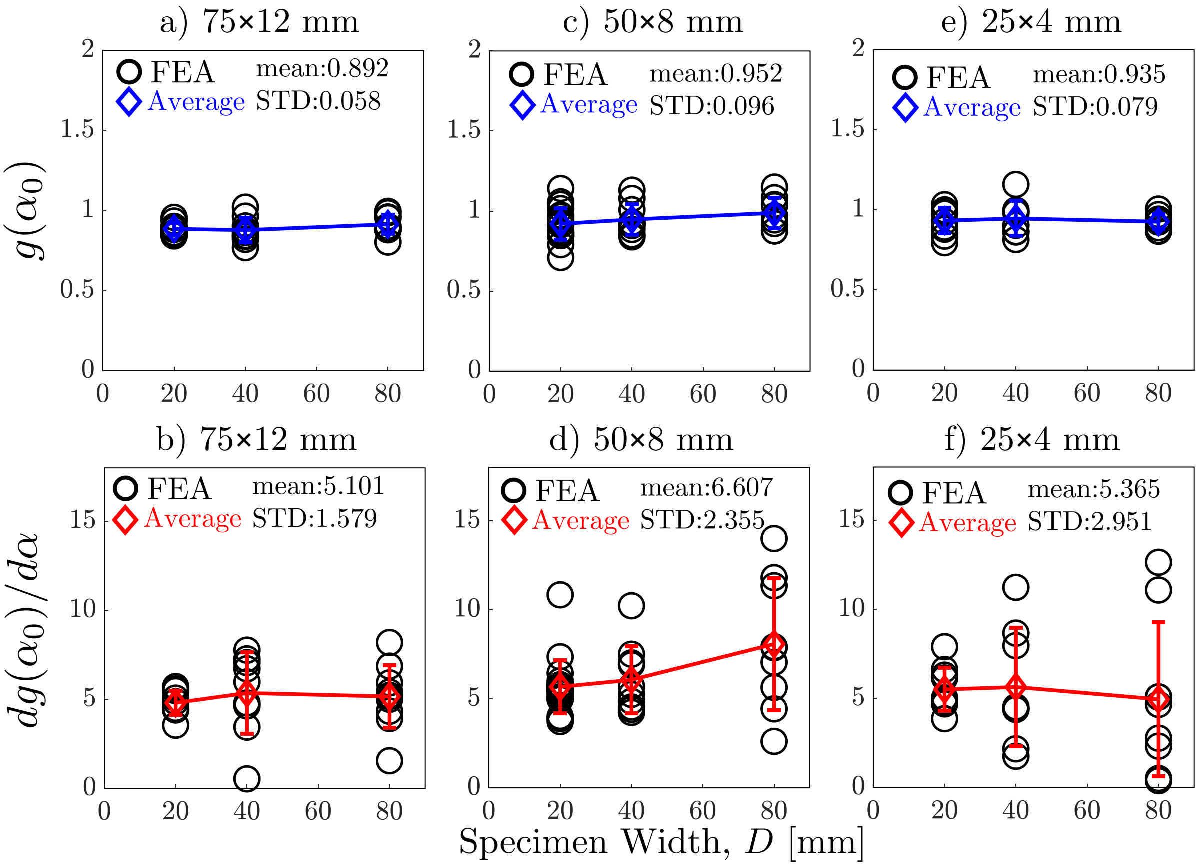

Figure 5.10: Comparison of dimensionless energy release rate and its derivative for the platelet size of a) and b) 75 × 12 mm, c) and d) 50 × 8 mm, and e) and f) 25 × 4 mm.

structural size effect on the average value of these functions is not significant. A slight effect of the size on the CoV of the function g' is noticeable but was neglected in this work as it does not affect the average behavior. Based on these results, the average values of the dimensionless functions were used. These values are summarized in Table 5.4 along with the ones for a quasi-isotropic laminate with equal thickness. Though the variations of $g(\alpha, D)$ and $g'(\alpha, D)$ are minute in this study, the case of their large variations will be reported in the future publications.

Connecting the size effect parameters, A and C, with the dimensionless functions lever-

Platelet size (mm)	$g(\alpha_0)^*$	$g'(\alpha_0)^*$	Fracture energy, G_f (N/mm)	Effective FPZ length, c_f (mm)
75 × 12	0.892 ± 0.058	5.101 ± 1.579	65.47 ± 11.38	13.21 ± 0.89
50 × 8	0.852 ± 0.096	6.607 ± 2.355	55.05 ± 13.23	6.41 ± 0.49
25 × 4	0.935 ± 0.079	5.365 ± 2.951	33.66 ± 9.34	6.54 ± 0.57
Quasi-isotropic	0.84	4.92	41.01 ± 11.28	1.85 ± 0.31

* Results of the FEM simulations

Table 5.4: The fracture properties obtained by the size effect experiments and the stochastic finite element.

aging Eq. (5.6), the fracture energy, G_f, and the effective FPZ length, c_f, can be calculated:

$$G_f = \frac{g(\alpha_0)}{E^*A}, \quad c_f = \frac{E^*G_fC}{g'(\alpha_0)} \tag{5.12}$$

Table 5.4 lists the fracture parameters for all the platelet sizes. The standard deviations are calculated following the approach in [36]. To provide better comparison, the fracture energy of three different platelet sizes is plotted in Fig. 5.11 along with the one of a typical Al5083 [105] and of a T700G QI laminate composite. The G_f of the QI laminate was obtained experimentally following the identical test procedure.

As can be noted from the Fig. 5.11, the complex heterogeneous mesostructure of DFCs provides them with the outstanding fracture energy. The fracture energy calculated in this work is 65.47 N/mm, 55.05 N/mm, and 33.66 N/mm for the 75 × 12, 50 × 8, and 25 × 4 mm platelets respectively. These fracture energies are from 5.5 to 2.8 times larger than the one of a typical Al5083 ($\sim$ 12 N/mm). This is remarkable considering that aluminum is one of the main competing materials for the manufacturing of complex, lightweight aerospace/automobile components. It is also a promising result in view of the possible application of DFCs to improve the crashworthiness of lightweight structures. It is noteworthy that all the DFCs considered in this study exhibit the fracture energy that is comparable or even larger than

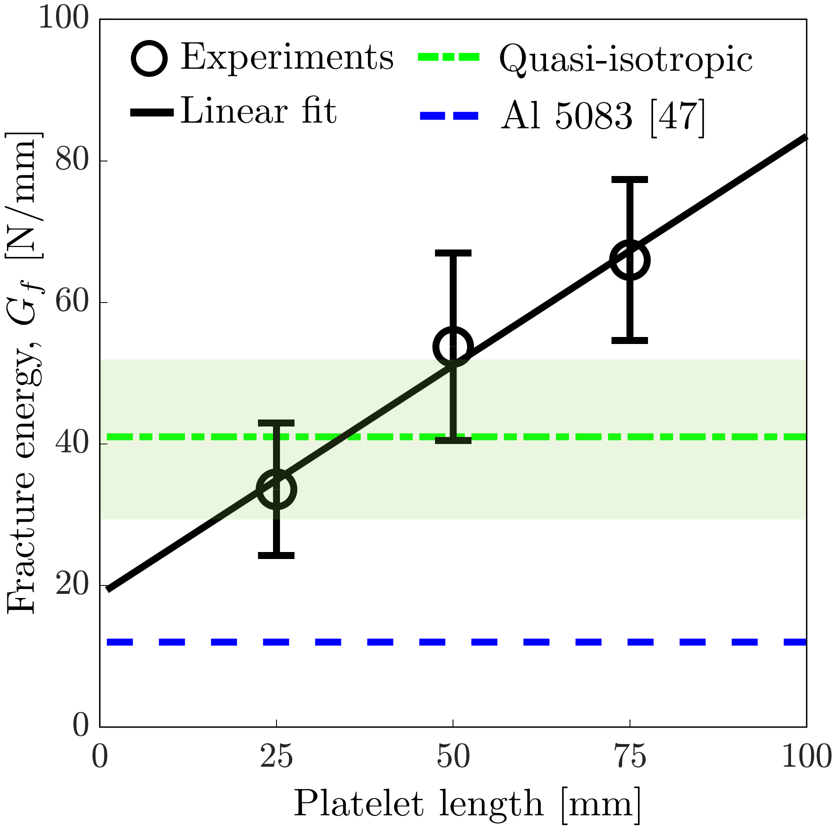

Figure 5.11: Comparison of the mode I fracture energy for DFCs, a quasi-isotropic layup, and a typical aluminum alloy.

the QI laminate made from the same materials (= 41.01 N/mm). For the DFCs made by 75 × 12 mm platelets, the fracture energy is 1.60 times larger.

The results also clearly indicate a strong effect of the platelet size on the fracture properties of the material. In particular, the fracture energy increases linearly with the platelet size in the range investigated in this work. Further computational studies are ongoing to clarify how this trend is affected by the mechanical properties of the constituents and the random orientation of the platelets. Finally, it is worth mentioning here that the platelet size also affects the effective FPZ length which is found to be 13.21, 6.41, and 6.54 mm for the 75×12, 50×8, and 25×4 mm platelets respectively. This is in agreement with the more pronounced quasi-ductility reported for the DFC structures made of longer platelets.

5.5.2 Remarks on the stochastic FE simulations

In the calculation of the dimensionless energy release rate functions presented in the foregoing sections it is worth to stress that the goal of the stochastic FEM simulation is not to model the progressive inter- and intra-platelet damage in DFCs. Rather, the objective is to properly calculate the energy release rate functions required for the proper application of the equivalent fracture mechanics approach proposed in this work. In pursuit of this goal, only the elastic strain energy in the structure needs to be simulated accurately. As the excellent agreement between energetic size effect law and the experimental data show, this is more than enough to simulate structures featuring long stress-free notches, the subject of this study. At the same time, the framework enabled the estimation of the fracture energy and the size of the FPZ for the first time for DFCs. It is worth mentioning, however, that in cases in which the structure exhibits pristine “defects’ due to the random heterogeneous mesostructure that are more severe than the applied notch, the statistical behavior of DFCs and their progressive damage significantly affects the mechanics of the structure and needs to be accounted for.

A full three-dimensional stochastic FE model to capture these important aspects is under development by the authors. Preliminary results have shown that modeling the random distribution of the platelets explicitly and capturing the damage with proper quasi-brittle damage laws leads to an accurate prediction of the failure location and the structural behavior. The discussion of such a modeling framework is beyond the scope of the present manuscript and will be the subject of future publications.

5.6 Conclusion

This work investigated the fracturing behavior and scaling of Discontinuous Fiber Composite (DFC) structures leveraging a combination of experiments and stochastic computational modeling. Based on the results of this study, the following conclusions can be elaborated:

1. The fracture tests on geometrically-scaled Single Edge Notch Tension (SENT) specimens confirmed a remarkable size effect on the structural strength. It was found that, when the specimen is sufficiently large, the structural strength scales according to the Linear Elastic Fracture Mechanics (LEFM) and the failure occurs in a very brittle way. In contrast, small specimens exhibit a more pronounced pseudo-ductility with limited scaling effect and a significant deviation from LEFM.

2. The transition from quasi-ductile to brittle fracture with an increasing specimen size is related to the development of a significant Fracture Process Zone (FPZ) whose dimensions were found to be comparable to the platelet size. In the FPZ, significant non-linear deformations due to sub-critical damage mechanisms, such as platelet delamination, matrix microcracking, and platelet splitting/fracture, promote strain redistribution and mitigate the intensity of the stress field induced by the crack/notch. This phenomenon is more pronounced for small structures since the size of a fully-developed FPZ is typically a material property and thus its influence on the structural behavior becomes increasingly significant as the structure size is reduced. For sufficiently large structures, the size of the FPZ becomes negligible compared to the structure's characteristic size in agreement with the inherent assumption of the LEFM that non-linear effects are negligible during the fracturing process.

3. The design of DFC structures must take the foregoing size effect on the nominal strength into serious consideration. In fact, if the correct scaling is not understood and properly acknowledged, the pseudo-ductile behavior reported in fracture tests on small laboratory-scaled DFC specimens may induce designers to overestimate severely the load capacity of real, large structural components. Size effect testing and analysis can overcome this problem.

4. To characterize the fracture energy, G_f, and the effective length of the fracture process zone, c_f, an approach combining equivalent fracture mechanics and stochastic finite element modeling was proposed. The model accounts for the effects of the complex random mesostructure of the material by modeling the platelets explicitly. This theoretical framework was able to describe the scaling of structural strength and enabled the characterization of the mode I fracture energy of DFCs.

5. G_f and c_f were estimated for a platelet size of 75×12 mm, 50×8 mm, and 25×4 mm respectively. It was found that $G_f = 65.47$ N/mm, 55.05 N/mm, and 33.66 N/mm while $c_f = 13.21$ mm, 6.41 mm, and 6.54 mm. These results clearly indicate a strong effect of the platelet size on the fracture properties of the material. In particular, the fracture energy was found to increase linearly with the platelet size in the range investigated in this work. Further computational studies are ongoing to clarify how this trend is affected by the mechanical properties of the constituents and the random orientation of the platelets.

6. While the fracture energy increases with the platelet size, the manufacturability indexes [106] developed for DFCs follow an opposite trend. Accordingly, particular care should be devoted to identifying the platelet morphology providing the best compromise in terms of manufacturabilty and fracture toughness for the desired application.

7. The analysis of the fracture tests highlighted an outstanding fracture energy of DFCs, from 2.80 to 5.50 times larger than the one of a typical Al5083 for the platelet sizes

investigated in this work. This result is particularly interesting in view of possible use of DFCs for crashworthiness applications.

8. Another important conclusion of this work is that, compared to traditional unidirectional composites, DFC structures exhibit higher pseudo-ductility and their strength is, by far, less sensitive to notches, defects, and cracks. However, this aspect can be used advantageously in structural design only upon the condition that proper certification guidelines acknowledging the more pronounced quasibrittleness of DFCs are formulated. The size effect analysis presented in this work represents the first step in this direction as it allows the assessment of the severity of a defect or notch for any DFC structure size and geometry.

9. Future work will focus on the development of a full three-dimensional stochastic FE model to capture the stochastic progressive damage in DFCs. Preliminary results have shown that modeling the random distribution of the platelets explicitly and capturing the damage with proper quasi-brittle damage laws leads to an accurate prediction of the failure location and the structural behavior. This aspect is of utmost importance to capture the failure of structures in which the failure is substantiated by the presence of weak spots due to the random mesostructure rather than by stress-free notches.

Chapter 6

EFFECT OF THE THICKNESS ON THE FRACTURING BEHAVIOR OF DISCONTINUOUS FIBER COMPOSITE STRUCTURES

6.1 Introduction

Discontinuous Fiber Composites (DFCs) made of chopped fiber platelets offer unique advantages over traditional unidirectional composites. The possibility of manufacturing DFC components by compression molding thanks to the outstanding formability, makes DFCs a highly viable option even for very complex geometries [93–95]. These characteristics have attracted significant interest from the scientific and industrial communities for the use of DFCs in applications that have been typical of light alloys, such as secondary structural components for aerospace [17, 93, 95], body frames of terrestrial vehicles [17, 91, 92, 94], composite brackets, suspension arms and interiors [94] and crash absorbers [17, 91, 94].

Another interesting feature of DFCs is their mechanical behavior compared to more traditional composites. Recent studies have shown that DFCs tend to exhibit a more quasi-ductile behavior [9, 13, 22, 50, 89, 90] and a significantly lower notch sensitivity [29, 31, 32] compared to laminated composites. At the same time, the fracture energy dissipated by DFCs has been shown to be noticeably larger than aluminum alloys and typical quasi-isotropic laminates, the main competing materials in the aerospace industry [29].

The foregoing interesting mechanical properties, however, have been shown to be significantly dependent on the material mesostructure and the structure size and geometry. In [22], Feraboli *et al.* conducted an extensive experimental campaign which showed that, for the range of plate thickness and platelet sizes investigated, the tensile and compressive strength increase with the platelet length whereas the effective elastic moduli seem to be almost unaffected. Combining experiments and two-dimensional Finite Element modeling, Selezneva *et al.* [9, 67] found that the measured strengths and their Coefficient of Variation (CoV) are strongly related to the platelet size and the thickness of the plates. The longer platelets provide higher strength with increased CoV whereas the thicker plates increase the average strength and feature a lower variability. Similar tests were conducted by Wan and Takahashi [13] who investigated the effects of the molding pressure. They concluded that a higher molding pressure increases the strength in both tension and compression whereas no significant differences were found on the effective elastic moduli. Nilakantan and Nutt [107] further extended the study on the effects of the processing conditions on the mechanical properties of DFCs. They investigated different manufacturing methods such as open, closed mold, and vacuum-bag-only. They found that the manufacturing conditions affect the mechanical performance of DFCs in a substantially different manner compared to continuous fiber composites. For instance, they found that DFCs show little correlation between the void contents and the tensile strength. Leveraging a three-dimensional mesoscale model and experimental tests, Kravchenko *et al.* [24, 97] investigated notch-free DFC structures with aligned and staggered platelets. Using controlled platelets orientations, they found that DFCs with longer and thinner platelets have higher strengths. They also showed that the mechanisms of failure transition from delamination-dominated fracture to platelet failure as its length increases. This phenomenon, similar to the one reported in other staggered materials systems such as nacre [108–111], causes the strength to increase almost linearly with the platelet size until reaching an asymptotic value. This asymptotic value depends on the strength of the platelet and its morphology and the mechanical properties of the polymer matrix.

Additionally, the effect of the tow thicknesses on the strength of DFCs was studied experimentally and numerically. Li *et al.* [12] investigated two different tow thicknesses under the uniaxial tension. Meng *et al.* [112] studied three different tape thicknesses in double-shear tests. Kravchenko *et al.* [24] as mentioned previously, examined the effect of the tow thickness in aligned and staggered platelets numerically. For all three cases, the strength of DFCs improved as the tow thickness decreased. Although many researchers investigated the behaviors of DFCs, there were two fundamental missing aspects regarding the study of DFCs. The first aspect was detailed study of the fracturing behaviors and its scaling. The second aspect was the effect of the structure thickness.

Ko *et al.* [29] investigated the fracturing and scaling of DFCs with respect to the platelet morphology. They showed that not only the platelet morphology but also the structure size and geometry affect the fracturing behavior. Through size effect test campaign on geometrically-scaled Single Edge Notch Tension (SENT) specimens made with platelets of different sizes, they were able to show that the fracturing behavior changes from pseudo-ductile to brittle with increasing specimen sizes. They also proposed a framework combining equivalent fracture mechanics and stochastic finite elements to estimate the fracture energy of the material. They found that this energy increases almost linearly with increasing platelet sizes. However, the effect of the thickness of the structure on the overall fracturing behavior and its scaling was still missing.

In order to shed more light on this critical aspect, this study presents an investigation of the intra-laminar fracture and the size effect in DFCs for four distinct structure thicknesses. The size effect on the structural strength of geometrically-scaled SENT specimens is characterized for each thickness. To capture the size effect and characterize the fracture energy, G_f, and the effective length of the fracture process zone, c_f, for each thickness, the approach combining equivalent fracture mechanics and stochastic finite element modeling proposed by Ko *et al.* [29] is used in this study. The model accounts for the complex random mesostructure of the material by modeling the platelets explicitly. Thanks to this theoretical framework, the mode I fracture energy of DFCs is estimated and it is shown to depend linearly on the thickness until it reaches an asymptotic value of 57.77 N/mm. For all the thicknesses investigated in this work, the fracture energy was much larger than aluminum alloy and quasi-isotropic laminate composites made from the same constituents. This aspect is significantly interesting considering the possible use of DFCs in applications demanding crashworthiness (see e.g. [98]).

6.2 *Material preparation and test description*

6.2.1 Material preparation

In previous studies, size effect testing of geometrically-scaled SENT specimens led to an accurate measure of mode I intra-laminar fracture properties of unidirectional laminates, textiles, and DFCs [29, 35, 37, 113, 114]. Therefore, in this study, we followed the experimental procedures proposed by Ko *et al.* [29]. As a first step, we manufactured the specimens using a Toray T700G-12K prepreg system and leveraging the in-house manufacturing process reported in [32]. We control the weight of the plate to manufacture consistent plate thickness.

To investigate the effect of the thickness, four different plate thicknesses were investigated: 4.1, 3.3, 2.2, and 1.1 mm. These values are chosen considering typical applications of DFCs. For each thickness, four different geometrically-scaled specimen sizes were investigated with all the dimensions being scaled (Fig. 6.1), while keeping the platelet size constant (50 × 8 mm). As summarized in Table 6.1, the ratio between the largest (size-1) and the smallest (size-4) specimen was 12.3 to 1, a ratio considered to be sufficiently large to enable a thorough investigation of the size effect on the nominal strength.

Table 6.1: Geometry information of the Single Edge Notch Tension (SENT) specimens.

Size	Width, D (mm)	Gauge length, L (mm)	Total length, L (mm)	Notch length, a_0 (mm)
1	80	178	254	16
2	40	89	165	8
3	20	44.5	120.5	4
4	6.5	14.5	90.5	1.3

* Tested thicknesses are 4.1, 3.3, 2.2, 1.1 mm with the platelet size of 50 × 8 mm.

To create a notch, a diamond-coated razor saw of width 0.2 mm was used. We choose to

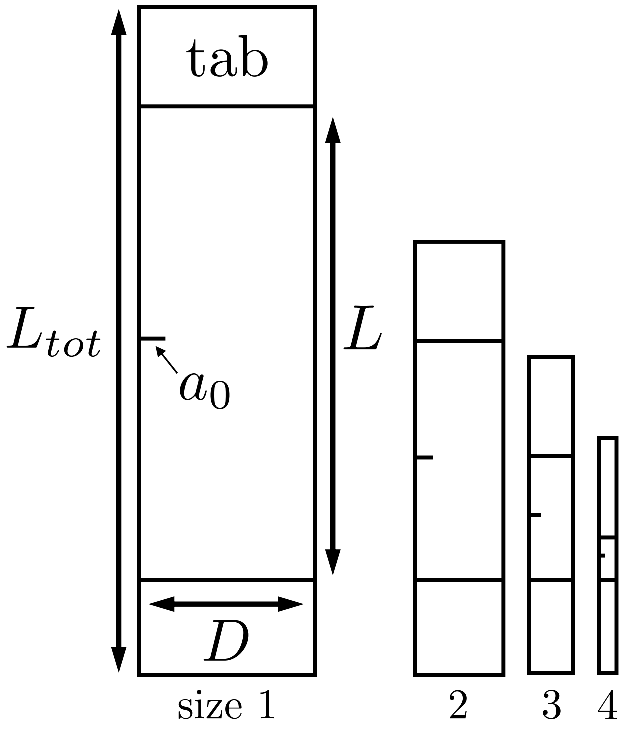

Figure 6.1: Geometry details of the Single Edge Notch Tension specimens.

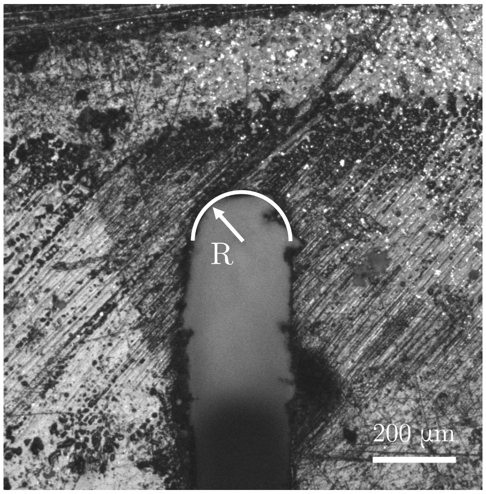

Figure 6.2: Optical microscope image of a typical notch tip used in this work. The tip radius is R = 0.23 mm which is negligible compared to the size of the Fracture Process Zone (FPZ) of the material system investigated.

saw the specimens because it prevents the development of the Fracture Process Zone (FPZ) before the tests [37]. For all the tests, the size of the initial notch a_0 was geometrically-scaled and equal to $D/5$. Figure 6.2 shows the optical microscope image of a typical notch tip resulting from the our cutting procedure. The tip radius is about $R = 0.23$ mm which is negligible compared to the size of the Fracture Process Zone (FPZ) of the material system investigated in this work which was in the order of several millimeter regardless of the thickness of the structure.

After manufacturing the notch, a layer of white paint followed by the black speckles was sprayed to perform the Digital Image Correlation (DIC) measurements.

6.2.2 Testing

We tested the specimens using a servo-hydraulic, closed-loop Instron 5585H with 200 kN capacity. To prevent strain rate effects, a 0.2 %/min nominal strain rate calculated as $\epsilon_{Nom} = \delta/L$ where δ = displacement from the Instron machine and L = gauge length was used for all the specimens. The load was recorded with a sampling frequency of 10 Hz. In addition, we captured the digital images with a sample rate of 1 Hz using a Nikon D5600 DSLR camera with two lenses: A Nikon AF micro 200 mm and a Sigma 135 mm DG HSM. All the digital images were analyzed using GOM Correlate software [62]. We calculated the nominal displacement, u, by taking the relative average displacement between two horizontal lines across the width placed symmetrically with respect to the notch. To scale this nominal displacement with the specimen size, the distance from the notch was chosen to be 1.2 times D.

6.3 Experimental results

6.3.1 Load-displacement curves

The load and the nominal displacement curves were analyzed after the fracture tests (Fig. 6.3a-d). Similar to other quasibrittle materials [33, 34, 36, 38–41, 45], a strong size effect can be observed in the load-displacement curves reported in Figs. 6.3a-d for all the thicknesses. For instance, in Fig. 6.3a, the size-1 (largest) shows an evidently linear behavior up to the peak load followed by sudden failure and snap-back instability [42], a typical phenomenon of a brittle structure. However, as the specimen size decreases, the load-displacement curve becomes increasingly non-linear before the peak load (see size-4 curves in insets). This is because, as the structure size decreases, the relative size of the FPZ increases and the effects of the sub-critical damage induced in the FPZ becomes more significant.

Another aspect to notice is the increased scatter of the strength as the structure thickness decreases. For DFCs with 1.1 mm thickness (see Fig. 6.3d), it is difficult to distinguish the failure loads between sizes 2 and 3 due to significant scatter in the experimental curves. In

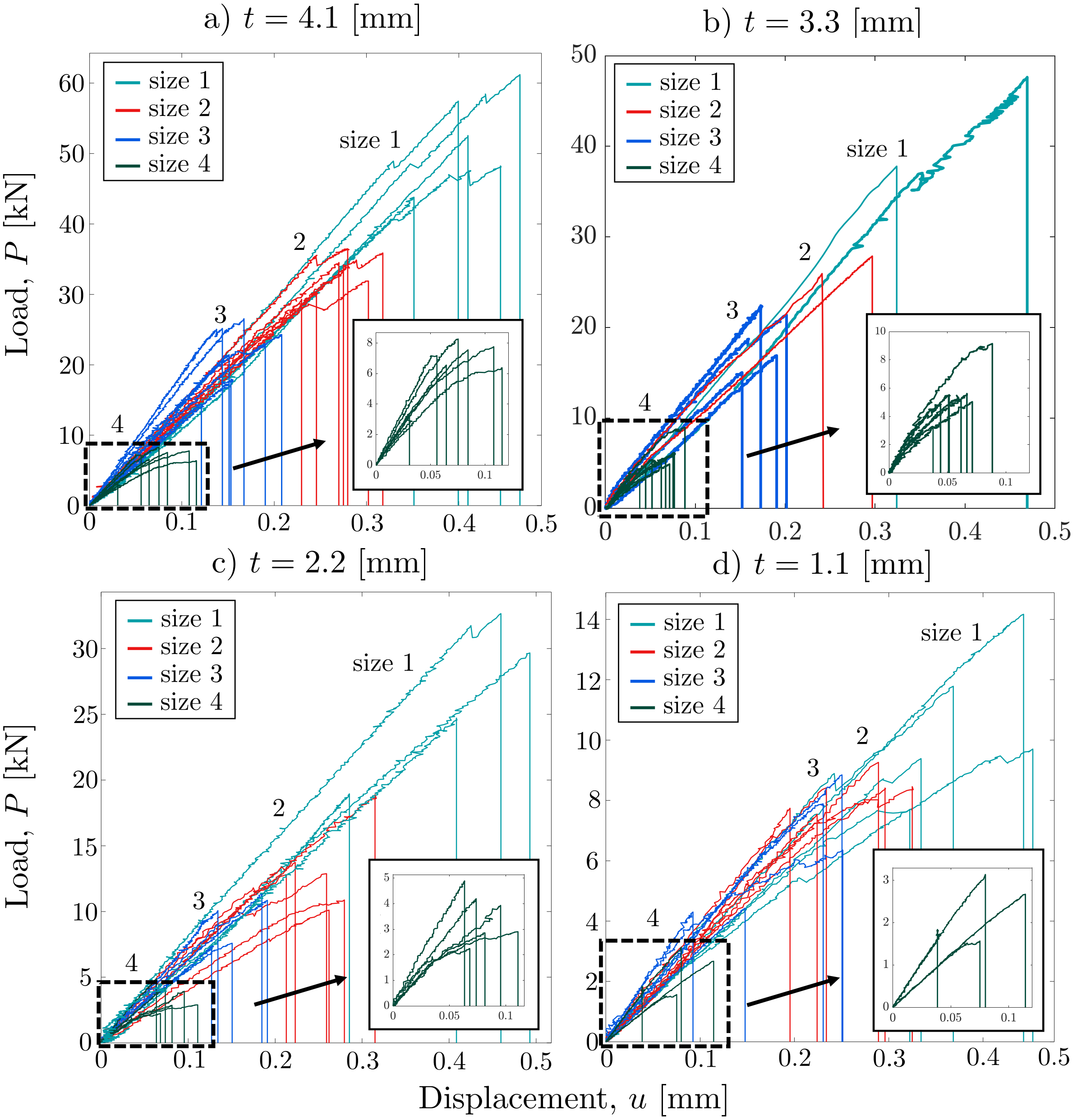

Figure 6.3: Load-displacement curves of DFCs with the thickness of (a) 4.1 mm, (b) 3.3 mm, (c) 2.2 mm, and (d) 1.1 mm.

contrast, for higher thicknesses, the CoV of the data is significantly lower (see Fig. 6.3a). This can be qualitatively explained by considering the mesoscale morphology of DFCs as a function of the structure thickness. We will address this point in section 5.1.

6.3.2 Fracture surfaces

Representative intra-laminar fracture surfaces of the tested specimens are shown in Figs. 6.4a-l. It is important to note that, for all the tests conducted in this investigation, the Fracture Process Zone (FPZ) emerging at the peak load was almost orthogonal to the load direction. After the peak is reached and the specimens exhibit snap-back instability with dynamic crack propagation, the path becomes more tortuous as clearly shown in Figs. 6.4a-l.

It is interesting to note that the fracture paths and the location of the fracture initiation depend on the structure size and thickness relative to the platelet size. For size-1 (see Figs. 6.4a-c), the fracture paths tend to be less tortuous and, on average, almost orthogonal to the loading direction. As the structure size decreases (see Figs. 6.4d-i), the paths become more tortuous and random. The location of fracture initiation also depends highly on the size of the structure. A higher probability of fracture away from the notch can be observed for the smaller sizes (see Fig. 6.5c) due to the larger size of the FPZ compared to the structure dimensions. In fact, the stress redistribution in the FPZ can mitigate the severity of the notch, thus promoting fracture initiation from other weak spots such as resin rich areas, air pockets, and locations where the platelets are unfavourably oriented with respect to the loading direction.

In addition to the structure size, the structure thickness also influences the process of fracture initiation and propagation. In fact, when the average number of platelets through the thickness is sufficiently low (lower than 1.1 mm for the system investigated in this work), the fracture tends to be more affected the presence of weak spots in the material mesostructure rather than the stress-free notch. This is evident in Figs. 6.5 where the DFC specimens featuring a thickness $t = 1.1$ mm exhibit a relatively clean fracture path initiated away from the notch even for size-1. In fact, almost half of the specimens failed away from the notch.

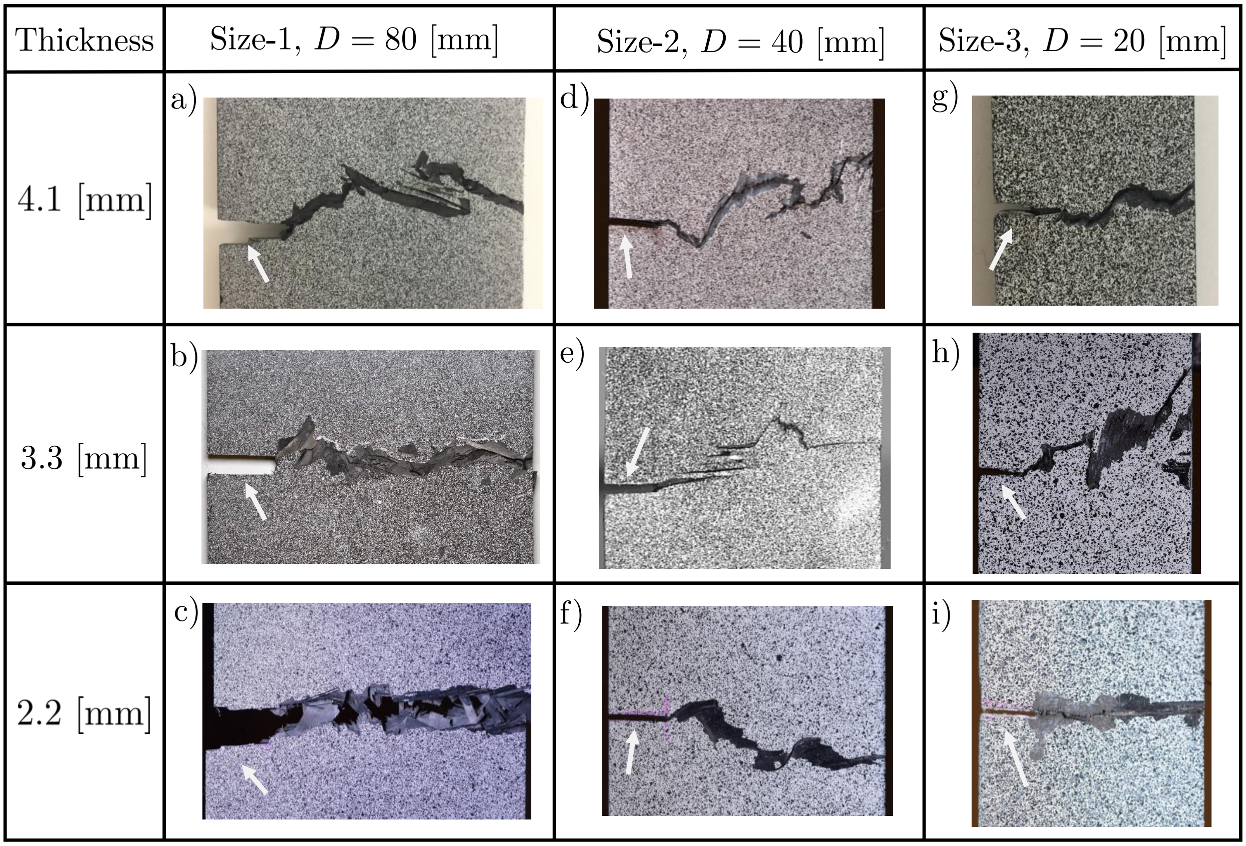

Figure 6.4: Representative fracture surfaces of Single Edge Notch Tension specimens for the thickness of 4.1, 3.3, and 2.2 mm. An arrow indicates an initial notch position.

Thickness	Size-1, $D = 80$ [mm]	Size-2, $D = 40$ [mm]	Size-3, $D = 20$ [mm]
1.1 [mm]	a) 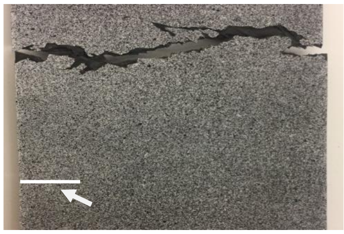	b) 	c) 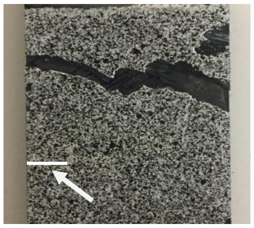

Figure 6.5: Representative fracture surfaces of Single Edge Notch Tension specimens for the thickness of 1.1 mm. As can be noted, most of the fractures were triggered far from the notch.

For larger thicknesses, the notch size featured by size-1 specimens is large enough to make it trigger the fracturing process. Yet, for the specimens with the lowest thickness, the fracture was still substantiated by other weak spots.

As seen from the Figs. 6.4 and 6.5, the fracture patterns of DFCs are generally very complex suggesting an important role played by the heterogeneous mesostructure in driving the unstable crack propagation. To understand the complex fracturing modes, the fracture surfaces were examined by means of a JEOL JSM-7000F field emission Scanning Electron Microscope (SEM). The samples were taken from fractured specimens with a thickness of 2.2 mm and a width of 80 mm. This configuration was found to provide a good representation of the main damage mechanisms identified in this work for all the specimen sizes and thicknesses investigated. As can be noted from Figs. 6.6a-d, multiple damage mechanisms including e.g. delamination between the platelets, platelet splitting, fiber breakages, fiber pullouts, and matrix cracking contribute to the fracturing process. As Figs. 6.6a,b show, fiber breakage and platelet pullout are among the most frequent failure mechanisms along with inter-platelet delamination and matrix crack propagation in resin rich areas (Figs. 6.6c,d). As will be discussed in Section 5 these energy dissipation mechanisms, which in a way remind of the fracture mechanics of an extremely tough material such as nacre [108, 109], provide DFCs with unprecedented damage tolerance and fracture toughness.

6.3.3 Structural size effect on the nominal strength

We define the nominal strength as the failure load, P_c, over the gross cross-section: $\sigma_{Nc} = P_c/Dt$ where D and t are the specimen width and thickness. The experimental results of the average nominal strength are summarized in Table 6.2. As can be noted, the average strength clearly shows a decreasing trend as the structure size increases for all the thickness investigated in this work. To analyze such scaling effect, the following sections introduce a theoretical framework combining equivalent linear elastic fracture mechanics and stochastic finite element analysis.

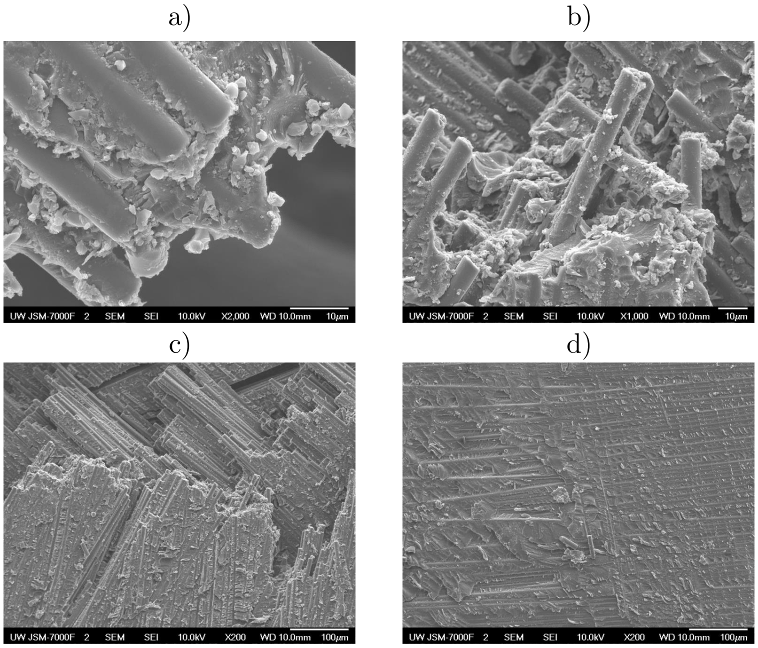

Figure 6.6: Images of the complex fracture surfaces of DFCs using SEM. (a) Fiber breakages, (b) Fiber pullouts, (c) delamination between platelets, and (d) delamination due to resin rich area.

Table 6.2: The average failure strength with standard deviation of tested SENT specimens.

	Failure strength, σ_{Nc} (MPa)			
Thickness (mm)	Size1	Size2	Size3	Size4
4.1	166.7 ± 15.53	216.0 ± 20.31	285.8 ± 32.32	297.7 ± 35.27
3.3	153.8 ± 27.61	198.2 ± 15.54	214.2 ± 14.58	242.2 ± 20.14
2.2	158.2 ± 45.90	200.5 ± 44.11	248.0 ± 71.04	284.3 ± 55.82
1.1	128.5 ± 27.32	180.0 ± 33.82	239.0 ± 80.28	354.8 ± 78.27

6.4 Theoretical Framework

Due to the complex mesostructure, the fracturing process of quasibrittle materials (such as concrete, ceramics, rocks, rigid foams, fiber composites, wood sea ice, stiff soils, consolidates snow and many bio-materials [34,35,37,39,41]) generally features a significant stress redistribution. This phenomenon, which is typically characterized by the emergence of a non-linear fracture process zone (FPZ), leads to a deterministic size effect in structures weakened, prior to maximum load, by stably grown large cracks or by notches. This type of size effect is generally referred to as Type 2 size effect.

In the case of quasibrittle structures of positive geometry, failing at crack initiation from a smooth surface, the size effect is caused by a combination of stress redistribution in the FPZ with strength randomness. In fact, because of the material heterogeneity, a finite FPZ must develop before the cracking can coalesce into a macro-crack of finite length emanating from the surface. At the same time, the location of crack initiation will depend on the spatial random distribution of material strength. This type of energetic-statistical size effect is generally referred to as Type 1 size effect [35,52,53].

The following Sections focus on the characterization and analysis of Type II size effect in DFCs. To capture the scaling of the structural strength in DFC structures weakened by stress-free notches, we combine an equivalent fracture mechanics approach (featuring a characteristic length-scale accounting for the finite size of the FPZ) and stochastic finite element analysis (to account for the random distributions of the platelets) [29, 41].

6.4.1 Analysis of size effect tests by Size Effect Law (SEL) for DFCs

To consider the FPZ, an equivalent crack length, a, is defined as the sum of the initial crack length, a_0 (see Fig. 6.1) and an effective FPZ size, c_f, which is assumed to be a material property:

$$a = a_0 + c_f \tag{6.1}$$

Following dimensional analysis, the energy release rate, G can be written as a function of the dimensionless crack length, $\alpha = a/D$ as follows:

$$G(\alpha) = \frac{\sigma_N^2 D}{E^*} g(\alpha) \tag{6.2}$$

Here, the nominal stress is $\sigma_N = P/Dt$ where P is the load, D is the specimen width, and t is the specimen thickness, E^* is an effective elastic constant, and g is the dimensionless energy release rate which typically accounts for the effects of the geometry on the energy release rate. If the structure is homogeneous, g depends only on the geometry of the structure and takes the same value for geometrically-scaled specimens regardless of the structure size [35, 37]. However, DFCs are highly inhomogeneous materials, the inhomogeneity dimensions being comparable with the size of typical DFC structures. Accordingly, since the inhomogeneity size is not scaled, different structure sizes may lead to a significantly different material morphology thus affecting the energy release and making g dependent on the structure size, D and the thickness t.

We can rewrite the Eq. (6.2) to account for the inhomogeneity of DFCs as follow [35,37]:

$$G(\alpha, D) = \frac{\sigma_N^2 D}{E^*} g(\alpha, D) \tag{6.3}$$

where the effect of the size D on the dimensionless energy release rate is explicitly introduced. In contrast, t is not introduced in the equation since Eq. (6.3) is used here to analyze geometrically-scaled specimens of the same thickness. Accordingly, a different set of dimensionless energy release rate functions, $g\left(\alpha, D\right)$ needs to be calculated for every thickness investigated in this work.

Following the derivations in e.g. [35,37]:

$$G_f = \frac{\sigma_{Nc}^2 D}{E^*}\left[g(\alpha_0, D) + \frac{c_f}{D}\frac{\partial g}{\partial \alpha}(\alpha_0, D)\right] \tag{6.4}$$

Eq. (6.4) can be rearranged into the following form:

$$\sigma_{Nc} = \sqrt{\frac{E^* G_f}{Dg\left(\alpha_0, D\right) + c_f g_D\left(\alpha_0, D\right)}} \tag{6.5}$$

where $g_D(\alpha_0, D) = \frac{\partial g}{\partial \alpha}(\alpha_0, D)$. The subscript D corresponds to the partial differentiation with respect to α for a constant structure size D. It is noteworthy that Eq. (6.5) contains all the necessary components to capture the scaling of the nominal strength of DFC structures. The characteristic FPZ size, c_f, enables to capture the transition from quasi-ductile to brittle fracturing behavior with increasing the structure size. Further, the dimensionless energy release rate parameters, g and g_D combine the geometrical effect as well as the inhomogeneous material characteristics. These parameters can be calculated using the stochastic finite element method described in the following section.

It is worth remarking here that the type 2 Size Effect Law provided in Eq. (6.4) is based on the inherent assumption that the fracture is initiated by the stress-free notch. As the results clearly show for the specimen sizes and platelet dimensions investigated in this work the foregoing condition is generally met when the overall thickness of the plate, t, is larger than 1.1 mm. In such cases, the vast majority of the specimens fail at the notch and the size effect law equipped with the dimensionless energy release rates calculated by means of the stochastic FE framework can be used to estimate the fracture energy of the material. In contrast, for sufficiently low thicknesses ($t < 1.1$ mm for the system investigated in this work), the random distribution of weak spots in the highly heterogeneous mesostructure affects the fracturing behavior more significantly. In such a condition, the type II SEL cannot be used and the description of the failure process can be based on a fully stochastic modeling framework. A full three-dimensional stochastic model to capture these important aspects is under development by the authors. Preliminary results have shown that modeling the random distribution of the platelets explicitly and capturing the damage with proper quasi-brittle damage laws leads to an accurate prediction of the failure location and the structural behavior. However, the discussion of such a modeling framework is beyond the scope of the present manuscript and will be the subject of future publications.

6.4.2 Stochastic finite element model

In order to characterize the fracture energy, G_f and the effective FPZ length, c_f, we need to calculate the dimensionless energy release rate functions, $g(\alpha_0, D)$ and $g_D(\alpha_0, D)$. These are related to a release of elastic energy caused by the creation of new crack surfaces. Due to the inhomogeneous mesostructure, the release of energy is strongly related to two elements in addition to the geometry of the structure: the platelet constitutive properties, and the orientation distribution of the platelets. Therefore, modeling the distribution of the platelets explicitly is key. More details on the algorithm and its implementation can be found in [29].

Using the mesostructure generation algorithm, we first investigate the mesoscale morphology of DFCs with respect to the structure thickness. The distributions of the average platelet orientations through the thickness are considered. We generate a size 1 specimen ($L = 178, D = 80$ mm) for 4 different thicknesses using the same Cumulative Distribution Function (CDF) of in-plane platelet orientations. The range of the platelet orientation is $-90° \leq \theta \leq 90°$. We calculate the average absolute platelet orientations through thickness, θ_A, in each partition. Figure 6.7 presents the Probability Density Function (PDF) of θ_A for each thickness. The bar graphs represent the frequency of θ_A from the mesostructure generation algorithm whereas the solid line represents a Gaussian probability fitting. As can be noted, the mean θ_A stays near $\approx 45°$ regardless of the structure thickness. However, the standard deviation changes dramatically with respect to the thickness, from 4.01° for $t = 4.1$ mm to 8.59° for $t = 1.1$ mm. To visualize the differences, we calculate the probability of $\theta_A \geq 55°$, represented as shaded areas in Fig. 6.7. For $t = 4.1$ mm, the probability is 0.56%

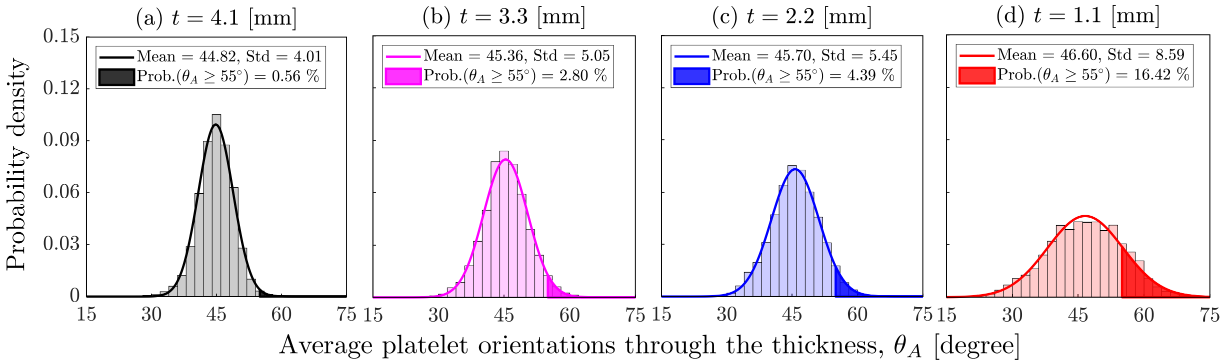

Figure 6.7: Probability density distributions of the average platelet orientations through the thickness, θ_A, obtained by simulation. Plate thickness: (a) 4.1 mm, (b) 3.3 mm, (c) 2.2 mm, and (d) 1.1 mm.

which is tremendously small comparing to 16.42% for $t = 1.1$ mm. This study quantitatively confirms that the probability of having unfavorable platelet orientations increases as the structure thickness decreases if the CDF of in-plane platelet orientations remains consistent. As a result, the average strength of DFCs deviates significantly in lower thickness as we observed from the experiments. It is worth mentioning that the results of this qualitative investigation are related to DFC plates where the distribution mechanism of platelets is not affected by the thickness.

A different scenario can be expected in structures featuring complex geometrical features in which high platelet flow can occur. In such a case, the effect of the thickness of the structure must be investigated via an accurate morphological study.

The generated mesostructure is now transferred to Abaqus/Standard [73] to find the dimensionless energy release rate functions (see 5.5.1 for the detailed implementation). Due to the stochastic nature of the problem, a total of 10 repetitions for each specimen sizes are simulated to find the average g and g_D. The process is repeated for all 4 different thicknesses. It is worth mentioning that additional 10 structures were generated for the thickness of 1.1

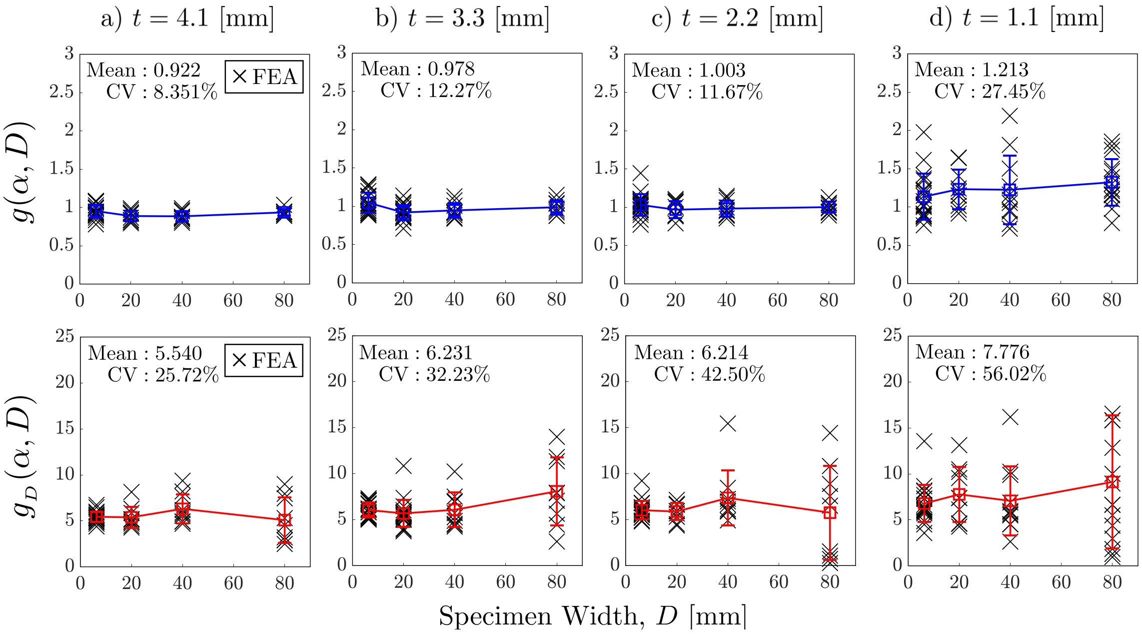

Figure 6.8: Dimensionless energy release rate parameters, g and g_D for the thickness of (a) 4.1 mm, (b) 3.3 mm, (c) 2.2 mm, and (d) 1.1 mm.

mm due to its high variations found in g and g_D. A summary of all the results is provided in Fig. 6.8 whereas the mean and standard deviation for each thickness is given in Table 6.4. As can be noted, for thicknesses higher than 2.2 mm, the effect of the structure size in g and g_D is negligible. Especially, for the thickness of 4.1 mm, there is hardly no dependency in g and g_D with the size of the structure. This is because for sufficiently large thicknesses spatial distribution of platelets becomes almost uniform, and the in-plane behavior becomes closer to the one of an homogeneous medium. As a result, g and g_D do not change for the geometrically-scaled structures. However, the effect of the material inhomogeneity remains strong for the $t = 1.1$ mm. As can be noted from Fig. 6.8d, the g and g_D change with respect to the structure size with large deviations. This is consistent with the observations made in section 3.1 and Fig. 6.3.

Although for $t \geq 2.2$ mm the dimensionless functions where shown to be basically unaf-

Table 6.3: Elastic material properties for the T700G and matrix layers.

Properties	T700G	Matrix
Platelet initial thickness, t_p [mm]	0.139	Varies
Longitudinal modulus, E_1 [GPa]	135	3
Transverse modulus, E_2 [GPa]	10	3
Shear modulus, G_{12} [GPa]	5	1.1
Poisson ratio, ν_{12}	0.3	0.35

fected by the structure size, we decided to use the average value of g and g_D for each structure sizes. While for the specimens investigated in this work, this can be shown to provide little difference on the estimated fracture energy and equivalent FPZ size, we made this choice for the sake of providing a general framework. In fact, a different platelet morphology could lead to more significant effects of the structure size. Another reason for adopting the general framework is that we investigated the use of Eq. (6.5) for the estimation of the fracture energy of the specimens featuring a thickness of 1.1 mm. In such a case, the dimensionless functions were shown to be size-dependent.

It is worth mentioning that for $t = 1.1$ mm the inherent assumption of the fracture being triggered by the stress-free notch was not met in almost half of the tests. In this scenario, a fully stochastic, mesoscale computational framework is needed to describe the fracturing behavior. Yet, we decided to verify if Eq. (6.5) could still be used to fit the size effect on the specimens that did fail by crack onset from the notch. A separate discussion regarding the size effect reported in the specimens featuring a thickness of 1.1 mm is provided in the following sections.

6.4.3 Fitting of the experimental data using the SEL

To find the fracture properties G_f and c_f, we combine the experimental results and the stochastic finite element model using Eq. (6.5). To do so, we introduce the following variables:

$$X = \frac{g}{g_D} D, \quad Y = \frac{1}{g_D \sigma_{Nc}^2} \tag{6.6}$$

Using theses variables, Eq. (6.5) can be transformed into the following linear expression:

$$Y = C + AX \tag{6.7}$$

with:

$$C = \frac{c_f}{E^* G_f}, \quad A = \frac{1}{E^* G_f} \tag{6.8}$$

Finally, the fracture energy, G_f, and the effective size of FPZ, c_f, are:

$$G_f = \frac{1}{E^* A}, \quad c_f = \frac{C}{A} \tag{6.9}$$

Figures 6.9a-d plot the linear regression analysis introduced in Eqs. (6.6) and (6.7) for the tests conducted in this work from which G_f and c_f can be calculated leveraging Eqs. (6.9).

6.5 Discussion

The theoretical framework described in foregoing sections can then be used to estimate the fracture energy of the material and the effective FPZ length. The measured G_f and c_f for various thicknesses are reported in Table 6.4, the standard deviations being calculated following [36]. Also, they are plotted in Fig. 6.10 along with a typical Al5083 [105] and T700G Quasi-Isotropic (QI) laminate composite [29] with a thickness of 3.1 mm.

As can be noticed, the intra-laminar mode I fracture energy of DFCs are outstanding compared to Al5083, $G_f^{Al} = 12.0$ N/mm and even to the QI laminate composite, $G_f^{QI} = 41.01$ N/mm. In fact, the measured G_f for the DFC plates investigated in this work are 49.54, 63.47, 40.32, and 34.55 N/mm for thickness of 4.1, 3.3, 2.2, and 1.1 mm respectively. It is worth noting that these measured G_f are $2.9 - 5.3$ times larger than the typical values of

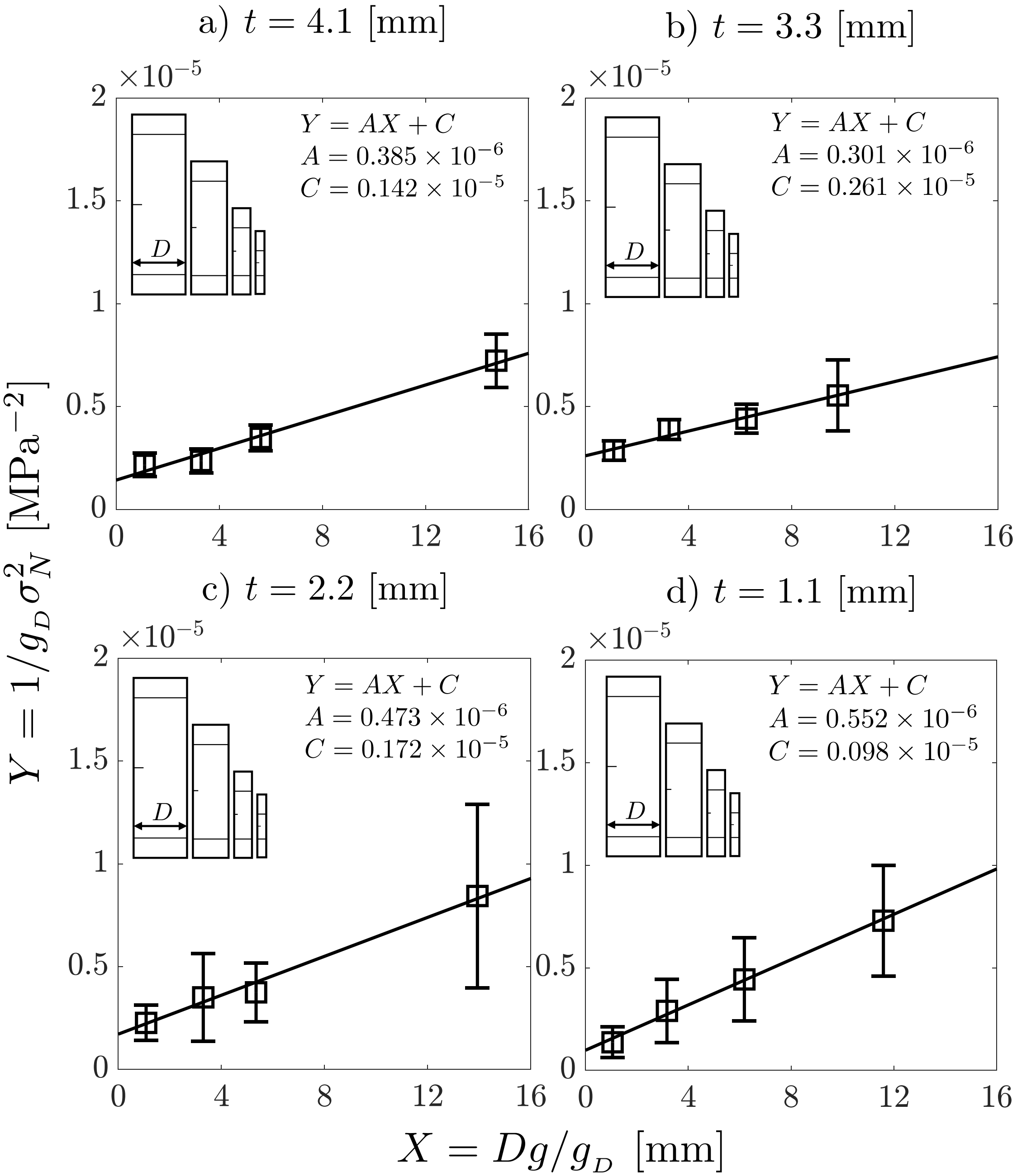

Figure 6.9: Linear regression analysis to find the fracture properties of DFCs with thickness of (a) 4.1 mm, (b) 3.3 mm, (c) 2.2 mm, and (d) 1.1 mm.

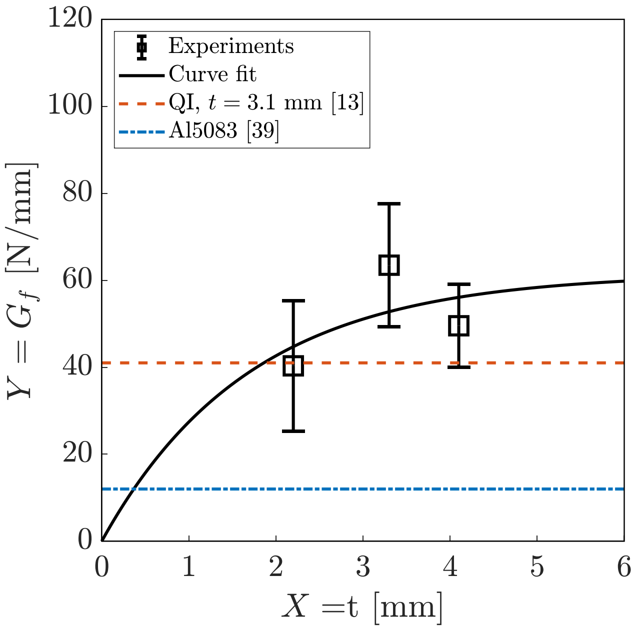

Figure 6.10: Measured fracture energy of DFCs with the exponential least square fitting.

an aluminum alloy which is the main competing material of DFCs in the current aerospace industry. If ones consider the weight saved by using fiber composite structures, having such a high G_f opens new avenues for DFC structures especially for crashworthiness applications. Even compare with the QI laminate composite made of the identical prepreg system, DFCs with equal thickness provide as much as 1.5 times higher G_f in the case of t =3.3 mm, thanks to the additional energy absorption mechanisms provided by complex mesostructure.

From Fig. 6.10, we also observe that G_f depends strongly on the thickness of DFC plates. According to Fig. 6.10, G_f increases gradually up to about 45.03 N/mm for a thickness of $\sim$ 2 mm. Then, it slowly approaches an asymptotic value of about 57.77 N/mm for larger thicknesses. As can be noted, the fracture energy seems to follow an exponential trend, $Y = A(1 - e^{BX})$ with $A = 57.77$ and $B = -0.76$ although more data points for larger thicknesses are needed to completely clarify this aspect.

When DFCs contain a sufficient number of platelets, the mesoscale morphology becomes

Table 6.4: The fracture properties and dimensionless energy release rate parameters calculated from the experiments and the stochastic FEM.

Thickness (mm)	Fracture energy, G_f (N/mm)	Effective FPZ length, c_f (mm)	$g(\alpha_0)^*$ -	$g_D(\alpha_0)^*$ -
4.1	49.54 ± 9.57	3.69 ± 0.51	0.92 ± 0.08	5.54 ± 1.43
3.3	63.47 ± 14.16	8.67 ± 1.37	0.98 ± 0.12	6.23 ± 2.01
2.2	40.32 ± 14.98	3.63 ± 0.97	1.00 ± 0.12	6.21 ± 2.64
1.1	34.55 ± 9.50	1.78 ± 0.30	1.21 ± 0.33	7.78 ± 4.36

* Averaged FE simulation results from each thicknesses.

more uniform and the amount of fracture area created in the FPZ reaches a limit value, leading to no further changes of G_f with increasing plate thickness. This result provides an important index for the engineers who want to optimize the thickness of DFCs. Increasing the thickness of DFCs will not provide a further benefit in terms of the G_f after $t \sim 3$ mm. For decreasing the thickness, we recommend paying extra attention because the fracture energy starts to drop significantly below $t \sim 2$ mm. The effective FPZ size, c_f also follows the similar trend. The c_f for the thickness of 4.1, 3.3, 2.2, and 1.1 mm are 3.69, 8.67, 3.63, and 1.78 mm respectively. This is an agreement with noticeable quasi-ductile fracturing behavior of thicker DFCs.

6.5.1 Effective Fracture Process Zone (FPZ) length

In the foregoing section, the effective FPZ length, c_f, is estimated leveraging size effect testing. This parameter is a measure of the size of the FPZ and should be large enough to provide a representative description of the main damage mechanisms in the FPZ. In materials featuring inter-granular damage (see Fig. 6.11), the effective FPZ is generally linked to the characteristic size of the inhomogeneities, h. Since the damage occurs mainly between the particles, c_f should span at least two or three inhomogeneities. The typical example of such a material is concrete in which the damage in the FPZ occurs in the form of distributed microcracking in the brittle mortar phase connecting the aggregates (see e.g. [36]). In materials characterized by intra-granular damage, it is possible that the representative volume of the main damage mechanisms in the FPZ is a fraction and not a multiple of the grain size. Our morphological analysis of the fracture surfaces suggests that DFCs belong to the latter rather than the former class of quasibrittle materials. In fact, as can be noted from Fig. 6.6 the main damage mechanisms in the FPZ are fiber failure and platelet pullout, matrix microdamage, and platelet delamination. All these phenomena involve regions spanning a fraction of the platelet width, h. In light of this, it not surprising that the effective FPZ length found from our size effect tests is in the order of the platelet width, $c_f \approx (1/2-1)h$ (See Fig. 6.11b). According to our study, this region provides a good statistical representation of the main damage mechanisms occurring in the FPZ.

6.5.2 Size Effect Curves

We can also plot the size effect curves using the experimental values and the finite element modeling results. To do so, the Eq. (6.5) is rearranged as follow [35]:

$$\sigma_{Nc} = \frac{\sigma_0}{\sqrt{1 + D/D_0}} \tag{6.10}$$

where $\sigma_0 = \sqrt{E^* G_f / c_f g_D}$ and $D_0 = c_f g_D / g$. The normalized size effect curves are plotted using the following axes:

$$Y' = \frac{\sigma_{Nc}}{\sigma_0}, \quad X' = \frac{D}{D_0} \tag{6.11}$$

In Fig. 6.12, the size effect curves are plotted in a double-logarithmic scale. There are two asymptotes in the plots: the horizontal asymptote represents the strength predicted by the strength-based failure criterion, on which the size effect is negligible. The oblique asymptote with a slope of $-1/2$ represents the nominal strength according to LEFM. As can be noticed, regardless of all the explored thicknesses, DFCs show a strong size effect. Additionally, the

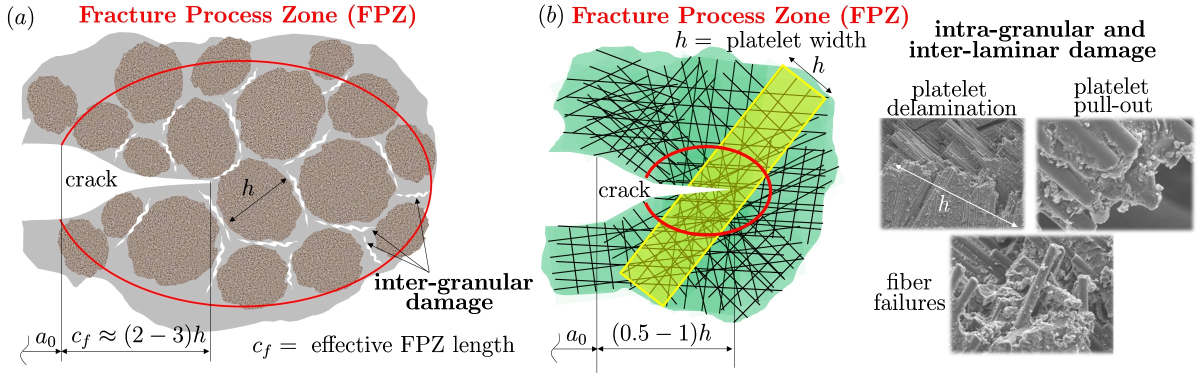

Figure 6.11: Fracture Process Zone (FPZ) and effective FPZ length, c_f, in quasibrittle materials: (a) materials featuring inter-granular damage (such as e.g. concrete) are typically characterized by $c_f \approx (2-3)h$ with $h =$ inhomogeneity characteristic size; (b) DFCs characterized by intra-granular and inter-laminar damage. In such a case, the main damage mechanisms such as platelet delamination and pull-out, and fiber failure occur in regions spanning a fraction of the platelet width, h. Accordingly, in DFCs the effective FPZ length correlates with the platelet width, $c_f \approx (1/2-1)h$, not with the platelet length.

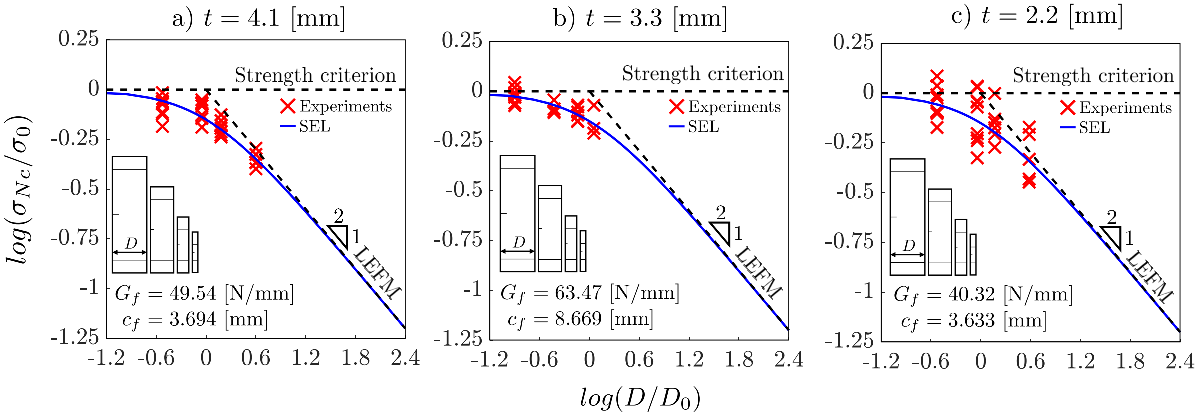

Figure 6.12: Measured size effects for DFCs with thickness of (a) 4.1 mm, (b) 3.3 mm, and (c) 2.2 mm. DFCs outperformed the aluminum as well as the quasi-isotropic laminate.

experimental data clearly show a transition from stress-driven to energy-driven failure. This transition can be explained by considering the relative size of the FPZ compared with the structure size. The relative size of the FPZ, which is a material property, increases as the structure size decreases. Therefore, the nonlinear effect induced by the micro-damage in front of the crack-tip becomes non-negligible. For sufficiently small structures, the effect is so significant to cause a strong deviation from the LEFM. On the other hand, the effect of the FPZ is reduced as the structure size increases and the size effect is well captured by the LEFM.

The characteristic size of the FPZ, c_f, increases with the range of thickness tested in this study (see Table 6.4). The thinnest DFCs are showing the most brittle failure with the smallest effective FPZ size, c_f, and fracture energy, G_f (see Fig. 6.12d). As the thickness increases, DFCs show pronounced pseudo-ductile response (see Fig. 6.12a).

6.5.2.1 Size Effect in thin DFC specimens

It is interesting to discuss the fracturing behavior of the specimens with $t = 1.1$ mm. For such a low thickness, corresponding to an average number of platelets through the thickness of about 8, almost half of the specimens exhibited fractures starting far from the stress-free notch. As discussed in the foregoing sections, this phenomenon is related to an increasing probability of having regions with platelets that are unfavourably oriented with decreasing thicknesses. In such a scenario, the number of specimens whose failure is substantiated by weak spots related to the random heterogeneous mesostructure increases and the size effect on the nominal strength transitions from Type 2 to Type 1. To capture this transition and the subsequent energetic-statistic size effect, a full three-dimensional stochastic computational framework is under development by the authors. However, since about half of the specimens with $t = 1.1$ mm did fail from the stress-free notch, it is interesting to discuss the fitting of the related data by Type 2 SEL. Fig. 6.13 shows the size effect curve for the thickness of 1.1 mm where the notch insensitive fractures are marked with a black circle on top of their experimental value. For such fractures, the equivalent LEFM approach described in the foregoing sections cannot be applied and the size effect should start to follow a different trend. However, it is remarkable to note that not only the specimens failing from the notch but also the ones with fractures triggered far from the notch can be fitted by means of Eq. (6.10). This is probably owed to the fact that, for this thickness and the size range investigated in this work, the weak spots in the material and the stress-free notch exhibit a similar severity. This result, however, is not general and applies only to the given range of thickness and structure sizes investigated in the present study. For lower thicknesses, Type 1 would likely be the dominating size effect and the experimental data on the nominal strength would follow a very different trend. Yet, it should be noted that most of the DFC structures used in engineering features thicknesses significantly larger than 1.1 mm. Accordingly, in practical situations the size effect of DFC structure or components featuring stress-free notches or defects can generally be described by the equations introduced in Section 4.

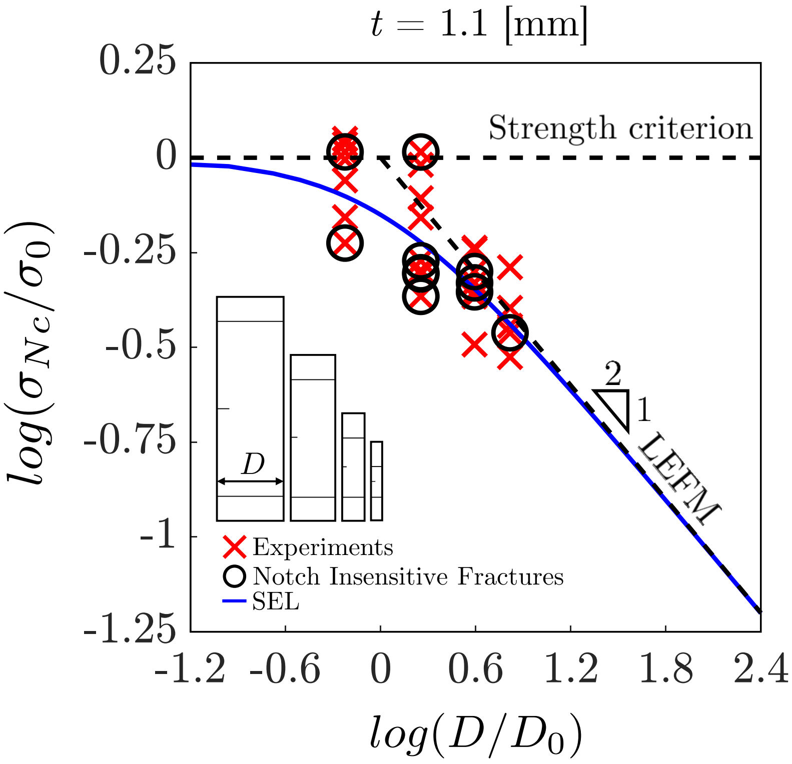

Figure 6.13: Measured size effects for DFCs with thickness of 1.1 mm. Notice that almost half of the specimens fractured away from the notch. However, the size effect law still captures the scaling effect of DFCs.

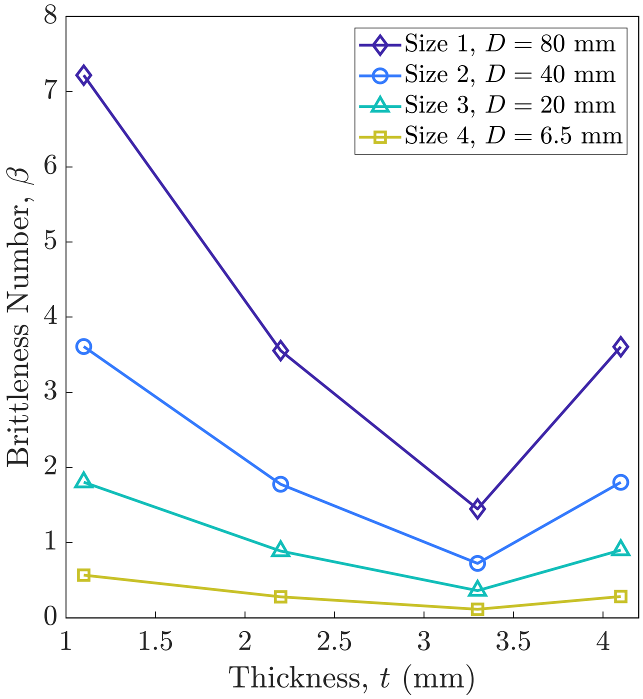

Figure 6.14: Change of the brittleness number, β, as a function of the thickness for all the experimented sizes.

6.5.3 Remarks on the structural design with DFCs

Based on the foregoing observations, we can conclude that the strong quasibrittleness of DFCs must be taken carefully in the design of DFC structures with sharp notches or defects. Neither traditional LEFM nor strength-criteria have the capability to precisely extrapolate the structural strength from the tested specimens, most of which belong to the transitional zone. When estimating the strength of larger structures, LEFM significantly underestimates the strength whereas strength-criteria overestimates it. If we continuously adapt LEFM in designing of DFC structures, the underestimations of strength capability may hinder the possible applications of DFCs in engineering applications. Therefore, a proper model equipped with a characteristic length scale such as SEL or other equivalent models must be utilized to capture the quasibrittleness of DFCs.

6.6 Conclusions

Combining experiments and stochastic finite element modeling, this work studied the fracturing behavior and scaling effect of Discontinuous Fiber Composite (DFC) structures with different thicknesses. The following conclusions are drawn based on the results of this study:

1. The experimental results on geometrically-scaled Single Edge Notch Tension specimens of four distinct thicknesses showed a significant size effect on the nominal strength of DFC structures. For a given thickness, smaller specimens exhibited a pronounced pseudo-ductile fracture behavior with minimum scaling effect. In contrast, when the size of the specimen was sufficiently large, the scaling of the nominal strength approached Linear Elastic Fracture Mechanics (LEFM) asymptotically and fracture occurred in a very brittle manner;

2. The transition from pseudo-ductile to brittle fracture with an increasing specimen size is related to the development of a significant Fracture Process Zone (FPZ) whose dimensions were found to be comparable to the platelet size. In the FPZ, significant non-linear deformations due to sub-critical damage mechanisms, such as platelet delamination, matrix microcracking, and platelet splitting/fracture, promote strain redistribution and mitigate the intensity of the stress field induced by the crack/notch. This phenomenon is more pronounced for small structures since the size of a fully-developed FPZ is typically a material property and thus its influence on the structural behavior becomes increasingly significant as the structure size is reduced. For sufficiently large structures, the size of the FPZ becomes negligible compared to the structure's characteristic size in agreement with the inherent assumption of the LEFM that non-linear effects are negligible during the fracturing process;

3. A significant effect of the thickness was also found on the nominal strength of DFC structures and its Coefficient of Variation (CoV). For a given specimen size, thinner specimens tended to fracture in a relatively brittle way with the nominal strength

being closer to LEFM compared to thicker specimens. At the same time, the scatter of the experimental data increased with decreasing thickness from values in the order of 9.31% for a thickness of 4.1 mm to 21.26% for a thickness of 1.1 mm for the size 1 specimens;

4. The highest scatter of the tests on thinner specimens was confirmed by the analysis of the fracture morphology. For a given specimen size, the fracture process in thick DFCs was mostly driven by the FPZ developing at the notch tip. In contrast, the fracture of thin specimens was often initiated far from the notch, showing that failure was driven by random weak spots in the material rather than the notch. This phenomenon is related to the average number of platelets through the thickness: when this number is low, the probability of having weak spots with platelets that are not favorably oriented with respect to the load increases if one assumes the distribution mechanism of platelets is not affected by the thickness. This was clearly showed in this work by numerical simulations that reported a shift of the PDF of average platelet orientation through the thickness towards larger angles compared to the load axis with decreasing thickness;

5. To investigate the effect of the plate thickness on the fracture energy, G_f, and the effective length of the fracture process zone, c_f, the approach combining equivalent fracture mechanics and stochastic finite element modeling proposed in [29] was used. This model accounts for the effects of the complex random mesostructure of the material by modeling the platelets explicitly. This theoretical framework was able to describe the scaling of structural strength and enabled the characterization of the mode I fracture energy of DFCs;

6. G_f and c_f were estimated for a platelet size of 50×8 mm, and a structure thickness of 4.1, 3.3 2.2, and 1.1 mm respectively. It was found that $G_f = 49.54 \pm 9.57$ N/mm, 63.47 ± 14.16 N/mm, 40.32 ± 14.98 N/mm, and 34.55 ± 9.50 N/mm while $c_f = 3.69 \pm 0.51$ mm, 8.67 ± 1.37 mm, 3.63 ± 0.97 mm, and 1.78 ± 0.30 mm. These results clearly indicate

a strong effect of the thickness on the fracture properties of the material. In particular, the fracture energy was found to increase gradually with the plate thickness up to an asymptotic value of about 58 N/mm when the thickness becomes larger than 3 mm. Further computational studies are ongoing to confirm this trend and to extend the study to other platelet sizes and plate thicknesses;

7. For all the thicknesses investigated in this work, the analysis of the fracture tests highlighted outstanding fracture energy of DFCs, from 2.9 to 5.3 times larger than the one of a typical Al5083 or a Quasi-Isotropic laminate made from the same prepregs for the platelet size investigated in this work. This result is particularly interesting in view of a possible use of DFCs for crashworthiness applications;

The critical investigation of the foregoing results can pave the way for the development of novel strategies for the tuning of the fracturing behavior leveraging the DFC mesostructural morphology.

Chapter 7

COMPUTATIONAL INVESTIGATION OF NOTCHED DFC COUPONS

7.1 Introduction

Discontinuous Fiber Composites (DFCs) provide unique opportunities to the composite industry to fulfill the need for large volume manufacturing capability with complex geometries [115]. This is possible because DFCs are made of chopped prepreg tapes. Short, chopped prepreg tapes can follow the contour of the mold more easily than continuous fibers [116]. Therefore, the compression molding technique becomes an ideal manufacturing method for DFC, unlike continuous fiber composites. Consequently, DFCs are suitable to fit into the complex molds within a short manufacturing period. Because DFCs are made of prepreg tapes, the loss of fiber volume fraction is minimized ($50 \sim 55\%$ [117]) compared to the short fiber composites. Therefore, DFCs possess comparable strength ($\sim 60\%$) and stiffness ($\sim 80\%$) with typical quasi-isotropic laminate composites [22]. Additionally, by controlling the size of the platelets, the material properties of DFCs can be engineered. In the early stage of studying DFCs, researchers have focused on finding the relationship between the material responses and the corresponding meso-structure often defined by the platelet size, platelet aspect ratio, tow thickness, and structure thickness [9, 22–24, 29, 30, 97]. The most studied aspect is the platelet size. The mechanical response of the various platelet sizes, tow thicknesses, and aspect ratios have been investigated. The experimental results show that the strength of DFCs increased with the larger platelet size, narrow aspect ratio, and thinner tow thickness. However, the optimum platelet size for the certain structural applications must be chosen based on the mechanical performance and processability [118]. As the platelet size increases, the performance of DFCs also improves such as strength [9, 23] and fracture energy [29]. However, shorter and smaller platelet sizes are much easier to follow the contour of the molds. Those platelets have advantages towards the manufacturing capability. Therefore, to find the optimum size of the platelets, we should compromise between the performance and manufacturing capability. Structure thickness and platelet tow thickness are also widely studied. A strong anisotropic material like DFCs has a non-negligible size effect in a thickness direction. As the structure thickness increases, we observe the strength and fracture energy increases as well while the variation of material properties saturates [9,23,24,30]. The tow thickness has an opposite trend. The structure strength increases as the tow thickness decreases [12,23]. However, the associated fracture behaviors with changing tow thicknesses have not fully characterized. This is because executing experiments in such that distinguishing the material size effect from the structural size effect is a big challenge. Besides the platelet and structure morphology, the manufacturing and curing process of DFCs have also been widely studied. Preetam and Lloyd [119] expressed the importance of the adhesion between the plies and found that the fracture energy can be doubled depending on the surface bonding process. Wan and Takahashi [13], and Nilakantan and Nutt [120] investigated the molding pressure and temperature during the curing process. They found the strength of DFCs increased as the temperature and pressure increased.

Based on the experimental findings, researchers now focus on constructing the computational models. One of the key aspects of modeling DFCs is to capture the meso-structure composed of randomly distributed platelets of finite length. There are multiple ways to characterize the meso-structure. First, direct measurements of the DFC structures are possible using X-ray μComputed Tomography (μCT) [56,60,61]. This technique provides an excellent measurement of platelets' orientations although it may not be the most accessible option considering the significant costs. Favaloro et al. [60] successfully integrated direct measurement from X-ray scan with the finite element model to create a digital copy of the scanned DFC structure. The simulation results match precisely with the experiment results including the location of the crack propagation. Utilizing the measurements from CT scan such as the average platelet orientation tensors, Kravchenko et al. [23,24] created the stochastic finite element model adapting a commercial software Digimat [121]. The FE model captures the effects of tow thicknesses, structure thicknesses, and platelet orientation distributions. Another possibility is to obtain an indirect measurement via optical microscopy of a statistically significant number of materials cross sections [14]. However, this approach can be extremely time consuming since its accuracy strongly correlated with the number of samples investigated and their locations. Finally, numerical generations of the platelets using the predefined probability of the fiber orientations are presented [12,14,14,29,30,67]. By calibrating the distributions of the fiber orientations obtained by the experimental observations using the µCT scanner and microscopes, the computational approach provides a robust method to study the meso-structures of DFCs.

This manuscript is an extension of previous studies by Ko *et al.*. [29,30,32]. Therein, the authors found the fracture energy of mode I intralaminar fracture energy of DFCs with respect to the platelet size and structure thickness, elaborating the strong size effects possessed in DFCs. This paper provides a novel approach to build a computational model for DFCs capturing the size effects which is shown to be efficient and accurate. The model is calibrated leveraging the previous experimental results. Then, we study the failure mechanisms of DFCs and predict the strength of different meso-structure of DFCs.

7.2 Computational Model Setup

7.2.1 meso-structure generation algorithm

To accurately create meso-structures of DFCs, it is critical to explicitly model the depositions of the platelets. The developed random platelet generation algorithm from the previous studies [29,30] explicitly generates the platelets into the given space with the assigned probability distributions in fiber orientations and the locations of the platelets' center point. Researchers have found that the in-plane orientations of the platelets in parts featuring relatively low flow can be well described by a uniform distribution, and therefore, the algorithm uses the uniform distribution from 0 to 180° [14, 60]. However, the algorithm can take any probability distributions depending on its manufacturing process. The platelet information is saved into the partitioned space. The partition-based method is an efficient method to save the random distributions of the platelets [12, 29, 30, 60, 67]. We use square, uniform, 1 $mm \times 1$ mm size partitions for simplicity and robustness of the computational model. However, it is worth mentioning that other options are available. Li et al. [14], for instance, utilized Voronoi diagram shaped partitions to mimic the surface of DFCs. The algorithm generates the platelets until the number of average platelets through the thickness in the whole domain reaches the desired value. Each platelet thickness is adjusted in order to indirectly simulate the flow of the platelets. At this step, we also introduce layers of resin where there is a lack of platelets through the thickness. A detailed description of the generation process can be found in Chapter 4.

7.2.2 Build a stochastic finite element model

The stored platelet information inside the partitions is transferred to a finite element model in Abaqus CAE [73]. The model contains 2D layers of partitioned parts with the corresponding platelet information. The partitioned layers are modeled using S4R shell elements which is a 4-node, quadrilateral conventional shell elements with reduced integration. The in-plane damage behaviors such as the fiber and matrix failure are captured by the Hashin failure criteria [75]. We use a linear softening damage evolution to model the post-peak behaviors of the platelets. From previous studies [29, 30], we have observed extensive damage developed in-between the platelets. Therefore, layers of cohesive elements are inserted between the platelets to capture the out-of-plane interlaminar failures. We choose COH3D8, 8-node 3D cohesive elements, with quadratic stress criteria as the failure criteria and a linear traction-separation law for the post-peak behaviors. The utilized cohesive laws are regularized such that they are mesh-objective and guarantee the correct dissipation of the fracture energy. A schematic of the model is in Fig. 4.10. By taking advantage of the shell elements along with the 3D cohesive elements, the model contains the necessary degrees of freedom to capture the failure mechanisms of DFCs with a relatively low computational cost. The size of the

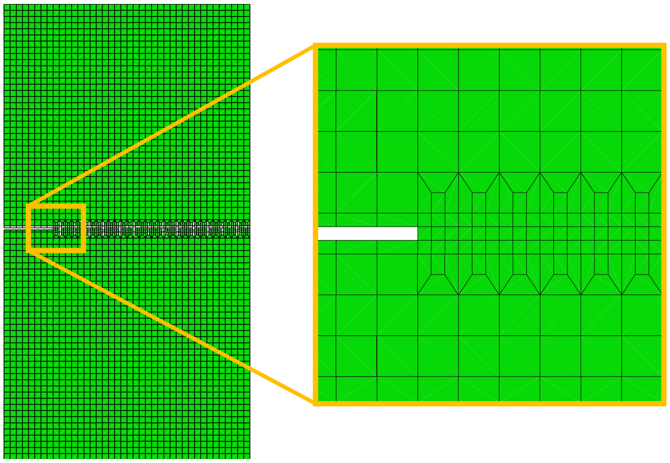

Figure 7.1: Meshing of the single edge notch tension specimen. (a) The global mesh size is 1×1 mm. (b) In front of the crack tip, the mesh size reduces to $\frac{1}{3}$ mm. The size of the mesh in front of the crack tip is much smaller than the size of fracture process zone. Therefore, it is suitable to describe the notch of the quasi-brittle material.

mesh is restricted by the size of the partition since an element cannot overlap between the partitions. At the location of the notch, a size of mesh is reduced to $\frac{1}{10}$ of the size of fracture process zone (FPZ) to capture the nonlinear behavior in front of the notch tip (see Fig. 7.1). The effective FPZ size for DFCs with the platelet size of 50×8 mm and thickness of 2.2 mm is found to be 3.63 mm [30]. A larger number of elements is desirable to fully capture the cohesive law [40]. The size of the mesh located outside of the notch region is set to be equal to the partition size. A mesh sensitive study is performed and showed minimum change with reduced size of the mesh.

To calibrate the model, a set of the size effect experimental results from the previous study [30] is used. The size effect tests are carried on three different sizes of geometrically scaled single edge notch tension specimens. Size effect testing of notched structures is the only way to fully characterize the energetic size effect in quasibrittle composites, as abundantly shown in several recent publications [36, 37, 42]. We only need to calibrate once with a single type of DFC size effect tests. For the baseline, we use the platelet size of 50×8 mm and thickness of 4.1 mm. The calibrated material properties of the platelet and resin are in Table 7.1, the cohesive elements are in Table 7.2.

Table 7.1: Calibrated material properties for the platelets, and resin layers.

Properties	Platelet	Resin
Initial thickness, t [mm]	0.139	varies
Longitudinal modulus, E_1 [GPa]	135	3
Transverse modulus, E_2 [GPa]	10	3
Shear modulus, G_{12} [GPa]	5.2	1.1
Poisson's ratio, ν_{12}	0.35	0.35
Longitudinal tensile strength, σ_1 [MPa]	2172	55
Transverse tensile strength, σ_2 [MPa]	55	55
Longitudinal shear strength, τ_{12} [MPa]	154	55
Transverse shear strength, τ_{23} [MPa]	61.49	55
Longitudinal tensile fracture energy, G_{f1} [N/mm]	60	1.0
Transverse tensile fracture energy, G_{f2} [N/mm]	1.0	1.0

In Fig. 7.2, calibrated simulation results of different coupon sizes are plotted. Three representative curves match well with the experiment average results plotted in dashed lines. We use a single parameter set for all the sizes. As can be noted, as the size increases, the force and displacement curve shows brittle failure. It means that the material behaves differently depending on the structural size, a simplified description of the quasi-brittle material. We simulated 20 coupons per size and obtain the average and standard deviation. The results are plotted in Fig. 7.3.

In Fig. 7.3, simulations and experimental results are plotted in log-log scale. The parameter D represents the width of the specimen and σ_{NC} corresponds to the nominal strength of the coupon. The nominal strength is defined as a $P/(Dt)$ where P is the maximum load

Table 7.2: Calibrated material propertiesfor the cohesive elements.

Properties	Value
Mode I tensile strength, $\sigma_{I,coh}$ [MPa]	180
Mode II, III tensile strength, $\sigma_{II,III,coh}$ [MPa]	180
Mode I fracture energy, $G_{fI,coh}$ [N/mm]	1.0
Mode II, III fracture energy, $G_{fII,III,coh}$ [N/mm]	4.0

and t is the coupon thickness. The size effect law extrapolated from the simulation results matches well with the experiments. The fracture energy from the experiments is 52.3 ± 3.5 N/mm. The fracture energy from the simulations is 54.6 ± 6.5 N/mm. The difference is only 4.3%. Based on the presented curve, we can predict the size effect of the DFC coupons with similar meso-structures.

7.3 Discussion

7.3.1 Failure mechanisms of DFCs

After calibrating the model, we observe the failure mechanisms of DFCs layer by layer. First, the model captures the notch insensitivity of the smaller specimens frequently observed during the experiments [29,30]. As shown in Fig. 7.4 (a) and (b), the model has a matching final failure location of the 20 mm width specimen. In Fig. 7.4 (b), the matrix damage is shown using the colorbar representing 0 as no damage and 1.0 as fully damaged element. At some layers, such as layer 16, the damaged elements are along with the final failure location. But at the layer 1 and 4, the damage is also accumulated near the notch tip. However, even if the damage is localized at the notch tip followed by the linear elastic fracture mechanics, DFCs can fracture away from the notch due to poorly oriented platelets or resin pockets. Using the computational model, we can easily capture this unique behavior of DFCs.

To fully understand the damage mechanisms in a different scale, we use a JEOL JSM-

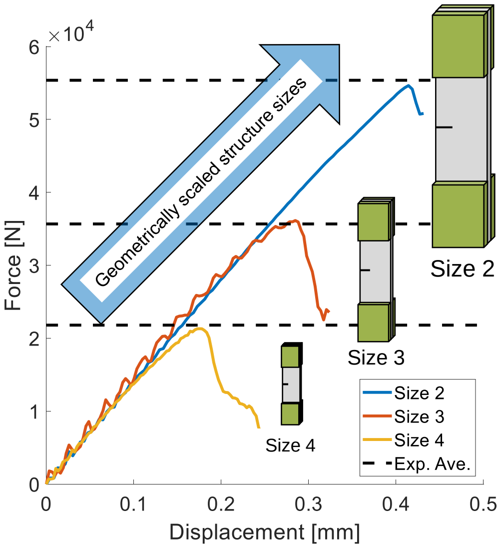

Figure 7.2: The load and displacement curves of three different structure sizes. The average experimental results are plotted in the dashed lines. The stochastic finite element models precisely capture the size effect of geometrically-scaled DFC coupons.

7000F field emission Scanning Electron Microscope (SEM) to observe the fractured regions of DFCs. In Fig. 7.5, multiple damage mechanisms are present. As Fig. 7.5a shows, fiber breakage, platelet splitting, inter-platelet delamination are the most frequently observed failures. In Fig. 7.5b, we can clearly observe the matrix cracking contributing to the fracture. Such complex damage mechanisms lead to a high fracture energy in DFCs [29, 30] compare to the continuous fiber composites.

A key advantage of the computational model presented in this work is that, since we model the interactions between platelets explicitly, we can study the individual damage mechanisms and understand the evolution of each damage accumulation in-situ with the loading conditions. In this study, we consider three main failure mechanisms of DFCs. They are fiber failure in tension, matrix failure in tension, and out-of-plane delamination. Damage due to shear and compression also play important roles [70] but they are not considered here. Each damage can lead to final failure depending on the meso-structure. To study

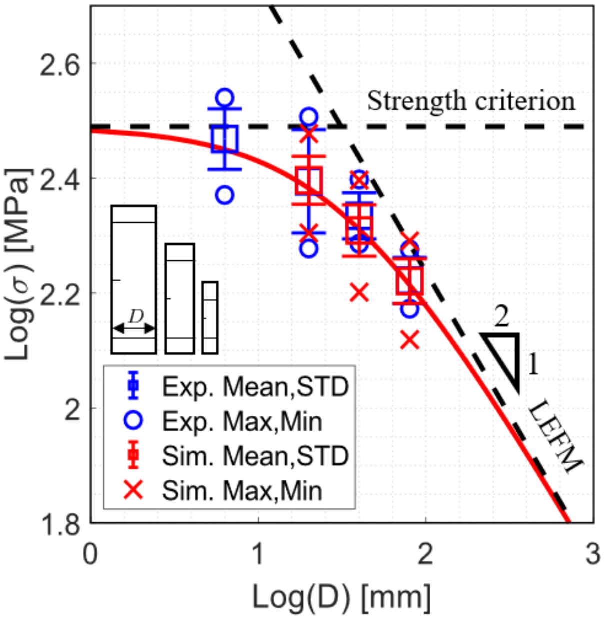

Figure 7.3: Experimental and simulation results of the geometrically-scaled coupons in log-log scale. The simulations precisely follow the non-linear size effect trend of the experimental results. Both the average and the standard deviation match well, meaning that the simulation captures the stochastic fracture behaviors of DFCs well.

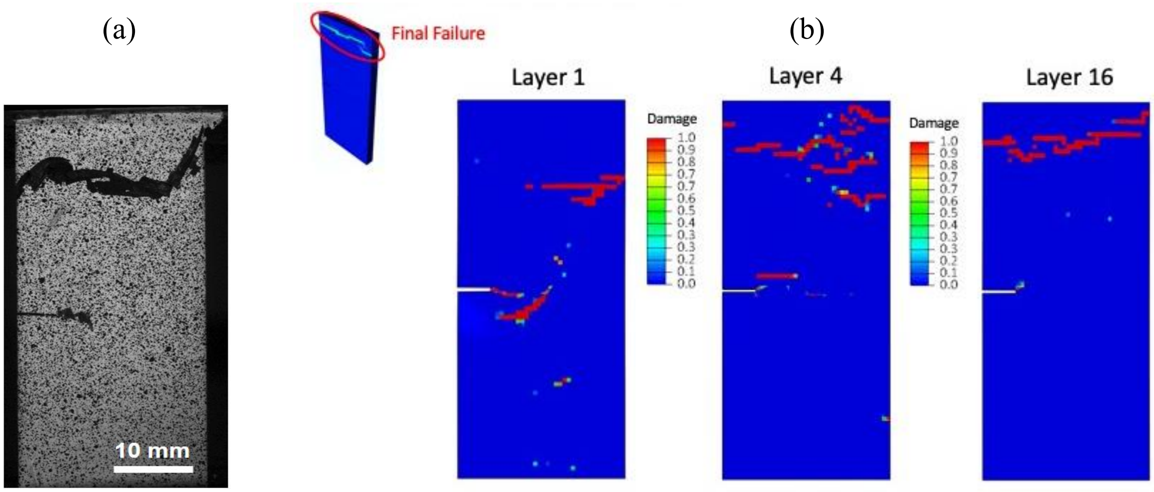

Figure 7.4: Comparison of the notch insensitive fracture between the (a) experiment and (b) simulation results. Frequent notch insensitive fractures happen in the tested DFC coupons. The simulation results also capture the notch insensitive fracture behavior similar to the experiment. Through the thickness, we observe the damage localized at the notch tip but could also happen away from the notch at the same time. Eventually, the fracture propagates at the location where the dominant damage localization happens through the thickness.

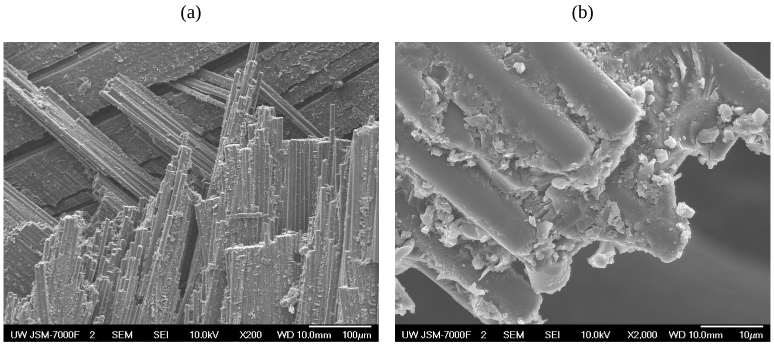

Figure 7.5: Scanning electron microscope images of the fractured DFC coupon. (a) Wide spread delamination and matrix damages are observed. (b) The tip of fiber is enlarged to observe the fiber damage. We can observe almost all kinds of the composite damage mechanisms in DFC coupons.

the evolution of these failures, we synchronize the load-displacement curve with the damage indices over the structure. The index starts from 0 to 1 meaning no damage to fully damaged elements. We obtain the damage in every element from every layer, then combine into a 2D image without averaging them. We distinguish the individual damages using different colors, black for the delamination, blue for the matrix damage, and red for the fiber damage.

In Fig. 7.6, a small specimen size of 44.5 × 20 mm is plotted. Figure 7.6b, c, and d represents a sequence of the damage evolution with respect to the displacement. In a linear region shown in Fig. 7.6b, a small amount of in-plane damages is accumulated near the notch tip (showing in red and blue). There is widespread delamination damage across the structure, but it does not lead to a critical fracture. When the structure reaches the peak as it shown in Fig. 7.6c, a large matrix damage is formed starting from the notch tip. Eventually, the structure fails with the fiber failure starting at the notch tip.

In Fig. 7.7, there is a distinct trend of damage localizations near the notch tip. Similar to the small specimen, a widespread delamination is developed first. At the peak load, fiber damage is accumulated heavily near the notch tip and propagate perpendicular to the loading direction (direction in Y). This is a different fracture phenomenon compared to the small size coupon, where it shows more of widespread damage by the matrix direction. We separate the intra-, and inter-laminar damages and plotted in Fig. 7.8. Also, insignificant level of damages are removed to see the concentration of the damages. As can be noted, at the failure, we notice dominant failure mode is the matrix failure concentrated at the notch tip. The delamination contributes second, and the fiber damage contributes at least. After the failure, the crack propagates and we observe fiber and delamination take the leads. Therefore, the abundant fiber damages observed in Fig. 7.5 is due to the post failure phenomenon. We also expand the analysis into 3D view. Figure 7.9 plots the damages of size 2 and 4 coupons in 3D. These are taken at the maximum stress. We could easily observe wide spreading damages across the body in coupon size 4 (see Fig. 7.9a). Through thickness damages are present regardless of the damage type. At the bigger size coupon, concentrations of the damages at the notch tip are observed.

These observations are important because they provide qualitative data, indicating that as the structure size increases, the structure fails in more brittle manner. Therefore, we can apply the linear elastic fracture mechanism where the pre-existing notch is the strongest source of the fracture. This change in fracture behavior matches well with the size effect curve in Fig. 7.3 where the larger size specimen follows the linear slope of the LEFM curve. This is an important aspect to capture when studying the strong quasibrittle material such as DFCs. As shown in the previous study [30], DFCs contain a significantly larger area of fracture process zone (FPZ) compared to the continuous fiber composites. The tested results show that for the DFCs with the platelet size of 75 × 12 mm, the size of effective FPZ can be larger than the quasi-isotropic layup in an order of magnitude. Therefore, the correct computational model should capture the effect of FPZ size by matching the size effect.

7.3.2 Prediction of the size effect law

The proposed stochastic finite element model is calibrated using the platelet size of 50 × 8 mm and thickness of 4.1 mm. If the model correctly represents the necessary details of the

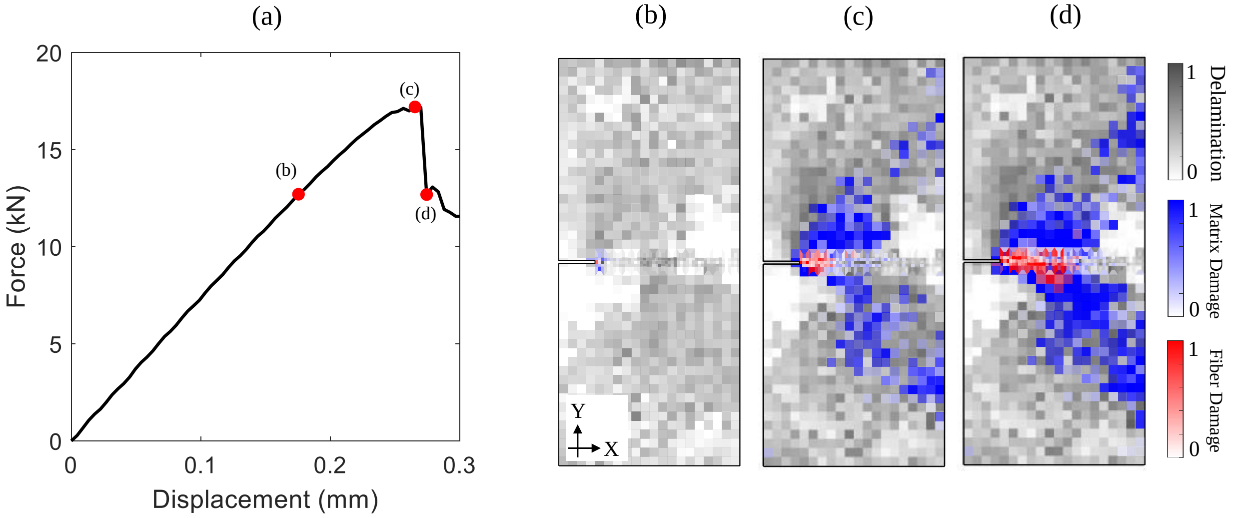

Figure 7.6: Simulation result of a DFC coupon with a width of 20 mm. The damage starts to accumulate around 80% of the maximum load. Starting at the notch tip, the matrix and delamination damage spread across the entire body of the coupon. The fiber damage contributes least to the final failure of the coupon.

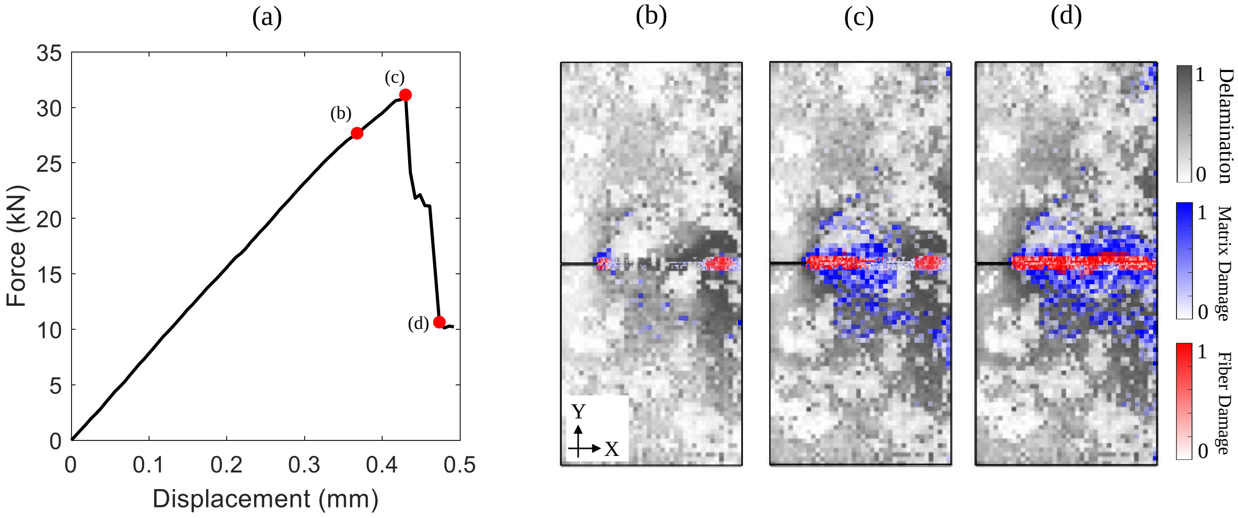

Figure 7.7: Simulation result of a DFC coupon with a width of 80 mm. The damage starts to accumulate around 90% of the maximum load. Similar to the small coupon size, the damage starts to accumulate at the notch tip. However, we can observe that the damages are more concentrated at the notch tip and across through the width not the entire body region. The fiber damage contribute larger portion of the final failure compare to the smaller coupon size.

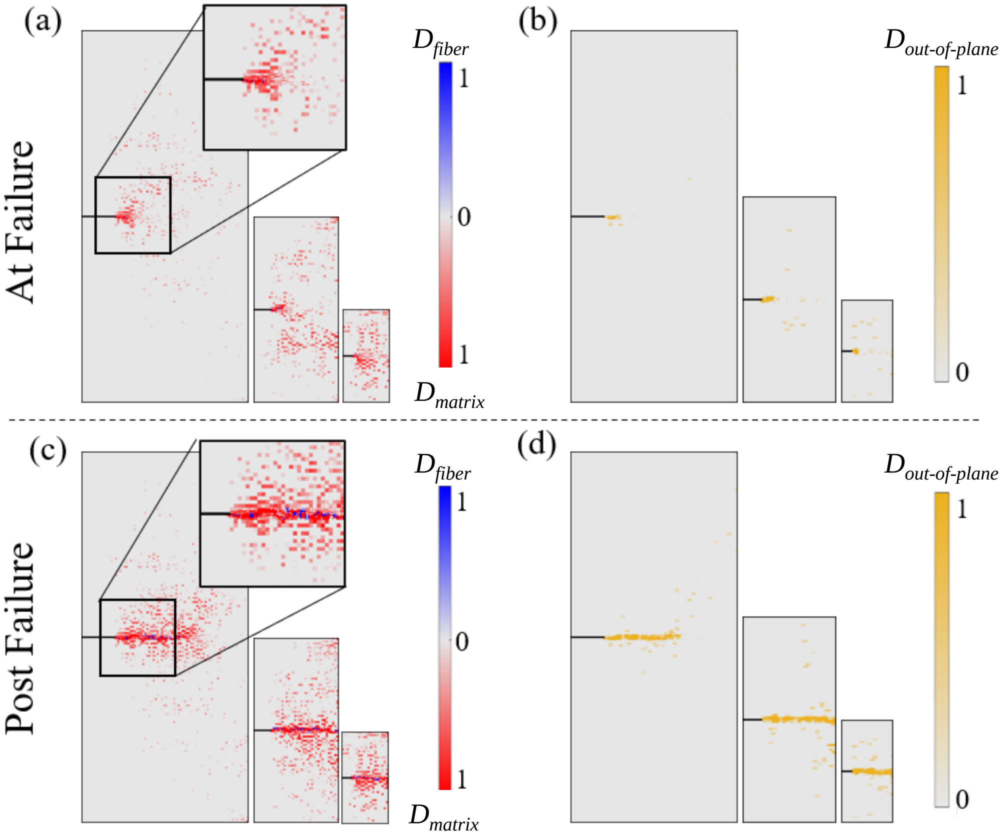

Figure 7.8: Separation of intra-, and inter-laminar damages (a) at the failure, and (b) after the failure of 80 mm width coupon. The matrix damage triggers the failure of DFC coupon whereas, the post failure is dominated by the fiber and delamination damages.

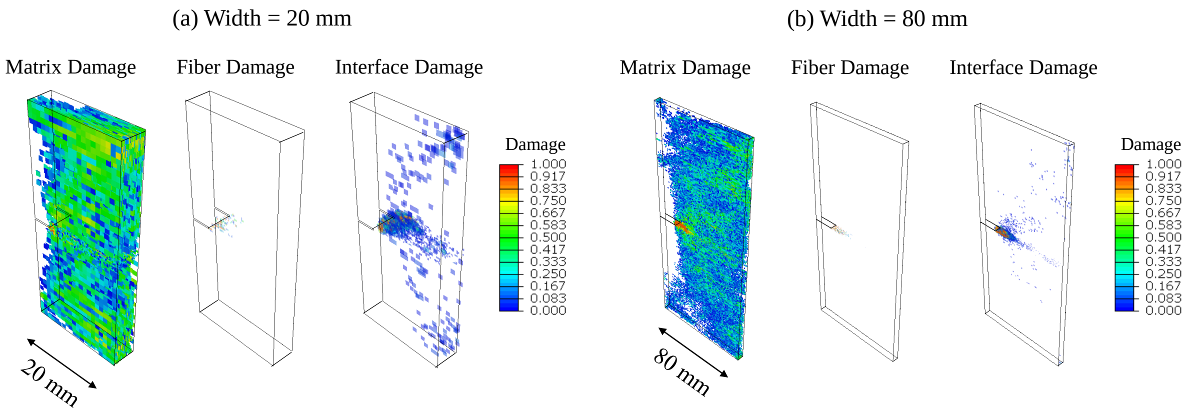

Figure 7.9: 3D visualization of the damage mechanisms. Similar with 2D damage plots, the smaller coupon has wider damage accumulation across the entire body. In 3D view, we can identify the through the thickness damage accumulated at the notch tip.

meso-structures, it should capture the size effect of the different platelet sizes with thickness. Also, it should be able to do it without recalibration of the material properties. To confirm, we create meso-structures with the platelet size of 50 × 8 mm and thickness of 3.3 and 2.2 mm. The calibrated material properties remain unchanged. The meso-structures are transferred to the FE models. The results are plotted along with the experimental data from [29, 30] in Fig. 7.10. The size effect curve from the numerical simulations matches well with the trend of the experimental data at the thickness of 3.3 mm. This shows that the model captures the fracturing behaviors of the different thickness without adjusting the input material properties. With the stochastic FE model, we can find the associated strength and moreover, estimate the fracture energy of a given platelet size and thickness without running the size effect experiments.

However, at the thickness of 2.2 mm, the simulation results overestimate the strengths and the fracture energy. As the structure size increases, the difference gets bigger. This discrepancies may coming from two reasons. First, as the coupon thickness decreases, the platelet orientation distribution plays more significant role. As a result, the variation associated with the strength and the fracture energy increase. For instance, the fracture energy coefficient of variation at 4.1 mm thickness is 11% whereas at 2.2 mm is 23%. Because the meso-structure is not fully calibrated to capture the stochastic distribution of the platelets, the overall strength overestimates the fracture energy. Second is related with the damage softening law of the platelet layers. A simple schematic of the softening curve is plotted in Fig. 7.11. Currently, we are using the linear softening law where the damage follows linear, straight line from the peak stress down to zero. In case of the quasi-brittle material, the shape of the softening curve plays a significant role. The parameters which determine the fracture of the material are the stiffness, strength, fracture energy, and the shape of the softening curve (see Fig. 7.11). We assume that the fracture of DFCs happen when the fracture process zone (FPZ) is fully developed. When the FPZ is fully developed, the material fails when they fully released their fracture energy (see Fig. 7.11b). In this case, the shape of the softening curve does not play a role. However, when the FPZ is not fully developed at the failure (see Fig. 7.11a), the energy released by the material is not at the critical point but smaller than the fracture energy. In this case, the shape of the softening curve plays a significant role. When the linear and bilinear softening curve have equal amount of the fracture energy (area under the curve), then the failure strength is different depending on the shape of the curve.

To confirm the effect of the fracture energy, we compare the size effect curves generated by the fracture energy from 60 and 30 N/mm. In Fig. 7.12, we simulate the same thickness of 2.2 mm with two different fracture energies. A linear softening curve is used. As can be noted, the overall strength estimation improve significantly by simply reducing the fracture energy. This observation provides an evidence indicating that for the thin coupons, the fracture process zone is most likely not fully developed. Therefore, we need to consider the shape of the softening curve in order to match the scaling effect of the DFC structures.

7.4 Conclusion

We introduce the computational stochastic finite element model that utilizes a random platelet generation algorithm to simulate the complex material meso-structure. Using the

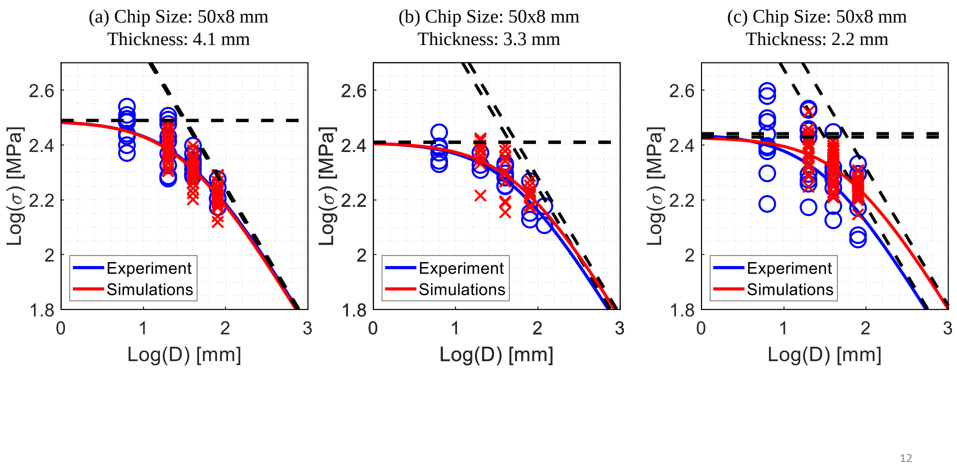
(a) Chip Size: 50x8 mm
Thickness: 4.1 mm

(b) Chip Size: 50x8 mm
Thickness: 3.3 mm

(c) Chip Size: 50x8 mm
Thickness: 2.2 mm

Figure 7.10: Size effect curves of different coupon thicknesses using the material properties calibrated at (a) the thickness of 4.1 mm. (b) At the thickness of 3.3 mm, the simulation precisely captures the non-linear size effect of the experiment. (c) At the thickness of 2.2 mm, the simulation results overestimate the fracture energy significantly. Two possible sources of such discrepancies are (1) increased platelet stochastic distributions, and (2) the shape of the softening law. A further investigation is required to fully capture the scaling effect of DFCs with different thicknesses.

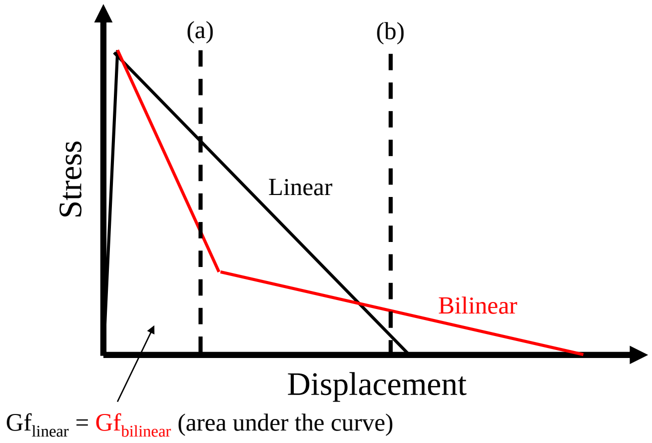

Figure 7.11: A linear and bilinear damage softening curves with equal fracture energy, Gf. When the failure happens at the point (a), the shape of the damage softening curve is important. This is the case when the FPZ is not fully developed. When the failure happens at the point (b), the shape of the curve is not important. This is the case when the FPZ is fully developed.

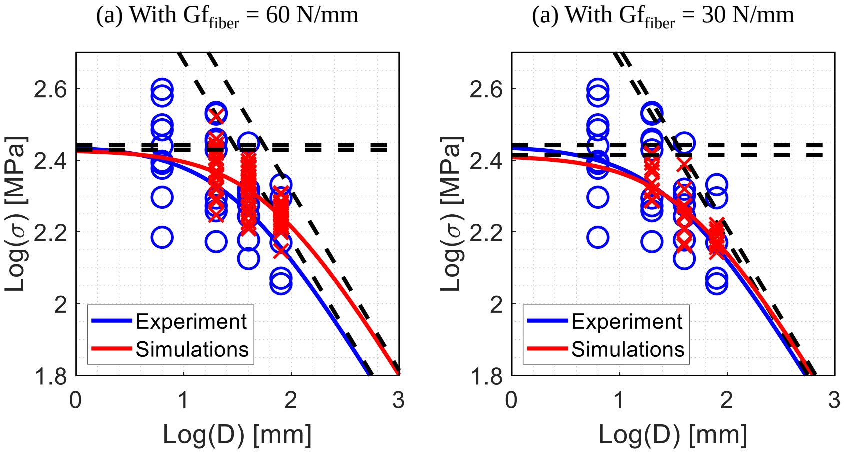

Figure 7.12: The size effect curves of DFC coupons with 50×8 mm platelets and 2.1 mm. Two different longitudinal fracture energies are used: (a) 60 N/mm and (b) 30 N/mm. Using 60 N/mm, the simulation results capture the size effect of thicker coupons but they overestimate the strength at 2.2 mm coupon. (b) By reducing the fracture energy, the size effect is well captured. This indicates that for the thinner DFC coupons, the shape of the softening law plays a significant role. We need further investigation to find the proper softening shape to capture the size effect of different thicknesses.

model, we study the fracturing behaviors of the discontinuous fiber composites with three main failure mechanisms: fiber tension, matrix tension, and out-of-plane delamination. The model presents in-situ, unique damage evolution of the DFC structures. The small-size structure shows a widespread matrix failure at the peak load whereas the larger-size structure has more localized damage accumulated near the notch end. These observations support the strong size effect of DFCs where the effective fracture process zone plays a significant role in the failure mechanisms. The implemented model provides the predictions of strength for the different meso-structures without recalibrating the material properties. This will bring a significant reduction of the experimental cost to validate the material properties and will help engineers to choose the optimized platelet morphology for their DFC structures.

Chapter 8

CONCLUSIONS AND FUTURE WORKS

8.1 Conclusions

In this study, we investigated the quasi-static, uni-axial tensile mechanical properties of discontinuous fiber composite (DFC) structures. The DFC structures were divided into two groups, (1) without a notch, and (2) with a notch. We studied their mechanical responses using experimental investigations and numerical analysis. Based on the results, we have the following conclusions:

1. We experimentally investigated two meso-structure characteristics (the coupon thickness and platelet width). We tested a large population of samples (30 coupons per type) in order to have statistically significant data. We found that the statistical distribution of the modulus data followed the normal and the strength data followed the Weibull distribution. Based on the experimental results, we observed strong thickness effect in both the narrow and square platelets. The tensile modulus and strength increased as the thickness increased. The thickness effect was stronger in the tensile strength than the modulus. The thickness effect also amplified as the thickness decreased. The platelet width effect was also significant. As the platelet width increased, the strength and modulus decreased. Not only the average of the strength and modulus had the thickness and platelet width effect, the variation also changed with respect to the meso-structures. As the thickness and the platelet width increased, the variation decreased. Thanks to the large number of tested samples, we could confidently calculated the B-basis design values. These results can be directly used by engineers and designers who want to use DFC structures in their engineering applications. We describe the unnotched tensile experimental investigation in Chapter 3.

2. We developed stochastic finite element framework to predict and understand the mechanical behaviors of DFCs. The random platelet meso-structure generation algorithm was proposed to mimic the manufacturing process. The algorithm explicitly generates the platelets following the designed probability distribution. The algorithm is capable of matching the spatial variation of platelet distributions. It allows the meso-structure to be fully calibrated against the experimental data. The finite element models used the calibrated meso-structures as inputs, matched the experimental thickness and platelet width effect. The FE model predicted that the thickness effect diminished after the thickness of 0.25" (45 layers through thickness). The computational models precisely captured both the average and associated variations in the modulus and the strength. The numerical analysis of the meso-structures allows the users to safely predict the B-basis design values which could potentially reduce a significant amount of the physical testing. Using this computational tools, we expect to expedite the certification process of DFC structures. The modeling process is described in Chapter 4.

3. We experimentally investigated mode I intra-laminar fracture of DFC structures. Three platelet sizes (75×12, 50×8, and 25×4 mm) and four coupon thicknesses (4.1, 3.3, 2.2, 1.1 mm) were tested. For the platelet size study, the coupon thickness was kept at 3.3 mm. For the coupon thickness study, the 50×8 mm platelet size was used. We tested single edge notch tension (SENT) coupons. Also, not just a single size of a coupon was tested but wide range of geometrically-scaled coupons were tested to accommodate the quasi-brittle material characteristic of DFCs. For the first time in the literature, we found the mode I intra-laminar fracture energy of DFCs. The experimental results showed that depending on the platelet size and the coupon thickness, the fracture energy varies. The platelet size has a positive, linear relationship with the fracture energy when the aspect ratio is fixed. The fracture energy also increases as the coupon thickness increases but reach the asymptotic limit after the thickness of 4.1 mm. The fracture energy of DFCs is $3 \sim 6$ times larger than the aluminum 5083. Also, it can

be 1.6 times larger than the quasi-isotropic laminate made of identical prepregs. These findings expand the applications of DFCs because they have higher tolerant to the crack propagation than the quasi-isotropic laminate. DFCs not only have the advantage in flexible manufacturing capability but also in their material performance on crack resistance. The experimental investigations are described in Chapter 5 and 6.

4. We applied the stochastic finite element framework to study the fracture behaviors of the notched DFC structures. With proper calibrations of the platelet and interface material properties, we successfully matched the non-linear scaling of the notched coupons. We identified the major and minor damage mechanisms of DFCs. The matrix and delamination damages were the dominant factors whereas the fiber breakage was the minor cause. The model also matched the size effects of different coupon thickness, showing the capability of predicting the different meso-structures. However, a further improvement is needed to match the results from the thickness of 2.2 mm or below. Leveraging this computational tools, we can predict the failure strength of different geometries with mode I intra-laminar loading condition without physically test them.

Overall, we experimentally investigated and numerically analyzed the mechanical behaviors of DFCs. We built extensive amount of experimental data to understand the statistical distribution of the material properties. We created the computational tools to predict the mechanical responses of DFCs. Having such tools will expand the applications of DFCs. They can minimize the unnecessary and costly physical tests. Engineers and designers can utilize these tools to build parts based on predictable mechanical performances. This study provides comprehensive engineering approach on how to characterize DFC materials.

8.2 Future Works

In the foregoing chapters, we discussed the experimental and numerical investigations of the DFC structures with and without a notch. Despite the comprehensive analysis were conducted, there are many aspects of DFCs that still need to be investigated. The following lists are the summary of future works:

1. We learned that the local platelet distribution determines the statistical variation of the tensile modulus and strength. Therefore, matching the local platelet distribution is the key to predict the material properties of DFCs. The local platelet distribution can be obtained by indirectly calibrating the meso-structures using the large amount of experimental data or directly from the X-ray µCT scans. We also need a proper size of the statistical representative volume element (SRVE). However, currently we are lack of analytical method to find the proper size of SRVE. If we can obtain the proper size of SRVE, and combined with the local platelet orientation distribution from CT scans, we can fully characterize the statistical variation of material properties without physically test the DFC coupons.

2. So far, we mainly focused on 2D flat coupons. However, DFC structures often contain 3D complex contours with significant out-of-plane deformation. Studying the 2D flat coupons provides significant insights on analyzing the 3D contours. But, 3D contours definitely require additional works. Many studies analyzed the mechanical behaviors of 3D DFC structures [10, 59, 60]. Most of them adapted the orientation tensors directly from X-ray µCT scans and analyzed the structures using finite element models. Favaloro *et al.* [122] explicitly modeled the platelet flow to determine the platelet distribution. However, this method required extensive computational cost. We must find the efficient yet accurate method to analyze complex 3D structures.

3. When the DFC structures contain notches and cracks, the softening shape of the damage evolution law may play an important role as mentioned in Chapter 7. In this case, especially when the fracture process zone is not fully developed, a bilinear or other softening shape is more suitable to capture the failure of DFCs. We are currently developing the bilinear damage evolution with the Hashin failure criteria. We will integrate the damage models in the future to capture the fracturing behaviors of the notched DFCs.

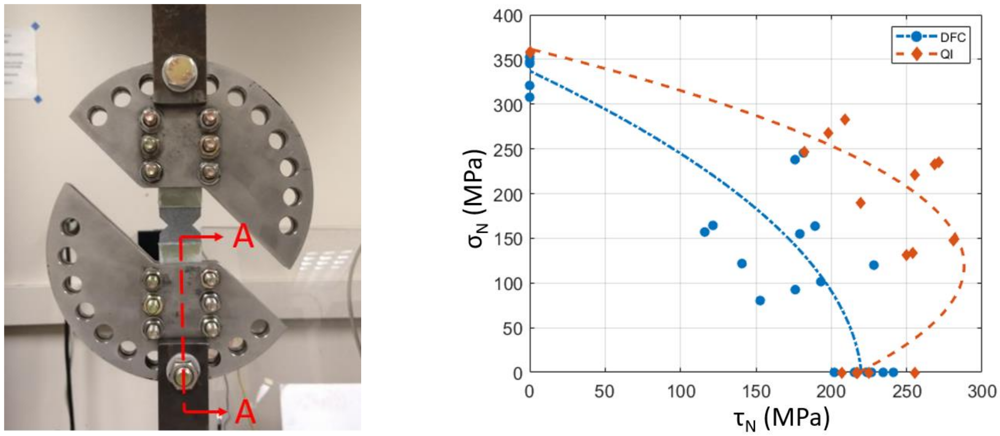

(a)

(b)

Figure 8.1: DFC double v-notch coupons under the Arcan fixture [48]. The Arcan fixture couples the axial and shear loading ratio using the pins. The test swept the pins' locations from the pure tension to pure shear. The experimental results are shown in (b). This is the multi-axial responses of DFCs reported for the first time in the literature.

4. In many applications, DFC structures are used as joints, connecting multiple parts together. In this case, DFCs often experience multi-axial loading condition. At the University of Washington, we have experimentally and numerically investigated the mechanical responses of DFCs under the multi-axial loading. Nguyen [48] reported this study in detail. In summary, We used the Arcan fixture shown in Fig. 8.1a. Using the Arcan fixture, we tested double V-notch DFC coupons under tension and shear coupling. The experimental results are plotted in Fig. 8.1b. For the first time in the literature, the multi-axial fracturing behaviors of DFCs are reported. We are planning on to calibrate the stochastic finite element models to capture the unique behaviors and furthermore predict the responses of different DFC meso-structures.

5. Besides mode I intra-laminar fracture, we also have investigated mode I inter-laminar

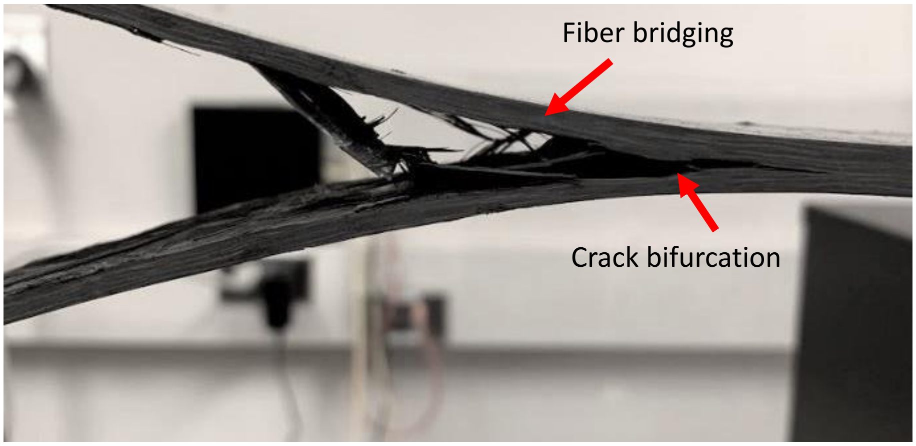

Figure 8.2: Fracture surfaces of double cantilever beam (DCB) test reported by Tidwell [49]. DFCs under the out-of-plane loading experience far more complex damage modes than the continuous fiber composites.

fracture using the double cantilever beam tests. The experimental results are reported by Tidwell [49] in details. Because of the random platelet orientation, the fracture surfaces are far more chaotic than the continuous fiber composites (see Fig. 8.2). In some coupons, crack bifurcation occurred showing two crack fronts from a single crack tip. As a result, the fracture energy for DFCs is 80 $\sim$ 167% higher than the reported values for continuous fiber composites [49]. However, in order to fully characterize the fracture energy, we still need to study the scaling effect in this failure mode. Computational modeling is needed to fully understand the fracturing behaviors of this material.

BIBLIOGRAPHY

[1] Barbero EJ. *Introduction to Composite Materials Design.* CNC Press, 2017.

[2] D Gay, SV Hoa, and SW Tsai. *Composite Materials: Design and Applications.* CRC Press, 2014.

[3] A Elmarakbi. *Advanced Composite Materials for Automotive Applications: Structural Integrity and Crashworthiness.* Wiley, 2013.

[4] DI Chortis. *Structural Analysis of Composite Wind Turbine Blades.* Springer, 2013.

[5] A Baker, S Dutton, and D Kelly. *Composite Materials for Aircraft Structures.* American Institute of Aeronautics and Astronautics, 2004.

[6] Boeing 787 Dreamliner. Online; 2021. https://www.boeing.com/commercial/787/.

[7] A Rashidi and AS Milani. A multi-step biaxial bias extension test for wrinkling/de-wrinkling characterization of woven fabrics: Towards optimum forming design guidelines. *Materials & Design*, 146:273–285, 2018.

[8] P Wang, X Legrand, P Boisse, N Hamila, and D Soulat. Experimental and numerical analyses of manufacturing process of a composite square box part: Comparison between textile reinforcement forming and surface 3d weaving. *Composites Part B: Engineering*, 78:26–34, 2015.

[9] M Selezneva and L Lessard. Characterization of mechanical properties of randomly oriented strand thermoplastic composites. *Journal of composite materials*, 50(20):2833–2851, 2016.

[10] BR Denos, DE Sommer, AJ Favaloro, RB Pipes, and WB Avery. Fiber orientation measurement from mesoscale ct scans of prepreg platelet molded composites. *Composites Part A: Applied Science and Manufacturing*, 114:241–249, 2018.

[11] BC Jin, X Li, A Jain, C González, J LLorca, and S Nutt. Optimization of microstructures and mechanical properties of composite oriented strand board from reused prepreg. *Composite Structures*, 174:389–398, 2017.

[12] Y Li, S Pimenta, J Singgih, S Nothdurfter, and K Schuffenhauer. Experimental investigation of randomly-oriented tow-based discontinuous composites and their equivalent laminates. *Composites Part A: Applied Science and Manufacturing*, 102:64–75, 2017.

[13] Y Wan and J Takahashi. Tensile and compressive properties of chopped carbon fiber tapes reinforced thermoplastics with different fiber lengths and molding pressures. *Composites Part A: Applied Science and Manufacturing*, 87:271–281, 2016.

[14] Z Chen, T Huang, Y Shao, Y Li, H Xu, K Avery, D Zeng, W Chen, and X Su. Multiscale finite element modeling of sheet molding compound (smc) composite structure based on stochastic mesostructure reconstruction. *Composite Structures*, 188:25–38, 2018.

[15] J Ryatt and M Ramulu. Prediction of tensile failure of stochastic tow-based discontinuous composites via mesoscale finite element analysis. *Composite Structures*, 279:114769, 2022.

[16] S Mortazavian and A Fatemi. Fatigue behavior and modeling of short fiber reinforced polymer composites: A literature review. *International Journal of Fatigue*, 70:297–321, 2015.

[17] B Boursier. New possibilities with hexmc, a high performance moulding compound. *SAMPE European conference*, 2001.

[18] J Aubry. Hexmc—bridging the gap between prepreg and smc. *Reinforced Plastics*, 45(6):38–40, 2001.

[19] SB Visweswaraiah, M Selezneva, L Lessard, and P Hubert. Mechanical characterisation and modelling of randomly oriented strand architecture and their hybrids–a general review. *Journal of Reinforced Plastics and Composites*, 37(8):548–580, 2018.

[20] Greene Tweed. Lansdale. PA. https://www.gtweed.com/.

[21] Hexcel, Stamford, CT. https://www.hexcel.com/Products/HexMC-Materials-for-Industries.

[22] P Feraboli, E Peitso, F Deleo, T Cleveland, and PB Stickler. Characterization of prepreg-based discontinuous carbon fiber/epoxy systems. *Journal of reinforced plastics and composites*, 28(10):1191–1214, 2009.

[23] SG Kravchenko, DE Sommer, BR Denos, AJ Favaloro, CM Tow, WB Avery, and B Pipes. Tensile properties of a stochastic prepreg platelet molded composite. *Composites Part A: Applied Science and Manufacturing*, 124:105507, 2019.

[24] SG Kravchenko, DE Sommer, BR Denos, WB Avery, and B Pipes. Structure-property relationship for a prepreg platelet molded composite with engineered meso-morphology. *Composite Structures*, 210:430–445, 2019.

[25] DE Sommer, SG Kravchenko, BR Denos, AJ Favaloro, and RB Pipes. Integrative analysis for prediction of process-induced, orientation-dependent tensile properties in a stochastic prepreg platelet molded composite. *Composites Part A: Applied Science and Manufacturing*, 130:105759, 2020.

[26] H Tang, Z Chen, G Zhou, Y Li, K Avery, H Guo, H Kang, D Zeng, and X Su. Correlation between failure and local material property in chopped carbon fiber chip-reinforced sheet molding compound composites under tensile load. *Polymer Composites*, 40(S2):E962–E974, 2019.

[27] Z Chen, H Tang, Y Shao, Q Sun, G Zhou, Y Li, H Xu, D Zeng, and X Su. Failure of chopped carbon fiber sheet molding compound (smc) composites under uniaxial tensile loading: Computational prediction and experimental analysis. *Composites Part A: Applied Science and Manufacturing*, 118:117–130, 2019.

[28] M Alves, D Carlstedt, F Ohlsson, LE Asp, and S Pimenta. Ultra-strong and stiff randomly-oriented discontinuous composites: Closing the gap to quasi-isotropic continuous-fibre laminates. *Composites Part A: Applied Science and Manufacturing*, 132:105826, 2020.

[29] S Ko, J Yang, ME Tuttle, and M Salviato. Effect of the platelet size on the fracturing behavior and size effect of discontinuous fiber composite structures. *Composite Structures*, 227:111245, 2019.

[30] S Ko, J Davey, S Douglass, J Yang, ME Tuttle, and M Salviato. Effect of the thickness on the fracturing behavior of discontinuous fiber composite structures. *Composites Part A: Applied Science and Manufacturing*, 125:105520, 2019.

[31] S Ko, K Chan, R Hawkins, R Jayaram, C Lynch, R El Mamoune, M Nguyen, N Pekhotin, N Stokes, D Wu, J Yang, ME Tuttle, and M Salviato. Experimental and numerical characterization of the intra-laminar fracturing behavior in discontinuous fiber composite structures. In *Proceedings of the 33th ASC Conference, Seattle, WA, USA*, pages 24–26, 2018.

[32] S Ko, K Chan, R Hawkins, R Jayaram, C Lynch, R El Mamoune, M Nguyen, N Pekhotin, N Stokes, D Wu, J Yang, ME Tuttle, and M Salviato. Characterization and computational modeling of the fracturing behavior in discontinuous fiber composite structures. In *SAMPE Conference. Long Beach, CA.*, 2018.

[33] ZP Bažant. Size effect in blunt fracture: concrete, rock, metal. *Journal of engineering mechanics*, 110(4):518–535, 1984.

[34] ZP Bažant and MT Kazemi. Determination of fracture energy, process zone length and brittleness number from size effect, with application to rock and conerete. *International Journal of fracture*, 44(2):111–131, 1990.

[35] ZP Bažant, IM Daniel, and Z Li. Size effect and fracture characteristics of composite laminates. *J Eng Mater Technol*, 118(3):317–324, 1996.

[36] ZP Bažant and J Planas. *Fracture and size effect in concrete and other quasibrittle materials*. CNC Press, 1998.

[37] M Salviato, K Kirane, SE Ashari, ZP Bažant, and G Cusatis. Experimental and numerical investigation of intra-laminar energy dissipation and size effect in two-dimensional textile composites. *Composites Science and Technology*, 135:67–75, 2016.

[38] CH Mefford, Y Qiao, and M Salviato. Failure behavior and scaling of graphene nanocomposites. *Composite Structures*, 176:961–972, 2017.

[39] Y Qiao and M Salviato. Study of the fracturing behavior of thermoset polymer nanocomposites via cohesive zone modeling. *Composite Structures*, 220:127–147, 2019.

[40] Y Qiao and M Salviato. Strength and cohesive behavior of thermoset polymers at the microscale: A size-effect study. *Engineering Fracture Mechanics*, 213:100–117, 2019.

[41] W Li, Z Jin, and G Cusatis. Size effect analysis for the characterization of marcellus shale quasi-brittle fracture properties. *Rock Mechanics and Rock Engineering*, 52(1):1–18, 2019.

[42] M Salviato, VT Chau, W Li, ZP Bažant, and G Cusatis. Direct testing of gradual postpeak softening of fracture specimens of fiber composites stabilized by enhanced grip stiffness and mass. *Journal of Applied Mechanics*, 83(11), 2016.

[43] M Salviato, M Zappalorto, and M Quaresimin. The effect of surface stresses on the critical debonding stress around nanoparticles. *International journal of fracture*, 172(1):97–103, 2011.

[44] M Salviato, M Zappalorto, and M Quaresimin. Nanoparticle debonding strength: a comprehensive study on interfacial effects. *International Journal of Solids and Structures*, 50(20-21):3225–3232, 2013.

[45] M Salviato, K Kirane, ZP Bažant, and G Cusatis. Mode i and ii interlaminar fracture in laminated composites: a size effect study. *Journal of Applied Mechanics*, 86(9), 2019.

[46] Weixin Li, Yao Qiao, Joel Fenner, Kyle Warren, Marco Salviato, Zdeněk P Bažant, and Gianluca Cusatis. Elastic and fracture behavior of three-dimensional ply-to-ply angle interlock woven composites: Through-thickness, size effect, and multiaxial tests. *Composites Part C: Open Access*, 4:100098, 2021.

[47] Sekisui aerospace corporation, Renton, WA. https://www.sekisuiaerospace.com/.

[48] M Nguyen. *Experimental and Numerical Investigation of the Mechanical Behavior of Discontinuous Fiber Composite Structures Under Multi-Axial Loading.* University of Washington, 2020.

[49] Kathryn Tidwell. *Investigating the Fracture Behavior and Damage Mechanisms of Discontinuous Fiber Composites Under Significant Out-of-plane Loading.* University of Washington, 2020.

[50] P Feraboli, E Peitso, T Cleveland, and PB Stickler. Modulus measurement for prepreg-based discontinuous carbon fiber/epoxy systems. *Journal of composite materials*, 43(19):1947–1965, 2009.

[51] ZP Bažant, J Le, and M Salviato. *Quasibrittle Fracture Mechanics and Size Effect. A First Course.* Oxford University Press, 2021.

[52] ZP Bažant. Probability distribution of energetic-statistical size effect in quasibrittle fracture. *Probabilistic engineering mechanics*, 19(4):307–319, 2004.

[53] ZP Bažant and J Le. *robabilistic Mechanics of Quasibrittle Structures: Strength, Lifetime, and Size Effect.* Cambridge University Press, 2017.

[54] Y Qiao and M Salviato. Micro-computed tomography analysis of damage in notched composite laminates under multi-axial fatigue. *Composites Part B: Engineering*, 187:107789, 2020.

[55] Y Wan, I Straumit, J Takahashi, and SV Lomov. Micro-ct analysis of internal geometry of chopped carbon fiber tapes reinforced thermoplastics. *Composites Part A: Applied Science and Manufacturing*, 91:211–221, 2016.

[56] Y Wan, I Straumit, J Takahashi, and SV Lomov. Micro-ct analysis of the orientation unevenness in randomly chopped strand composites in relation to the strand length. *Composite Structures*, 206:865–875, 2018.

[57] G Cai, T Shirai, Y Wan, K Uzawa, and J Takahashi. Application of x-ray computed tomography to measuring fiber orientation distribution of chopped carbon fiber tape reinforced thermoplastics. *Applied Composite Materials*, 28(2):573–586, 2021.

[58] BR Denos, SG Kravchenko, and RB Pipes. Progressive failure analysis in platelet based composites using ct-measured local microstructure. In *SAMPE Conference*, pages 1421–1435, 2017.

[59] S Kravchenko. *Failure analysis in platelet molded composite systems. PhD Dissertation.* PhD thesis, Purdue University, 2017.

[60] AJ Favaloro, DE Sommer, BR Denos, and RB Pipes. Simulation of prepreg platelet compression molding: Method and orientation validation. *Journal of Rheology*, 62(6):1443–1455, 2018.

[61] LM Martulli, L Muyshondt, M Kerschbaum, S Pimenta, SV Lomov, and Y Swolfs. Carbon fibre sheet moulding compounds with high in-mould flow: Linking morphology to tensile and compressive properties. *Composites Part A: Applied Science and Manufacturing*, 126:105600, 2019.

[62] GOM, Braunschweig, Germany. https://www.gom.com.

[63] WG Cochran. *Sampling Techniques.* New York: John Wiley & Sons, 1977.

[64] Handbook, M. MIL-HDBK-17: Composite materials handbook. Virginia: US Department of Defense, 2002.

[65] P Feraboli, T Cleveland, P Stickler, and JC Halpin. Stochastic laminate analogy for simulating the variability in modulus of discontinuous composite materials. *Composites Part A: Applied Science and Manufacturing*, 41(4):557–570, 2010.

[66] K Harban and ME Tuttle. Reducing certification costs of discontinuous fiber composite structures via stochastic modeling. *U.S. Dept. of Transportation FAA*, 2017.

[67] M Selezneva, S Roy, S Meldrum, L Lessard, and A Yousefpour. Modelling of mechanical properties of randomly oriented strand thermoplastic composites. *Journal of Composite Materials*, 51(6):831–845, 2017.

[68] SZH Shah, RS Choudhry, and S Mahadzir. A new approach for strength and stiffness prediction of discontinuous fibre reinforced composites (dfc). *Composites Part B: Engineering*, 183:107676, 2020.

[69] SB Visweswaraiah, L Lessard, and P Hubert. Interlaminar shear behaviour of hybrid fibre architectures of randomly oriented strands combined with laminate groups. *Composite Structures*, 176:823–832, 2017.

[70] Y Li and S Pimenta. Development and assessment of modelling strategies to predict failure in tow-based discontinuous composites. *Composite Structures*, 209:1005–1021, 2019.

[71] J Henry and S Pimenta. Semi-analytical simulation of aligned discontinuous composites. *Composites Science and Technology*, 144:230–244, 2017.

[72] JC Halpin and NJ Pagano. The laminate approximation for randomly oriented fibrous composites. *Journal of Composite Materials*, 3(4):720–724, 1969.

[73] Dassault Systemes ABAQUS. ABAQUS Documentation, Providence, RI. 2018.

[74] BG Green, MR Wisnom, and SR Hallett. An experimental investigation into the tensile strength scaling of notched composites. *Composites Part A: Applied Science and Manufacturing*, 38(3):867–878, 2007.

[75] Z Hashin. Failure criteria for unidirectional fiber composites. *J Appl Mech*, 47:329–34, 1980.

[76] I Lapczyk and JA Hurtado. Progressive damage modeling in fiber-reinforced materials. *Composites Part A: Applied Science and Manufacturing*, 38(11):2333–2341, 2007.

[77] PP Camanho and CG Dávila. Mixed-mode decohesion finite elements for the simulation of delamination in composite materials. 2002.

[78] ML Benzeggagh and M Kenane. Measurement of mixed-mode delamination fracture toughness of unidirectional glass/epoxy composites with mixed-mode bending apparatus. *Composites science and technology*, 56(4):439–449, 1996.

[79] A Hillerborg, M Modéer, and PE Petersson. Analysis of crack formation and crack growth in concrete by means of fracture mechanics and finite elements. *Cement and concrete research*, 6(6):773–781, 1976.

[80] A Turon, CG Dávila, PP Camanho, and J Costa. An engineering solution for mesh size effects in the simulation of delamination using cohesive zone models. *Engineering fracture mechanics*, 74(10):1665–1682, 2007.

[81] MD McKay, RJ Beckman, and WJ Conover. A comparison of three methods for selecting values of input variables in the analysis of output from a computer code. *Technometrics*, 42(1):55–61, 2000.

[82] W Weibull. A statistical distribution function of wide applicability. *Journal of applied mechanics*, 18(3):293–297, 1951.

[83] S Ko, T Nakagawa, Z Chen, J Davey, T Abdullah, L Kuklenski, E Adams, M Soja, C Park, W Avery, J Yang, and M Salviato. Experimental and numerical investigations of stochastic thickness effects in discontinuous fiber composites. In *American Society of Composites Conference. Virtual*, 2021.

[84] I Amidror. Scattered data interpolation methods for electronic imaging systems: a survey. *Journal of electronic imaging*, 11(2):157–176, 2002.

[85] S Mindess, JF Young, and D Darwin. *Concrete*. Prentice Hall, 2003.

[86] Volume Graphics GMBH, VGStudio MAX 3.0, Heidelberg, 2015.

[87] bR Denos. *Fiber Orientation Measurement in Platelet-Based Composites via Computed Tomography Analysis*. PhD thesis, Purdue University, 2017.

[88] DE Sommer, SG Kravchenko, and RB Pipes. A numerical study of the meso-structure variability in the compaction process of prepreg platelet molded composites. *Composites Part A: Applied Science and Manufacturing*, 138:106010, 2020.

[89] A Ionita and YJ Weitsman. On the mechanical response of randomly reinforced chopped-fibers composites: Data and model. *Composites science and technology*, 66(14):2566–2579, 2006.

[90] S Yamashita, K Hashimoto, H Suganuma, and J Takahashi. Experimental characterization of the tensile failure mode of ultra-thin chopped carbon fiber tape-reinforced thermoplastics. *Journal of Reinforced Plastics and Composites*, 35(18):1342–1352, 2016.

[91] Quantum Composites, Bay City, MI. https://www.quantumcomposites.com/applications/lamborghin

[92] Moore S. SMC adopted for rear door frame of Toyota's new Prius PHV, Plastics Today, 3 April 2017 https://www.plasticstoday.com/automotive-and-mobility/smc-adopted-rear-door-frame-toyota-s-new-prius-phv/163725208056557.

[93] M Turtle, T Shifman, and B Boursier. Simplifying certification of discontinuous composite material forms primary aircraft structures. *Hexcel research and technology*, 2010.

[94] P Feraboli, F Gasco, B Wade, S Maier, R Kwan, W Salmon, A Masini, L DeOto, and ML Reggiani. Forged compositer" technology for the suspension arms of the sesto elemento. In *ASC 26rd Annual technical conference. Montreal*, 2011.

[95] S Black. Military oem makes the switch from sandwich construction to compression molding to optimize composite aerospace part. *High Perf Compos*, 2012.

[96] G Nilakantan and S Nutt. Reuse and upcycling of aerospace prepreg scrap and waste. *Reinforced Plastics*, 59(1):44–51, 2015.

[97] SG Kravchenko, DE Sommer, and RB Pipes. Uniaxial strength of a composite array of overlaid and aligned prepreg platelets. *Composites Part A: Applied Science and Manufacturing*, 109:31–47, 2018.

[98] T Matsuo, M Kan, K Furukawa, T Sumiyama, H Enomoto, and K Sakaguchi. Numerical modeling and analysis for axial compressive crushing of randomly oriented thermoplastic composite tubes based on the out-of-plane damage mechanism. *Composite Structures*, 181:368–378, 2017.

[99] K Johanson, LT Harper, MS Johnson, and NA Warrior. Heterogeneity of discontinuous carbon fibre composites: Damage initiation captured by digital image correlation. *Composites Part A: Applied Science and Manufacturing*, 68:304–312, 2015.

[100] ZP Bažant and L Cedolin. Stability of structures: elastic, inelastic, fracture, and damage theories. 1991.

[101] P Feraboli, E Peitso, T Cleveland, PB Stickler, and JC Halpin. Notched behavior of prepreg-based discontinuous carbon fiber/epoxy systems. *Composites Part A: Applied Science and Manufacturing*, 40(3):289–299, 2009.

[102] C Qian, LT Harper, TA Turner, and NA Warrior. Notched behaviour of discontinuous carbon fibre composites: Comparison with quasi-isotropic non-crimp fabric. *Composites Part A: Applied Science and Manufacturing*, 42(3):293–302, 2011.

[103] GR Irwin. *Fracture, Vol. VI of Encyclopedia of Physics.* Springer, 1958.

[104] JR Rice. A path independent integral and the approximate analysis of strain concentration by notches and cracks. 1968.

[105] N Tsangarakis. All modes fracture toughness of two aluminium alloys. *Engineering Fracture Mechanics*, 26(3):313–321, 1987.

[106] IY Chang and JF Pratte. Ldf™ thermoplastic composites technology. *Journal of Thermoplastic Composite Materials*, 4(3):227–252, 1991.

[107] G Nilakantan and S Nutt. Reuse and upcycling of thermoset prepreg scrap: Case study with out-of-autoclave carbon fiber/epoxy prepreg. *Journal of composite materials*, 52(3):341–360, 2018.

[108] S Kamat, X Su, R Ballarini, and AH Heuer. Structural basis for the fracture toughness of the shell of the conch strombus gigas. *Nature*, 405(6790):1036–1040, 2000.

[109] F Barthelat, H Tang, PD Zavattieri, CM Li, and HD Espinosa. On the mechanics of mother-of-pearl: a key feature in the material hierarchical structure. *Journal of the Mechanics and Physics of Solids*, 55(2):306–337, 2007.

[110] F Barthelat. Designing nacre-like materials for simultaneous stiffness, strength and toughness: Optimum materials, composition, microstructure and size. *Journal of the Mechanics and Physics of Solids*, 73:22–37, 2014.

[111] H Gao, B Ji, IL Jäger, E Arzt, and P Fratzl. Materials become insensitive to flaws at nanoscale: lessons from nature. *Proceedings of the national Academy of Sciences*, 100(10):5597–5600, 2003.

[112] L Meng, I Oshsawa, and J Takahashi. A parametric study of ultra-thin chopped carbon fiber tape reinforced thermoplastic in double-shear tests. In *18th European conference on composite materials. Athens, Greece*, 2018.

[113] M Salviato, SE Ashari, and G Cusatis. Spectral stiffness microplane model for damage and fracture of textile composites. *Composite Structures*, 137:170–184, 2016.

[114] K Kirane, M Salviato, and ZP Bažant. Microplane-triad model for elastic and fracturing behavior of woven composites. *Journal of Applied Mechanics*, 83(4), 2016.

[115] J Fudge. compelling performance and cost effective material. In *SAMPE conference. Wichita KS*, 2009.

[116] GP Picher-Martel, A Levy, and P Hubert. Compression moulding of carbon/peek randomly-oriented strands composites: a 2d finite element model to predict the squeeze flow behaviour. *Composites Part A: Applied Science and Manufacturing*, 81:69–77, 2016.

[117] B Boursier and Lopez A. Failure initiation and effect of defects in structural discontinuous fiber composites. *Hexcel Research and Technology*, 2010.

[118] M Selezneva. *Experimental and theoretical investigations of mechanical properties of randomly-oriented strand (ROS) composites.* PhD thesis, McGill University, 2015.

[119] MC Preetam and SV Lloyd. Effect of bond quality on crack growth resistance of adhesively bonded composite joints under static and cyclic loading. In *SAMPE Conference, Seattle, WA.*, 22-25 May 2017.

[120] G Nilakantan and S Nutt. Reuse and upcycling of thermoset prepreg scrap: Case study with out-of-autoclave carbon fiber/epoxy prepreg. *Journal of composite materials*, 52(3):341–360, 2018.

[121] Digimat User's Manual. e-Xstream Engineering. Luxembourg. Germany. 2017.

[122] AJ Favaloro, BR Denos, DE Sommer, RA Cutting, and JE Goodsell. Validation of process simulation workflow for thermosetting prepreg platelet molding compounds. *Composites Part B: Engineering*, 224:109198, 2021.

[123] SG Advani and CL Tucker. The use of tensors to describe and predict fiber orientation in short fiber composites. *Journal of Rheology*, 31(8):751–784, 1987.

[124] APC (PEKK) Thermoplastic composite tapes. Online; 2021. https://www.solvay.com/en/product/apc-pekk-thermoplastic-composite-tapes.

[125] A Beghini, G Cusatis, and ZP Bažant. Spectral stiffness microplane model for quasibrittle composite laminates—part ii: Calibration and validation. *Journal of applied mechanics*, 75(2), 2008.

[126] G Cusatis, A Beghini, and ZP Bažant. Spectral stiffness microplane model for quasibrittle composite laminates—part i: theory. *Journal of Applied Mechanics*, 75(2), 2008.

[127] S Ko, J Yang, ME Tuttle, and M Salviato. Stochastic computational modeling of the fracturing behavior in discontinuous fiber composite structures. In *SAMPE Conference. Virtual*, 2020.

[128] SE Phenisee, S Tien, and M Salviato. Spectral stiffness microplane model for unidirectional composites. In *ASC 33rd Annual technical conference, Seattle, WA*, 24-26 Sept 2018.

[129] Y Wan, X Zhang, Y Sato, and J Takahashi. Stochasticity modeling and analysis of elastic modulus of randomly oriented strands. *Advanced Composite Materials*, 30(3):286–306, 2021.

[130] J Xue and K Kirane. Strength size effect and post-peak softening in textile composites analyzed by cohesive zone and crack band models. *Engineering Fracture Mechanics*, 212:106–122, 2019.

[131] SS Zumdahl and DJ DeCoste. *Chemical Principles.* Brooks Cole, 2016.

Appendix A

We tested unnotched tension of the quasi-isotropic (QI) laminate samples made of Toray T700G-12K prepreg system. The prepreg system was the identical material used in Ch. 5 and 6. The QI stacking sequence was $[0/45/90/-45]_{2s}$. The coupon geometry was 140×25.5 mm. The coupon thickness was 2.47 mm. We used a closed-loop, servo-hydraulic Instron 5585H with 200 kN capacity. The nominal strain rate was set to 0.2 %/min. The DIC technique was used to calculate the displacement field. We used a Nikon D5600 DSLR camera with Nikon AF micro 200 mm. A sampling rate of 1 Hz was taken.

The stress and strain curves of 6 QI coupons are plotted in Fig. A.1 and recorded in Table A.1. Unlike the DFCs shown in Fig. 3.2, the experimental curves of the continuous fiber composites are much pronounced linear up to the strength and followed by the sudden drop. Unlike the DFCs, the fracture of the continuous fiber composites is mainly dominated by the single damage mechanism. Therefore, the modulus tends to remain relatively constant until the final failure.

Coupon ID	Modulus [GPa]	Strength [MPa]
1	47.1	584.3
2	44.2	555.7
3	47.7	561.5
4	46.0	574.8
5	46.0	599.2
6	44.9	561.7

Table A.1: Unnotched tension experimental results of the quasi-isotropic laminate.

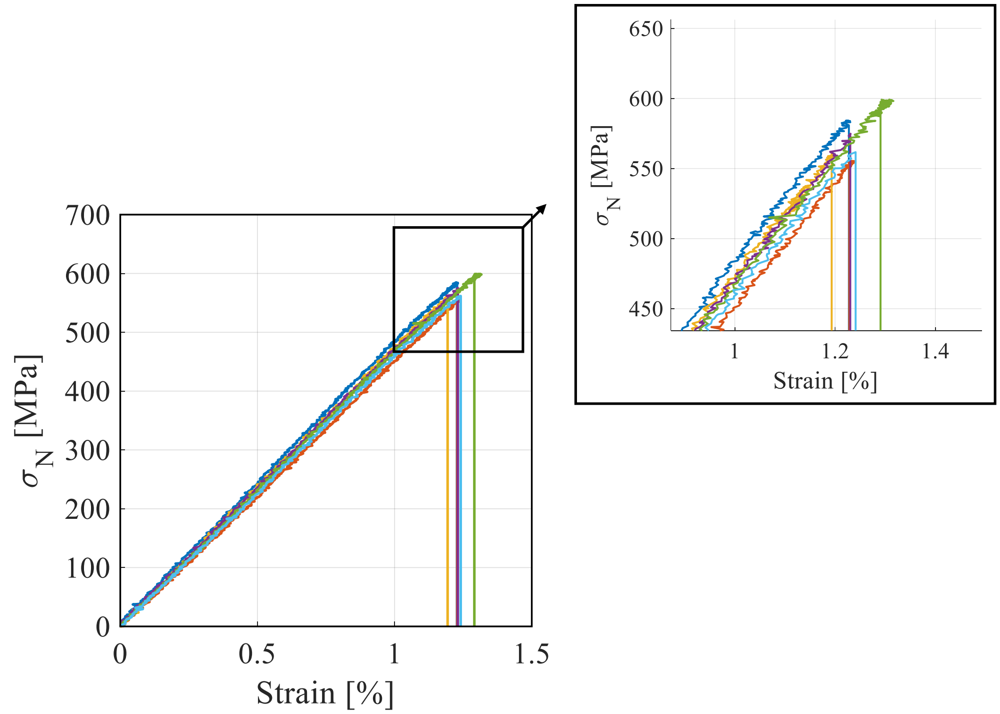

Figure A.1: The experimental stress and strain curves of 6 unnotched tension quasi-isotropic laminate coupons.

VITA

Seunghyun Ko was born in Seoul, South Korea. He earned his B.S. in Aeronautics & Astronautics degree from the University of Washington in 2015. Then, he joined the Laboratory for Engineered Materials and Systems (LEMS), led by Professor Jinkyu Yang (co-chair) at the same university right after finishing his Bachelor's degree. He joined the Laboratory for Multi-scale Analysis of Materials & Structures (MAMS) led by Professor Marco Salviato (chair) in the winter of 2016. In autumn 2021, he earned his Ph.D. degree in Aeronautics & Astronautics from the University of Washington.